12-31-2020

Small-scale dynamics of photospheric magnetic activities and their chromospheric responses

Jiasheng Wang
New Jersey Institute of Technology

ABSTRACT

SMALL-SCALE DYNAMICS OF PHOTOSPHERIC MAGNETIC ACTIVITIES AND THEIR CHROMOSPHERIC RESPONSES

by
Jiasheng Wang

The evolution of photospheric magnetic fields is considered as the fundamental source of forming atmospheric structures and triggering most solar activities, including flares and mass ejections on various scales (CMEs, jets, etc.). With implementation of high-resolution observational instruments, small-scale details of magnetic features are recognized that can provide important information regarding the evolution in active regions and the connection between photospheric magnetic reconnection and jet-like ejections in the quiet Sun. This research takes advantage of the exceptionally high-resolution measurements of vector magnetic field and imaging observations by the Goode Solar Telescope, and UV/EUV imaging observations from space-based instruments. The studied topics include structural evolution of penumbra and shear flows in response to a flare eruption, flux emergence in the formation of an active region, and small-scale magnetic reconnections in the photosphere in a coronal boundary. The main findings in this dissertation work are listed as follows:

- Using high-resolution imaging observation in the TiO band by GST and photospheric vector magnetic field observation by the Helioseismic and Magnetic Imager, strong shear flow expansion in a precursor kernel near the polarity inversion line (PIL) is found to be closely associated with the M6.5 flare in AR 12371, which indicates a linkage between small-scale magnetic changes and the flare eruption. Flow field of the penumbra in the flaring core region is calculated using the differential affine velocity estimator. An enhancement of penumbral flows (up to an unusually high value of 2 km s^{-1}) and an extension of penumbral fibrils after the first peak of the flare hard X-ray (HXR) emission are observed to be accompanied by a rapid increase of horizontal field. These results provide evidence of the back reaction theory of coronal restructuring on the photosphere as a result of flare energy release.
- Taking advantage of high-resolution magnetic field measurements, TiO continuum, and Hα observations by GST, small-scale magnetic flux emergences in the AR

12665 are observed in two types of topology: magnetic flux sheet emergence associated with the newly forming granules, and the traditional magnetic flux loop emergence. Both types of flux emergence are associated with darkening of granular boundaries, while only flux sheets elongate granules along the direction of emerging magnetic fields and expand laterally. Hα observations reveal transient brightenings in the events of magnetic loop emergence, which are most probably the signatures of Ellerman bombs.

- Statistical study of small-scale magnetic reconnections around the coronal hole boundary is achieved by tracking magnetic features with the Southwest Automatic Magnetic Identification Suite (SWAMIS). The tracking results show that the magnetic energy release rate by small-scale cancellation inside the coronal hole is 3 times higher than that outside the coronal hole. Spicules are likely associated with these kinds of reconnections, while only a small portion of the release magnetic energy is directly deposited to hot plasma.

SMALL-SCALE DYNAMICS OF PHOTOSPHERIC MAGNETIC ACTIVITIES AND THEIR CHROMOSPHERIC RESPONSES

by
Jiasheng Wang

A Dissertation
Submitted to the Faculty of
New Jersey Institute of Technology and
Rutgers, The State University of New Jersey – Newark
in Partial Fulfillment of the Requirements for the Degree of
Doctor of Philosophy in Applied Physics

Department of Physics

December 2020

APPROVAL PAGE

SMALL-SCALE DYNAMICS OF PHOTOSPHERIC MAGNETIC ACTIVITIES AND THEIR CHROMOSPHERIC RESPONSES

Jiasheng Wang

Dr. Haimin Wang, Dissertation Co–Advisor Date
Distinguished Professor of Physics, Director of Space Weather Research Laboratory, NJIT

Dr. Chang Liu, Dissertation Co–Advisor Date
Distinguished Research Professor of Physics, NJIT

Dr. Dale E. Gary, Committee Member Date
Distinguished Professor of Physics, Director of Owens Valley Solar Array, NJIT

Dr. Wenda Cao, Committee Member Date
Professor of Physics, Director of Big Bear Solar Observatory, NJIT

Dr. Chengjun Liu, Committee Member Date
Professor of Computer Science, Director of Face Recognition and Video Processing Lab, NJIT

BIOGRAPHICAL SKETCH

Author: Jiasheng Wang

Degree: Doctor of Philosophy

Date: December 2020

Undergraduate and Graduate Education:

- Doctor of Philosophy in Applied Physics,
  New Jersey Institute of Technology and Rutgers-Newark, Newark, NJ, 2020
- Bachelor of Science in Earth and Space Sciences,
  University of Science and Technology of China, Hefei, China, 2015

Major: Applied Physics

Presentations and Publications:

J. Wang, C. Liu, and H. Wang, "A High-resolution Study of Magnetic Field Evolution and Hα Spicules Around a Coronal Hole," in preparation.

J. Wang, C. Liu, W. Cao, and H. Wang, "High-resolution Observations of Small-scale Flux Emergence by Goode Solar Telescope (GST)," *The Astrophysical Journal*, Volume 900, Issue 1, article id.84, 12 pp, September 2020.

J. Wang, C. Liu, N. Deng, and H. Wang, "Evolution of Photospheric Flow and Magnetic Fields Associated with the 2015 June 22 M6.5 Flare," *The Astrophysical Journal*, Volume 853, Issue 2, article id. 143, 9 pp, February 2018.

C. Liu, W. Cao, J. Chae, K. Ahn, D. Prasad Choundhary, J. Lee, R. Liu, N. Deng, J. Wang, and H. Wang, "Evolution of Photospheric Vector Magnetic Field Associated with Moving Flare Ribbons as Seen by Goode Solar Telescope (GST)," *The Astrophysical Journal*, Volume 869, Issue 1, article id. 21, 13 pp, December 2018.

C. Liu, Y. Xu, W. Cao, N. Deng, J. Lee, H.S. Hudson, D.E. Gary, J. Wang, J. Jing, and H. Wang, "Flare Differentially Rotates Sunspot on Sun's Surface," *Nature Communications*, Volume 7, article id. 13104, 9 pp, October 2016

J. Wang, C. Liu, and H. Wang, "A High-resolution Study of Magnetic Field Evolution at Coronal Hole Boundary," *iPoster*, Virtual 50th Anniversary Meeting of the AAS Solar Physics Division, August 2020.

J. Wang, C. Liu, and H. Wang, "High-resolution Observations of Small-scale Flux Emergence in Multiwavelengths by Goode Solar Telescope (GST)," *Oral presentation*, AAS/Solar Physics Division 50th Meeting, St Louis, Missouri, June 2019.

J. Wang, C. Liu, and H. Wang, "Fine-scale Emerging Flux in NOAA AR 12665 Observed by BBSO/GST," *Oral presentation*, First Ten Years of Goode Solar Telescope (GST) Workshop, Newark, New Jersey, March 2019.

J. Wang, C. Liu, and H. Wang, "Elementary Emerging Flux Near PIL Observed by GST/NIRIS on 2017 July 13," *Oral presentation*, The Triennial Earth-Sun Summit (TESS)/Solar Physics Division 49th Meeting, Leesburg, Verginia, May 2018.

J. Wang, C. Liu, N. Deng, and H. Wang, "Evolution of Photospheric Flow and Magnetic Fields Associated with 2015 June 22 M6.5 Flare," *Poster*, American Physical Society, Newark, New Jersey, November 2017.

J. Wang, C. Liu, N. Deng, and H. Wang, "Evolution of Photospheric Flow and Magnetic Fields Associated with 2015 June 22 M6.5 Flare," *Oral presentation*, AAS/Solar Physics Division 48th Meeting, Portland, Oregon, August 2017.

To

my mother & father,
for their unconditional love and support in my life.

ACKNOWLEDGMENT

It is a great pleasure that I have this opportunity upon finishing my dissertation to give thanks to so many people who have helped me during my graduate study.

I would like to express my deep and sincere gratitude to my research advisor Dr. Haimin Wang, for giving me the opportunity and financial support to do research in solar physics. It is Dr. Wang who inspired me in exploring interests of study and kept me encouraged through any challenges and difficulties with his rich knowledge and great wisdom. Without his insightful advice on my research, I could not have finished my dissertation. It is a great honor for me to have such a wonderful mentor who led me into the area of solar physics and showed tremendous enthusiasm in research.

I am deeply grateful to my co-advisor Dr. Chang Liu for his patient guidance and enlightening advice on my research. Dr. Liu sets an example for me on how to be an academically devoted scientist and conduct research with rigorous attitude. I truly appreciate every opportunity I had to discuss with him about my research and learned a lot from his rich knowledge in solar sciences and inspirational ideas that guide me in my research.

My heartfelt thanks to Dr. Dale E. Gary, Dr. Wenda Cao, and Dr. Chengjun Liu for serving as members of my Ph.D dissertation defense committee. I thank Dr. Gary for sharing expertise in solar and radio astronomy in lectures and group meetings. Thanks to Dr. Cao for helping me get permissions to use the most advanced GST data from collaborators and sharing professional advice in observation.

This work is supported by NSF under grants AGS-1348513, AGS-1408703, AGS-1821294, AGS-1954737, and AGS-1927578, by NASA under grants NNX13AF76G, NNX13AG13G, NNX16AF72G, 80NSSCITK0016, 80NSSC19K0257 and

80NSSC20K0025, and by National Science Foundation of China (NSFC) under grant 11729301.

I would like to thank the CSTR people for having a such academic friendly environment. I thank Drs. Yan Xu, Ju Jing, and Gelu Nita for valuable discussions and ideas of research. My special thanks to Dr. Jeongwoo Lee for his constructive comments on my recent research and help me with my presentation practice. I am thankful to Dr. Bin Chen and Sijie Yu for organizing weekly journal club where current advances in solar and terrestrial researches are routinely exchanged. I thank Dr. Gregory D. Fleishman for hosting the online SolFER Colloquium. I thank Drs. Shuo Wang, Xin Chen, and Xu Yang for their helps in my learning of research techniques and my graduate student life. I cherish my friendship and communications with Dr. Qin Li, Nengyi Huang, Mr. Yingjie Luo, Mr. Nian Liu and Mr. Yi Chai.

I would like to thank all faculty and staffs from Big Bear Solar Observatory (BBSO) for their hard work so that the state of the art data can be obtained for my study. I thank Dr. Vasyl Yurchyshyn for sharing insights of jets study and observation advice. I am grateful to Claude Plymate, Nicolas Gorceix, John Varsik, Sergey Shumko, and Jeff Nenow for their technical support during my observation stay in BBSO. I also thank Dr. Kwangsu Ahn for providing inverted magnetic field data with his expertise.

Last but not the least, I would like to thank my parents, Yikang Wang and Jinli Duan, for their endless love and support in my life.

TABLE OF CONTENTS

TABLE OF CONTENTS
(Continued)

Chapter **Page**

TABLE OF CONTENTS
(Continued)

Chapter **Page**

LIST OF TABLES

Table **Page**

LIST OF FIGURES

Figure **Page**

LIST OF FIGURES
(Continued)

Figure **Page**

LIST OF FIGURES
(Continued)

Figure **Page**

LIST OF FIGURES
(Continued)

Figure **Page**

LIST OF FIGURES
(Continued)

Figure **Page**

LIST OF FIGURES
(Continued)

Figure **Page**

LIST OF FIGURES
(Continued)

Figure **Page**

LIST OF FIGURES
(Continued)

Figure **Page**

LIST OF FIGURES
(Continued)

Figure **Page**

CHAPTER 1

INTRODUCTION

Solar activities exert perpetual influences to the solar system on various time scales, from milliseconds to thousands of years. Of the most important and specific interest to solar scientists are the eruptive solar activities, i.e., solar flares. Although even the strongest flares can hardly perturb the total solar irradiance (1367 W m^{-2}), such dynamic explosions are capable of releasing substantial amount of energy up to 10^{32}ergs in 100–1000 s and are often accompanied with coronal mass ejections (CMEs) and solar energetic particles (SEPs). The accelerated ionized particles fill the interplanetary space through solar wind and put threats to our modern society and technology, including electronic communications, air transportation, and near earth satellite safeties. Thus study of the solar flare mechanisms and evolution of solar eruptions is critical in terms of advancing the predictability of space weather. In the solar atmosphere (photosphere, chromosphere, and corona), manifestations of flares are associated with magnetic energy storage and release. Magnetic fields play an important role in varying the solar atmospheric structures. Taking advantage of the state-of-the-art ground based telescopes (e.g., Goode Solar Telescope, GREGOR Solar Telescope) and space-based instruments (e.g., Helioseismic and Magnetic Imager (HMI) on board the Solar Dynamic Observatory (SDO), Solar Optical Telescope (SOT) on board Hinode), our understandings of the magnetic structures and evolution are considerably advanced. However, the details of magnetic evolution are still not fully understood, especially the small-scale magnetic energy budget in the photosphere.

1.1 Formation of the Active Regions

An active region (AR) on the Sun is where the strong magnetic flux is lifted from solar interior to the solar atmosphere. Typically, the areas of concentrated radial photospheric magnetic fields of ∼kG in ARs are called sunspots. Parker [154], Wilson [250], and Ponomarenko [159] proposed that the formation of sunspots in ARs start with magnetic flux rope emerging into photosphere through magnetic buoyancy and convergence of supergranule flux through convection. During formation of an AR, strong radial magnetic fields in a sunspot spread out and intrude below the photosphere, thus turn into horizontally inclined fields at edges of the sunspot, which are observed as penumbra in white light continuum. Based on the difference of magnetic topology in ARs, sunspot groups are commonly categorized by Mount Wilson classification [105]: α – a sunspot group of same polarity; β – a bipolar sunspot group with a simple division between sunspots of opposite polarities; γ –a sunspot group of complex polarities so that the polarity inversion line (PIL) cannot be identified; and the configuration of δ group – umbrae of opposite polarities locate in the same penumbra. Flare productive ARs often consist of various magnetic classifications in sunspot groups, of which the studies (e.g., [267, 133, 206, 210]) show that the existence of δ–sunspots is highly correlated to flare eruptions. Figure 1.1 shows high-resolution images of a flare producing AR on the Sun. Near the disk center, a group of $\beta\gamma\delta$–sunspots with flare ribbons are clearly seen in the ultraviolet (UV) 1600 Å image (the top left panel taken by the Atmospheric Imaging Assembly (AIA; [111]) on board the Solar Dynamics Observatory (SDO)). According to the National Oceanic and Atmospheric Administration (NOAA), this region is numbered as 12371, which produced diverse solar eruptions on different scales in its life cycle, including four M-class flares and one C-class flare.

As the fundamental source of most of the phenomenal solar activities, magnetic field of ARs is of great interest to solar physicists. With the availability of

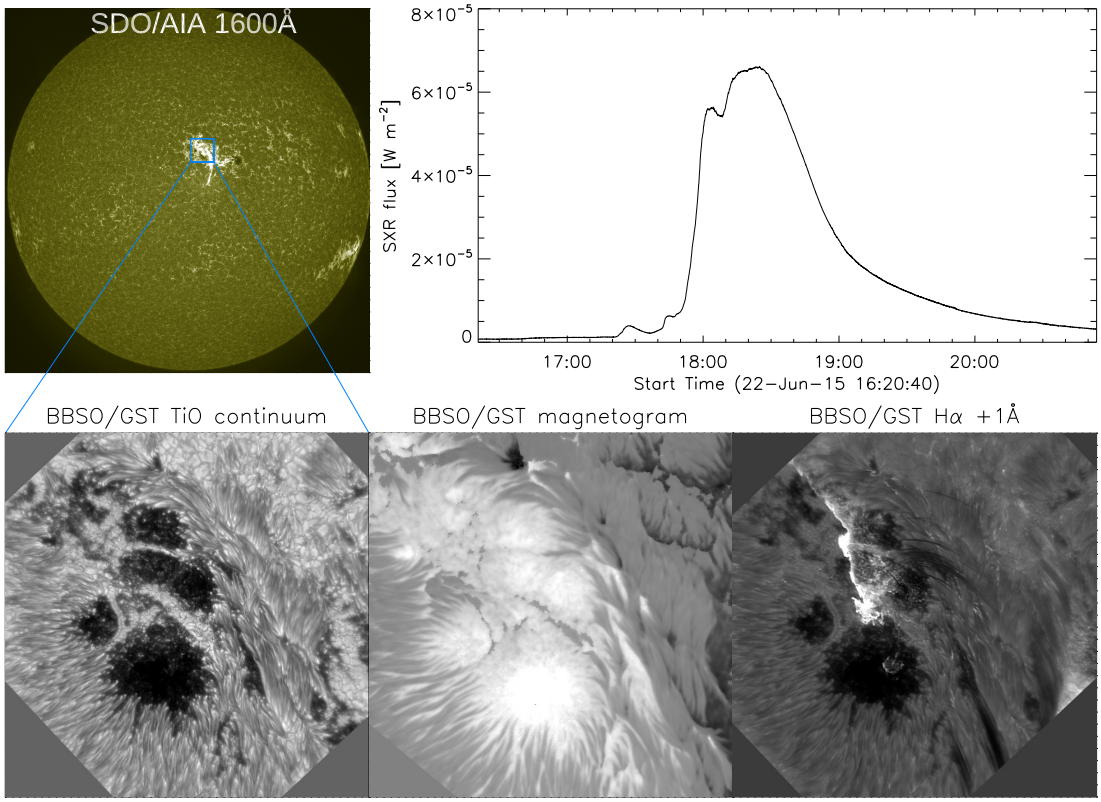

Figure 1.1 Flare-productive NOAA AR 12371. Images of the observation are obtained from SDO and the ground-based instrument in BBSO/GST. Light curve of GOES soft X-ray 1–8 Å indicates solar radiation changes due to flares associated with magnetic eruptions.
Image sources: BBSO/GST, AIA/SDO, GOES

magnetograms, understandings of structure and nonpotentiality of the photospheric magnetic field are greatly advanced. The generation of ARs is investigated from two perspectives: flux emergence modelling from solar interior and multiwavelength observations of reconnections of emerging flux in the solar atmosphere.

1.1.1 Flux Emergence Theory

A vastly accepted flux emergence model forming ARs is the toroidal magnetic flux rope rising from the deep convection zone through magnetic buoyancy [154]. Basic physics of flux emergence from solar interior is derived based on ideal gas assumptions.

Assuming a magnetic flux tube of field strength B is embedded in convection zone, when the magnetic structure reaches pressure equilibrium,

$$p_e = p_i + \frac{B^2}{8\pi}, \tag{1.1}$$

where p_e and p_i are thermal pressures of the ambient environment and in the magnetic flux tube, respectively. The magnetic pressure is $p_m = \frac{B^2}{8\pi}$. In this case, gas thermal pressure satisfies the relation $p_e > p_i$. If the magnetic structure is also in thermal equilibrium with ambient background ($T_i = T_e = T$), then Equation (1.1) can be rewritten as,

$$\rho_e = \rho_i + \frac{B^2}{8\pi}\frac{m}{k_B T}, \tag{1.2}$$

where ρ_e (ρ_i) is density in background (magnetic structure), m is molecule mass, and k_B is Boltzmann constant. The unbalance of gas pressure is then caused by the density deficiency in the magnetic structure, i.e., $\Delta\rho = \rho_i - \rho_e < 0$, which drives the magnetic structure to surface from surroundings. The magnetic buoyancy force is

$$f_{MB} = \Delta\rho g = -\beta^{-1}\rho g, \tag{1.3}$$

where plasma–β is defined as the ratio of thermal pressure and magnetic pressure ($8\pi p/B^2$). Hence, buoyancy dominates the evolution of the highly magnetized plasma with field strength above 10^3 G in absence of significant convection [154].

Generally, the numerical simulations of the buoyant magnetic structures emerging from the convection zone exclude influences other than magnetic buoyancy, such as pressure gradient and Lorentz force, from consideration of initial equilibrium setup (for details see Chapter 3 in [33]). The magnetic evolution of flux emergence is developed by inserting a horizontal flux tube wrapped in twisted field. In this case the perturbed magnetic structure rises into arched flux tube as a result of three-dimensional buoyant instability while still remains coherent in its emerging

process [55]. Because of the significant vertical gradient of gas pressure through convection zone [189, 37, 220], the magnetic tube must expand laterally to maintain gas pressure equilibrium with its surroundings [141, 34, 148]. Due to vortex motion associated with flux emergence, relatively weak poloidal field is sufficient for magnetic flux tube to rise to the solar surface while generate twist of the emerging flux tube [85, 9]. The typical model of formation of ARs through flux emergence shows that the twisted rising magnetic flux tube deforms to an Ω-loop and enters photosphere so that an AR with opposite polarities is developed [56].

In the radiative MHD simulations, Cheung et al. [34] found that the semitorus-shaped flux tube emerges into the photosphere with an upward speed of 0.5–1 km s^{-1} in ∼4–5 hours before small pores appear in multiple locations. Sunspots are formed at the locations where semitorus footpoints are rooted in two hours. In the presence of convective flows generated by photospheric cooling in the upper convection zone, magnetic flux emerges as small-scale undular transient in the first stage (see Figure 1.2(b)), followed by a gradual flux concentration process. Such serpentine nature of granular-sized magnetic field is explained as an interplay of convective downflow and buoyantly rising magnetic field [195, 152, 36]. Simulations of the photospheric properties of emerging flux regions (EFRs) show the enhancement of evanescent horizontal field in the neighboring granular cells with upflowing plasma in darkening continuum counterparts [36, 144].

The upward motions and horizontal expansion of magnetic field and plasma are responsible for the chromospheric eruptions at different heights. The undular topology of the emerging magnetic field can lead to the formation of bald patches, in which the U-loops under the solar surface can generate Ellerman bombs (EBs) [94, 8] and the Ω-loops that are more profoundly associated with jet eruptions [143, 142, 201, 253]. Such eruptions are produced by magnetic reconnection due to the emergence of

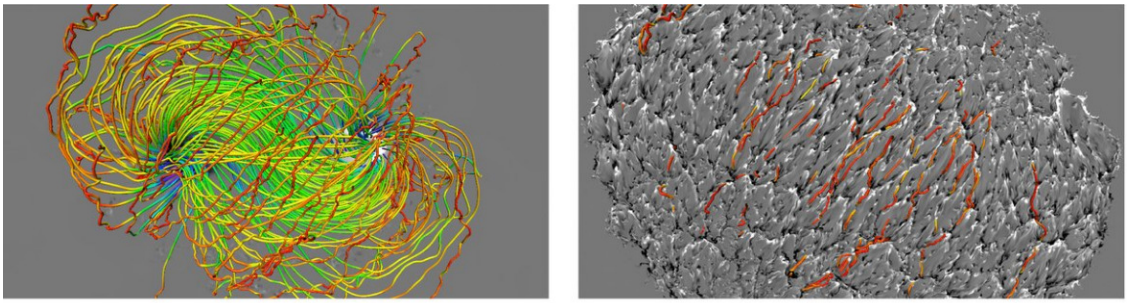

(a) (b)

Figure 1.2 Magnetic structure of a semi-torus as it erupts onto the solar surface. The panel (a) shows the distribution of the vertical component of the magnetic field (scaled between ±17 kG) at z = −7.5 Mm. The panel (b) shows the corresponding magnetic map at z = 0 (scaled between ±2 kG), which highlights the serpentine nature of the magnetic field lines near the surface as a consequence of the interaction between the emerging field and the granular convective flows.
Adapted from [34]

magnetic field. At the same time, a large fraction of mass confined in the rising field is discharged from magnetic structure and drain below the surface.

1.1.2 Flux Emergence Observations

In the process of flux emergence, magnetic flux contents is observed in a wide range of sizes, from as large as sunspots of 30 Mm in diameter carrying 10^{22} Mx to pores, ephemeral regions, and faculae with flux in 10^{18}–10^{20} Mx [76, 203]. Flux emergence regions evolve actively to form active regions and generate consequent long-term photopsheric evolution and abrupt solar activities. Since the discovery of magnetic field in sunspots [77], evolution of the solar active regions are quantified extensively by their magnetic characteristics. The lifetime of active regions shows close relations with the embedded magnetic flux, i.e., as shown in Table 1.1 (summarized in Chapter 2 of van Driel-Gesztelyi and Green [215]). The typical lifetime has a positive correlation with maximum magnetic flux of an AR. Zwaan [270] summarized that the bipolar emerging signature does alter its surrounding magnetic structure and as the emerging flux region grows, it ranges from a small bipole with magnetic flux $\Phi \leq \times 10^{20}$ Mx that

does not develop beyond an ephemeral active region, to a large AR with $\Phi \geq \times 10^{21}$ Mx that structures sunspots. A dark pore can attain magnetic field of 1900–2600 G at end of the emergence phase while sunspots umbrae typically contain field over ∼3000 G [269, 20]. Study of the horizontal dynamics in large EFRs shows that small magnetic elements of opposite polarities scatter in the whole region in an organized manner, in which a string of pores extend from the major preceding sunspot to the major following sunspot, making a thread-like distribution of magnetic flux in magnetograms [194].

Table 1.1 Relations of Typical Magnetic Flux, Lifetime, and Ratio of Emergence Phase to AR Lifetime

Regions	Magnetic flux[a] (Mx)	Lifetime
Large (with sunspots)	$5–30\times10^{21}$	weeks–months
Small (pores, no spots)	$0.1–5\times10^{21}$	days–weeks
Ephemeral	$0.3–10\times10^{19}$	hours–≈ 1 day

[a]Unsigned magnetic flux in one polarity of the active region.

Besides the appearance of magnetic concentrations in the photosphere, vector magnetic field product reveals that in the emergence of small bipolar active regions, horizontally inclined field of 200–600 G rises through solar surface at an apparent speed of ∼1 km s^{-1}[116]. The magnetic field of individual emerging elements can reach kG when the emerged flux diverges from emergence site rapidly and attains more vertical field in the process. From a statistical study of 37 emerging ARs, strong magnetic field distribution is seen to be significantly reduced comparing to prior peak of flux emergence. Dacie et al. [40] proposed the evolution of field distribution as a result of magnetic flux reprocessing by magneto-convection. Moving

magnetic features resulted from convective flows remove magnetic field from the decaying AR. At the same time, emerged fluxes of opposite polarities are concentrated along boundaries of supergranules. They coalesce with each other and descend into subsurface. The cancelled flux is redistributed by near surface convection and emerges in the intranetwork.

Due to the serpentine nature of small-scale emerging field in the EFR, recurring emergence and cancellation of magnetic elements are observed in the photosphere with high spatial resolution data [194, 195]. Such frequent magnetic reconnections are driven by horizontal motion of granules and faculae embedded in the intergranular lanes. Figure 1.3 shows properties of dynamic small-scale structure in the emerging NOAA AR 5617. Near the PIL, small-scale emergences repeatedly occur on 10 minutes timescale and display braided pattern in magnetograms (see Figure 1.3(a)) and aligned arch filament system in Hα (see Figure 1.3(b)). During the lifetime of individual small-scale emergence, footpoints of the flux tube separate in an average speed of 1.4 km s^{-1}, moving toward the edge of the active region with the same polarity of their own.

With high-resolution photospheric vector magnetograms and Hα blue wing images, Pariat et al. [152] found EBs [54] in the dipped field lines of undulatory flux tubes during flux emergence. They proposed that EBs could be due to magnetic reconnection where field lines present a U-loop shape, which is defined as bald patch. This type of reconnection discharges magnetic flux from the dipped field with dense material trapped in photosphere (also see [240, 219, 218]). UV/EUV emissions in chromosphere and transition region are also witnessed to be associated with magnetic energy release in the form of flux cancellation during the emergence process. Particularly, intense transient brightenings in 1400 Å, 1600 Å, and 1700 Å are identified as UV bursts [209, 205], which are caused by small-scale reconnections in the lower atmosphere. Jets, on the other hand, are usually observed in EUV

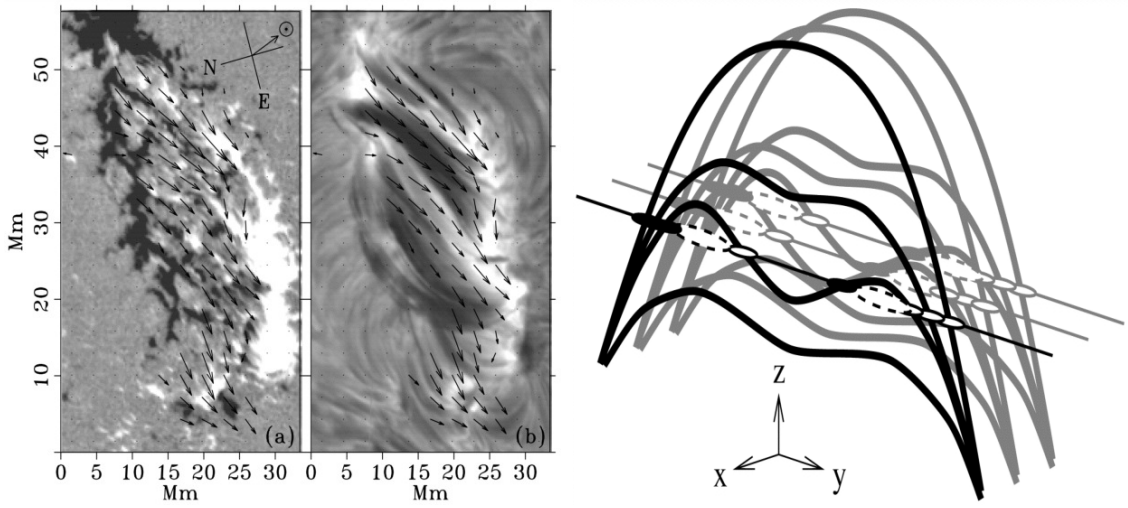

Figure 1.3 Left: (a) a magnetogram and (b) the Hα nominal line-center intensity of the NOAA AR 5617. Overlaid vector field shows the average velocity of facular elements. Right: a model of undulatory flux tubes in vertical sheets, of which each produces a sequence of aligned flux emergence events.
Adapted from [195]

and X-ray wavelengths. They are characterized to have a size of 4,000–10,000 km, transverse velocity of 50–100 km s^{-1}, and lifetime of 2–4 minutes [31]. The onset of jet ejections is divided into two classes: standard jets – the rising arch of untwisted magnetic field reconnects with ambient open field so that heated plasma escapes upward, and blowout jets – the highly sheared and twisted core arch field produces an ejective eruption as it also reconnects with ambient open field [139]. The blowout jets are often associated with small-scale filament eruptions, by which coronal heating process may be powered [191]. With availability of high-resolution observations (SDO/AIA, Hinode/XRT, IRIS), both types of jet ejections are observed on various scales, including coronal jets, macrospicules, and spicules (e.g., [119, 261, 1, 190, 151]).

1.2 Solar Flares

Solar flares are a sudden release of energy in the atmospheric layers of the Sun. The discovery of solar flares is dated back to 1859 September 1, when Carrington [26] and

Hodgson [82] witnessed a brilliant brightening in a large group of sunspots in white light. Although solar flare eruptions are detectable in a broad range of spectrum, white light flares are exceedingly rare, comparing to those in X-ray, UV/EUV, and radio wavelengths. Thanks to the invention of spectroheliograph by G.E Hale, the first photographic figure of solar flare on 1892 July 15 was obtained in Hα line, following which observations of solar flares in the optical wavelength of Hα line by spectrohelioscope became easier and increased over the time. In the optical aspect of flare observations, flare emission is most responsive in the lowest Balmer series (i.e., Hα) in the early phase of flare development. When flares reach maximum phase, the whole spectrum in the range of 3550–6600 Å turns into emission. Flare classification based on flaring area and maximum brightness is denoted ascendantly as *S–1–2–3–4*, in which *S* represents subflares and *4* represents the most extensively large flares that cause interplanetary and terrestrial disturbances [223]. Nowadays, flare strengths are classified by their soft X-ray brightness in the wavelength range of 1–8 Å taken by the Geostationary Operational Environmental Satellite (GOES; [65]). There are five categories in logarithm order of peak flux, A, B, C, M, X, corresponding to 10^{-8}, 10^{-7}, 10^{-6}, 10^{-5}, 10^{-4} W m^{-2} at 1 AU, respectively.

Triggering mechanisms of solar flares with manifestation of emissions in a wide range of wavelengths have been investigated extensively from magnetic perspective since the discovery of magnetic field on the sun [77]. It is now generally believed that solar flares are powered by free magnetic energy stored in the corona [161], and that the energy released via magnetic reconnection causes plasma heating and particle acceleration [177], producing various flaring signatures at multiple heights in the solar atmosphere. Following the observational results, a series of classical models were proposed by Carmichael [25], Sturrock [196], Hirayama [81], and Kopp and Pneuman [104] to describe solar flare eruptions based on two-dimensional (2D) magnetic reconnection theory. These models are collectively called CSHKP model

and have been regarded as a standard model. This classical *two-ribbon-flare* model predicts that in long-duration-event (LDE) flares the rising closed magnetic field is opened by MHD instability in association with filament eruption, followed by reconnection in the vertical current sheet at magnetic null point due to inflow driven by Lorentz force. In addition, observations of hard X-ray emissions and fast MHD shock (termination shock) on top of the reconnected loop indicate hot plasmoid ejection in impulsive compact-loop flare production [64, 178, 213]. A schematic picture of the modified CSHKP model was introduced by Shibata [178] to depict basic features of both LDE and impulsive flares (see Figure 1.4).

The free energy released in the process of flare eruption is usually defined as an excess of magnetic field energy in the active region over the potential field energy in the same boundary conditions. The photospheric magnetic field properties such as total magnetic flux, photospheric free energy, and total vertical current are closely associated with flare productivity. In combination with measures of magnetic shear, these photospheric magnetic quantities can serve as a flare indicator [107, 98]. The importance of magnetic shear for the onset of flares and CMEs is emphasized in the tether-cutting model [140], in which a sigmoid configuration is formed by magnetic bipoles with their footpoints connected by sheared core fields. In this scenario, runaway tether-cutting reconnection occurs in the sheared core field of the crossed arms of the two binding magnetic loops (see Figure 1.5). Observations of the brightened sigmoid and the new enveloping flare arcade after reconnection were achieved in soft X-ray wavelengths.

Although tremendous efforts have been devoted to flare studies, many fundamental physical problems are still not well understood, such as the energy build-up and triggering of flares, and the consequent back reaction into the low atmosphere as a result of the sudden coronal restructuring (see Wang & Liu[229] and Toriumi & Wang[211] for recent reviews). Since coronal magnetic fields are anchored to the dense

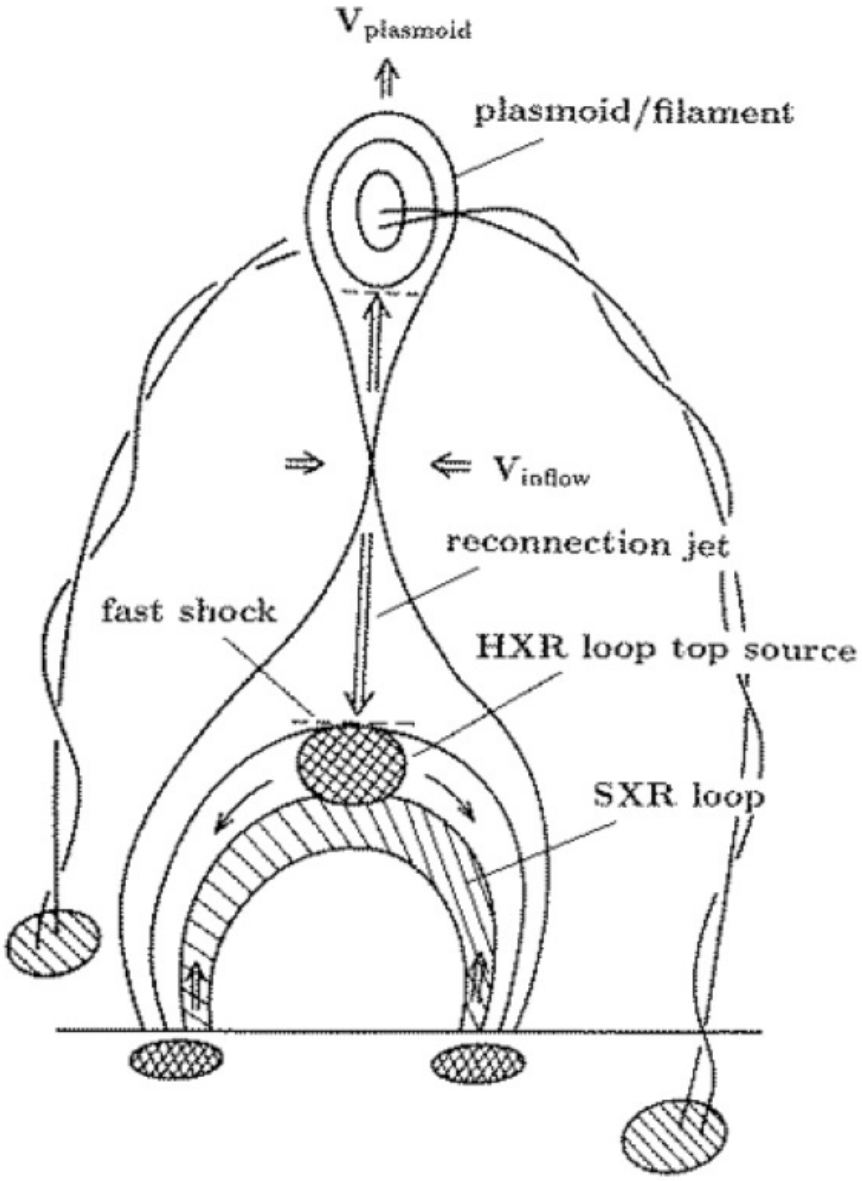

Figure 1.4 A modified CSHKP–plasmoid ejection model for compact-loop flares and standard two-ribbon flares. Evidence of HXR is observed on top of the heated loop by Yohkoh.
Adapted from [178]

photosphere, insights into these problems can be obtained by studying the structural evolution of photospheric magnetic field and the closely coupled plasma flow field leading to and from flare events. In general, the first problem above is often related to relatively long-term (in hours to days) evolution of magnetic and flow fields (e.g.,

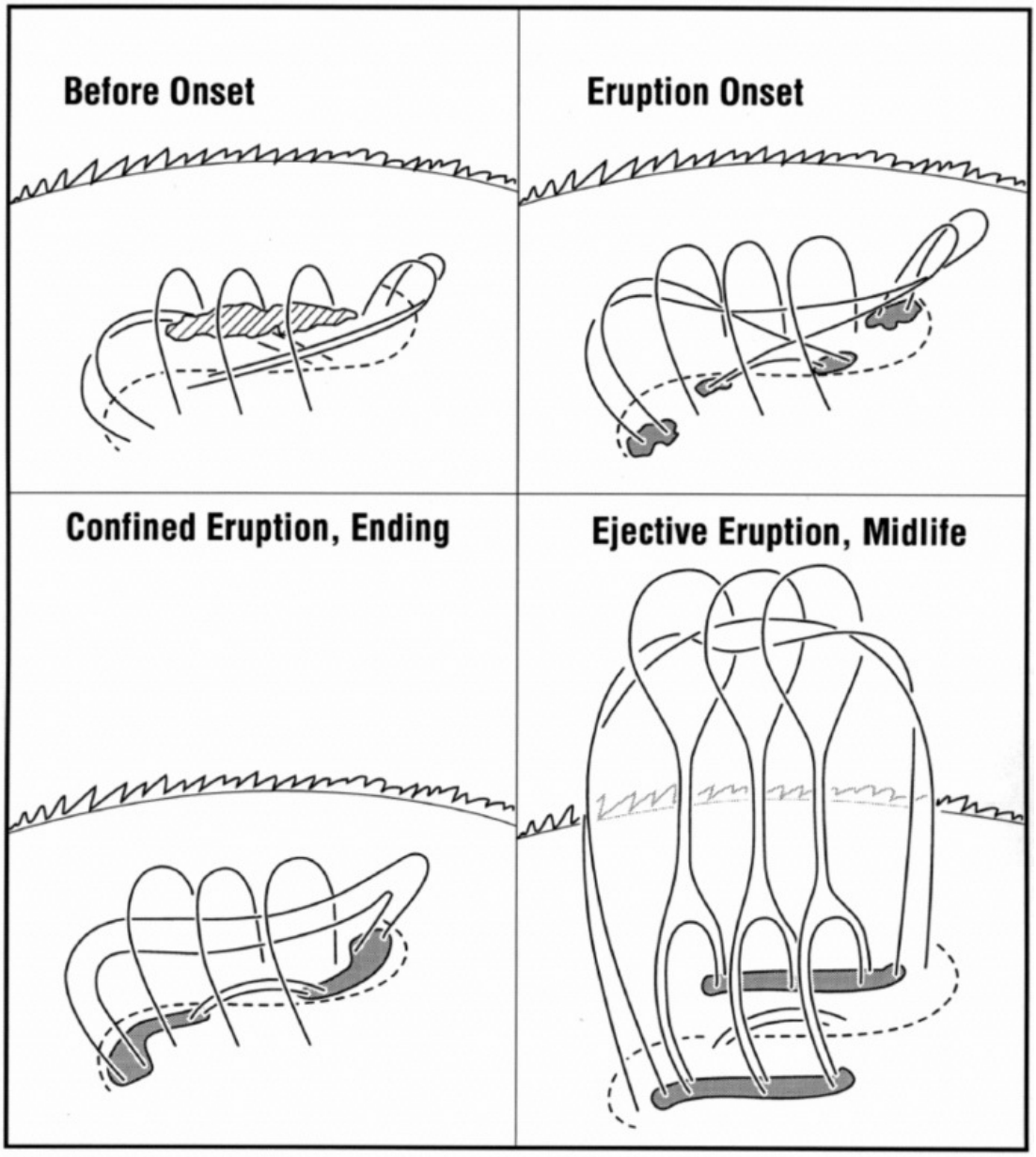

Figure 1.5 A schematic figure of tether-cutting model, in which ejective eruption (lower right panel) and confined eruption (lower left panel) both begin in the same way: the two opposite elbow ends of the sigmoid, with crossed arms over the neutral line, brighten and expand as a new bright sheared arcade appears and grows below the crossed arms. A new bright strand connecting the far ends of the elbows appears above the crossed arms and rises upward. The envelop field blows open in association with a CME in ejective eruptions and transforms to closed long-duration flare arcade, whereas the explosions are enclosed in the sigmoidal bipole with a shorter period of flare in confined eruptions.
Adapted from [140]

emerging fluxes, shear and converging flows), while the second problem above deals with short-term (in tens of minutes) flare-induced changes of magnetic/flow fields down to the photosphere of solar eruption.

1.2.1 Photospheric Magnetic Field Evolution

It is particularly noticeable that back reaction due to flares is traditionally considered to be small because of the large inertia of the photosphere. The reconfiguration of coronal field is the focus of almost all models of flares and the often associated coronal mass ejections (CMEs), which generally do not consider the restructuring of magnetic and flow fields in the photosphere due to the assumed line-tying effect. Magnetic shear build up and associated rapid change of vector magnetic field in the flaring region, especially of the transverse field across the PILs, were firstly observed in photospheric magnetographs over two decades ago [224, 227]. Based on the principles of energy and momentum conservation, Hudson et al. [89] and Fischer et al. [61] quantitatively investigated the back reaction on the solar surface and interior as a result of the coronal field evolution (specifically, implosion) after energy release, and pointed out that flares/CMEs would make the photospheric magnetic field become more horizontal at the flare-related magnetic PILs. The authors formulated the resulted changes of the integrated vertical (downward) and horizontal Lorentz force exerted on the photosphere from the corona, and suggested that the former may energize seismic waves and the latter may cause plasma bulk motions.

Thus far, these predictions of the back reaction theory have been substantiated by many aspects of observational results of flare-related photospheric magnetic field changes, including the rapid and permanent step-like increase of horizontal field at flaring PILs (e.g., [224, 120, 236, 228, 118, 200, 157, 199]), possible linkage to the excitation of seismic waves (e.g., [5, 117]), and sunspot displacement and rotations (e.g., [7, 237, 122]). The downward collapse of coronal current systems

presumably due to coronal implosion following flares/CMEs is also corroborated by time sequence of nonlinear force-free field models (e.g., [200, 117]) and is reflected in MHD simulations (e.g., [57, 58]).

1.2.2 Flow Field Evolution

Besides magnetic field variations, changes of sunspot structure in white light have also been found to be consistent with the back reaction scenario. Notably, sunspot penumbrae are a direct indication of horizontal photospheric field, with their fibrils following the direction of magnetic azimuth [185]. The outward plasma flows along fibrils (known as Evershed flows) can have a velocity up to $\sim$4 km s^{-1} in photosphere from spectroscopic observations (e.g., [186]), and can reach up to $\sim$8 km s^{-1} in chromosphere [13], while optical penumbral flows measured by flow tracking methods based on imaging observations generally result in a velocity on the order of $\sim$1 km s^{-1} (e.g., [202, 217]). The penumbral structure and its carried flows are governed by the magnetic field strength and especially the field inclination, as revealed by previous observations (e.g., [90, 51]) and MHD simulations [165, 103]. Thus, the expected more horizontal photospheric field configuration in response to the coronal restructuring as described above is strongly evidenced by observations of flare-related darkening and/or formation of penumbral structure, together with strengthened horizontal field and decreased inclination angle, near central flaring PILs [120, 49, 32, 113, 232, 256]. It can be noted that these works studied the structural evolution of penumbra mainly based on the overall intensity of penumbral segments, without examining in detail the associated penumbral flows.

Understandably, studying the flare-related flow field evolution requires high-quality, high-resolution observations that cover the entire flare interval, which are, however, relatively rarely available. Using high-resolution ($0.2''$) G-band images from Hinode, Tan et al. [202] observed enhancement of the central penumbral region of

the δ spot in NOAA AR 10930 associated with the December 13 X3.4 flare. By employing the local correlation tracking (LCT) technique, the authors were able to detect shear flows (i.e., opposite-directed flows at the two sides of the PIL) in the penumbral region, which exhibited a significant decrease associated with the flare, probably due to the magnetic restructuring and energy release. Importantly, shear flows can contribute to the build up of magnetic nonpotentiality in flaring regions [79, 6, 241] and thus flare triggering, as in high resolution they show a close spatial proximity to the initial flare kernels [259, 53]. It is obvious that more studies of both the flow and magnetic field evolution in penumbrae can help to shed further light on our understanding of the photosphere-corona coupling related to flaring activities.

1.3 Features of Quiet Sun Reconnection

With improvement of spatial resolution of solar observations over the past decades, detection of small-scale features are made possible, which substantially advances our understandings of magnetism of quiet Sun photosphere. The quiet Sun appears to be dominated by granulation in the continuum images and the transient nature of their webbing magnetic field leads to magnetic flux accumulation in the photosphere through horizontal photospheric advection. Magnetic fluxes raised into the solar surface by granulation are therefore the potential candidates of chromospheric heating.

Magnetic concentrations of kG field in the quiet sun photosphere forms boundaries of supergranulation, of which each cell has a typical horizontal scale of 30–35 Mm and a lifetime of 24–48 hours. Supergranules often exhibit strong horizontal flow of 300–400 m s^{-1} and very weak vertical flow of 20–30 m s^{-1} [166]. The boundary of supergranulation is called network [176], which expands with convective evolution and eventually transports flux to the chromosphere [184, 16]. As outlined by the internetwork inside the supergranule cells, granulation shows more

dynamic evolution, with a lifetime of 5–10 minutes and a horizontal length scale of 0.5–2 Mm [167]. Analysis of high-resolution magnetograms found well balanced magnetic energy budget and release in quiet Sun, where the magnetic flux appearance rate in internetwork regions is 120±3 $Mx\ cm^{-2}\ day^{-1}$ ($3.7\pm0.4\times10^{24}\ Mx\ day^{-1}$ over the entire solar surface) and flux disappearance rate from the internetwork is 125±6 $Mx\ cm^{-2}\ day^{-1}$ ($3.9\pm0.5\times10^{24}\ Mx\ day^{-1}$) [75].

Small-scale reconnection in the quiet Sun is often accompanied with magnetic flux decay involving cancellation of opposite polarities and drainage of internetwork elements. Chromospheric responses of the enhanced photospheric magnetic activities are jets and spicules. Particularly, spicules and macrospicules are pervasive small-scale, thin plasma features that are often seen in strong chromospheric spectrol lines, such as Hα and Ca II lines, against solar disk (e.g., [265, 258, 106, 175]) as well as off the limb (e.g., [225, 257, 42, 198, 14]). The discovery of inverted Y-shaped Ca jets by high-resolution Hinode/SOT observation revealed that the small-scale jets occur frequently associated with ubiquitous reconnection in the lower atmosphere (photosphere, chromosphere) [179]. The typical apparent velocity of Ca jets is 10–20 $km\ s^{-1}$. Study of Ellerman bombs in the quiet Sun shows that chromospheric counterparts of the small-scale jetlike ejections have apparent velocity of 50–80 $km\ s^{-1}$ [164]. While the ultimate energy source comes from convection zone, it is increasingly clear that the direct energy deposit for coronal/chromospheric heating is resulted from recurrent small-scale reconnection by stressing their footpoints. Such prominent features play a crucial role in heating chromosphere by releasing magnetic energy at a rate of $0.2–1\times10^{24}\ ergs\ s^{-1}$ and cancelling flux at a rate of $10^{15}\ Mx\ s^{-1}$ in the cancellation regions [153]. Study of the small fraction of magnetic structure in photosphere is a key apsect of resolving the heating mechanisms that cause solar wind acceleration.

1.4 Scientific Goal and Dissertation Outline

Since the discovery of magnetic field in sunspots, it is evidently confirmed in modelling and observational studies that the most dynamic solar activities such as flares and CMEs are originated by the complexity of evolving magnetic fields. The evolution of photospheric flow and magnetic fields before and after flares can provide important information regarding the flare triggering and back reaction processes. However, such studies on the flow field are rare due to the paucity of high-resolution observations covering the entire flaring period. On the other hand, magnetic free energy build up in the corona are closely related to reconnection processes such as those in flux emergence and cancellation in the lower atmosphere. While such evolution of magnetic structures occurs in various scales, it is worth noting that small-scale flux cancellation is ubiquitous in the photosphere and plays an important role in heating corona.

This research takes advantage of the exceptionally high-resolution data of the ground-based Goode Solar Telescope, focusing on the magnetic structure and flow fields evolution in the photosphere. Studies are conducted with the unprecedented high-resolution magnetic measurements taken by GST/NIRIS, together with sharp TiO continuum images by GST/VIS and supplementary data at multiple wavelengths from SDO/HMI, SDO/AIA, and GOES. For statistical analysis of the small-scale magnetic properties, an advanced magnetic feature tracking method is employed to characterize the intermittent magnetic reconnection driven by the evolution of magnetic elements.

The scientific goal of this dissertation is to understand photospheric magnetic field changes by investigating high-resolution magnetic structures in both flare active regions and ephemeral regions. With the most advanced data from the ground observation accomplished by BBSO/GST, this dissertation addresses the science questions by studying the important role of magnetic field in solar activities from two

aspects, flare-induced magnetic changes in restructuring photosphere and small-scale magnetic evolution associated with energy release using case studies and statistical analysis. As much as the study of space weather concerns, the source of solar wind acceleration can be traced back to the ubiquitous photospheric magnetic structures and reconnection in the lower atmosphere, which leads to the key science questions: What are the rapid changes of magnetic field and flow field in response to flare eruptions, what is the significant morphological and magnetic properties of small-scale magnetic evolution, and to what extent the energy released in this kind of impulsive magnetic reconnection can contribute to coronal heating and acceleration of solar wind.

CHAPTER 2

DATA SOURCES AND OBSERVATIONS

2.1 Data Sources

Solar imaging in the near-infrared wavelengths is accessible to ground-based observations and is widely utilized for accurate magnetic field measurement because of Zeeman sensitivity [160]. With the improvement of spatial and temporal resolution of magnetic field measurement, fine structures of the magnetic field that are essential regarding to the magnetic energy buildup in low atmosphere and its linkage to a flare or jet can be observed comprehensively. Due to transmittance of earth atmosphere, only wavebands of visible light, near-infrared and radio waves are accessible in ground observations. The image quality is greatly advanced by large aperture, adaptive optics control system, and post-processing techniques (e.g., speckle reconstruction [251]). Hence, high-resolution optical and infrared observations gain popularity in the study of solar activities with the state-of-the-art ground-based telescopes. On the other hand, X-ray and UV/EUV radiations are completely absorbed in the earth's mesosphere (∼30–80 km) and thermosphere (above 80 km), respectively, which makes them impossible to be received on the ground.

2.1.1 Ground-based Observations

This dissertation is accomplished with the unprecedentedly high-resolution data taken by the Goode Solar Telescope (GST), given its upgraded AO system for steady quality and coverage of long observing period. Since completion of telescope upgrade, GST entered its commission phase in January 2009. This telescope performs diffraction-limited observations in an all reflecting off-axis Gregorian system with a 1.6 m clear aperture. Routine observation is conducted by Nasmyth focus filtergraphs which achieve high spatial resolution broad/narrow band photometric measurement

in visible and near-infrared wavelengths. The utilized instruments are Broad-band Filter Imager (BFI), Visible Imaging Spectrometer (VIS), and Near Infra-Red Imaging Spectropolarimeter (NIRIS). All available optical observations with each instrument are listed in the Table 2.1.

For the study of solar photospheric dynamics, data obtained by GST ground observations contain TiO continuum (7057 Å with 10 Å bandpass) by BFI that resolves photopsheric granulations and sunspots, Hα of eleven line positions (0, $\pm$0.2, $\pm$0.4, $\pm$0.6, $\pm$0.8, $\pm$1.0 Å) around the central line (6562.8Å with 0.07 Å bandpass) that identify filaments, jets, and spicules, and full spectroscopic measurement, i.e., full Stokes I, Q, U, V, obtained in Fe I 1.56 μm doublets. BFI captures 100 frames per each burst in cadence of 15 s in all available lines, and VIS captures 60 frames (25 best) per each burst in every line position.

The latest adaptive optics system, AO-308 on GST telescope, was installed and in effect since 2013 [180]. AO-308 uses a 357 actuators deformable mirror and its wave front sensor has 308 sub-apertures, which provide high order correction of Earth's atmospheric seeing. With speckle-masking image reconstruction [251], angular resolution of GST observations is designed to reach diffraction limit from 0.4 μm to 1.7 μm wavelengths in a FOV of over 85″.

NIRIS uses dual Fabry-Pérot etalons of 100mm aperture to simultaneously capture left and right polarization states side-by-side, with each taking 1024×1024 pixels of the 2048×2048-pixel Teledyne camera, achieving a image scale of 0.083″/pixel. In 85″ round field of view, the instrument scans over 100 line positions in each full spectroscopic measurement at a cadence of 10 s, and in each line position the polarimetry is measured at 16 sampled phase angles by rotating the waveplate. NIRIS covers spectral wavelength range from 1000 to 1700 nm, with spectral resolving power ($\lambda/\Delta\lambda$) in the order of 10^5. There are two particular interference filters, 1083 nm and 1565 nm, and NIRIS can be operated in four modes: polarimetric mode, spectroscopic

Table 2.1 Operating Instruments and Available Wavelengths in BBSO

Instrument	Filter[a]	Wavelength (bandpass)	FOV	Image scale (/pixel)	Angular resolution	Cadence
Hα full-disk	Zeiss	6562.8Å (0.25Å)	full-disk	1″	1″	1 min
BFI	TiO	7057Å (10Å)	70″	0.034″	0.09″	15 s
	red continuum	6684Å (4Å)	70″	0.034″	0.09″	15 s
	G-band	4305Å (5Å)	55″	0.027″	0.06″	15 s
VIS	Hα	6562.8Å (0.07Å)	70″	0.034″	0.1″	15 s/line
	Fe I	6300Å (0.07Å)	70″	0.034″	0.1″	15 s/line
	Na I	5890Å (0.07Å)	70″	0.034″	0.09″	15 s/line
NIRIS	Fe I	15648Å (0.1Å)	85″	0.083″	0.24″	10 s/Stokes measurement
	He I	10830Å (0.05Å)	85″	0.083″	0.17″	10 s/Stokes measurement

[a]Instruments used in the dissertation are shaded in the table.

mode, Doppler mode (a few selected spectral points), and photometric mode. In

this dissertation, polarimetric mode is used to obtain a full spectral profile with polarization optics.

Magnetic features in the deepest photospheric layers are explored by the highly Zeeman sensitive ($\sim 10^{-4} I_c$) Fe I line doublet at 1564.85 nm and 1565.29 nm, which are close to the opacity minimum of 1.6 μm. The Milne-Eddington inversion of these data provides magnetic field product. When the system is operated in a fixed-phase-angle, dual-polarization mode allows speckle reconstruction of Stokes I and V for diffraction-limited line-of-sight magnetic field diagnostics.

2.1.2 Space-based Observations

Since the launch on February 11, 2010, SDO provides views of the Sun's atmosphere in multi-layers from photosphere to active region corona. There are two imaging instruments utilized in this space-based observatory, the Atmospheric Imaging Assembly (AIA; [111]) and Helioseismic and Magnetic Imager (HMI; [172]), which in total image the Sun in 12 different wavelengths. AIA consists of four telescopes of 4096×4096 pixel CCD that employ normal-incidence, multilayer-coated optics to take full-disk solar images including the entire corona in ten wavelengths from 94 Å to 4500 Å nearly simultaneously, at a resolution of $\sim 0.6''$ and a cadence of 12 s (at EUV wavelengths) to 24 s (at UV wavelengths). It provides a high signal-to-noise ratio in ∼3 s exposure, which reaches as high as 10,000 in the high-temperature channels and 100 in the low-temperature channels in quiet Sun. The narrow-band imaging of seven EUV bands is centered on the specific lines: Fe XVIII (94 Å), Fe VIII, XXI (131 Å), Fe IX (171 Å), Fe XII, XXIV (193 Å), Fe XIV (211 Å), He II (304 Å), and Fe XVI (335 Å). The temperature diagnostics of the EUV emissions is in the range of 6×10^4–2×10^7 K. Particularly, EUV images at 171 Å can detect emissions in emergent magnetic loops in the quiet Sun corona, and EUV images at 193 Å are usually used for the identification of coronal holes due to its capability of hot coronal material

(10^6 K) detection. UV images observed at C IV line (1600 Å) and in continuum (1700 Å) detect emissions in the upper photosphere of 10,000 K and emissions in the solar surface of 4500 K, respectively, where precursors of solar flares are detectable.

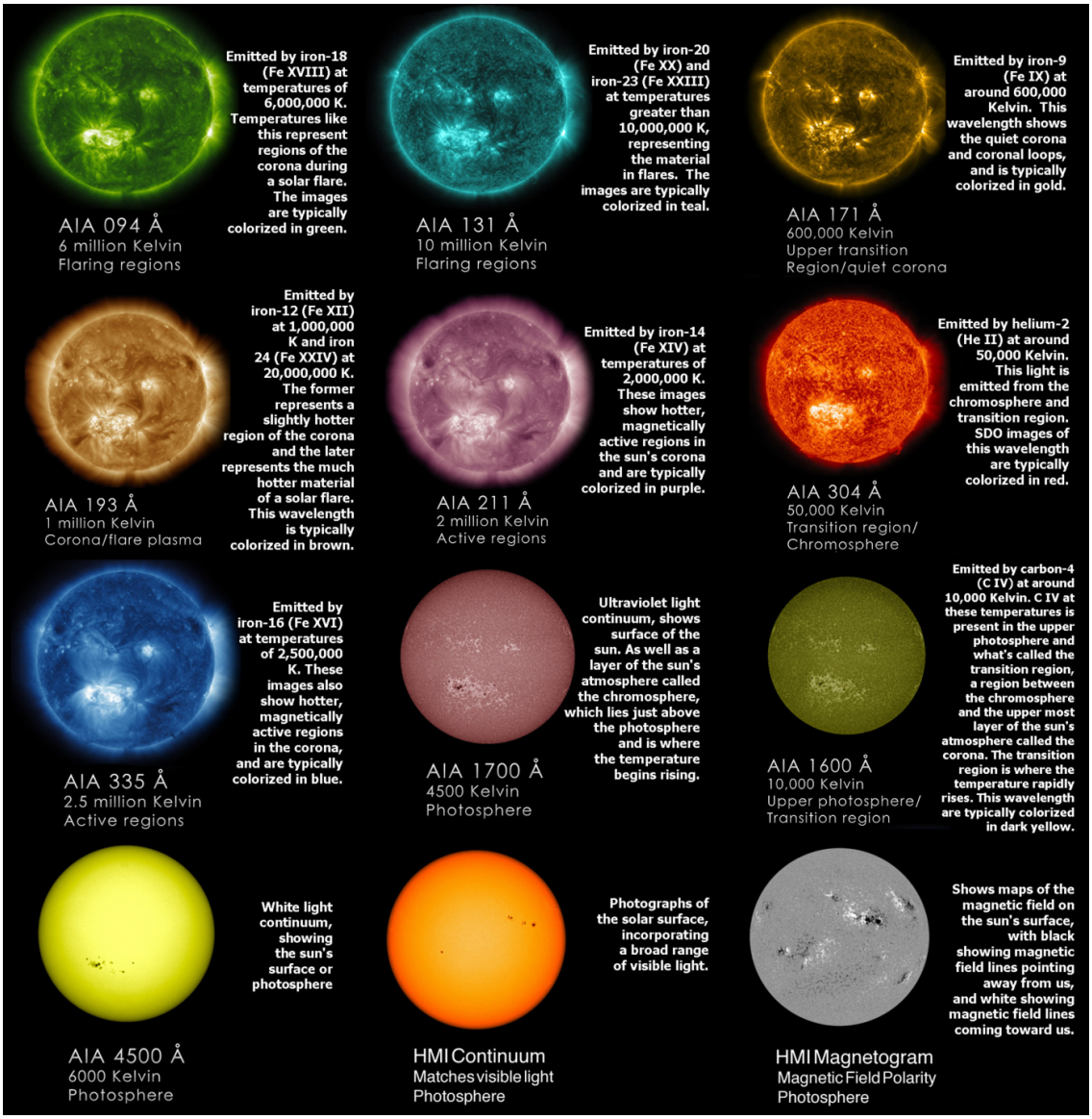

Figure 2.1 Solar images taken in different wavelengths, by AIA and HMI on board the SDO. In the dissertation, HMI magnetograms of 135 s cadence and AIA images at 171, 193, and 1700 Å are used for the study of magnetic evolution and UV/EUV responses, respectively.
Credit: NASA/SDO/Goddard

HMI observes the full disk solar photosphere at 6173 Å Fe I absorption line with a resolution of 1″. There are four main types of data available: dopplergrams on the solar surface, broad-band continuum, line-of-sight magnetograms, and vector magnetic field products. HMI contains two identical 4096×4096 pixel CCD cameras, which can be read out in about 2.3 seconds. Filtergram cadence of each camera is 3.75 s. Summation of all the scans through six spectral tuning positions gives the overall cadence of Dopplergrams, intensity, and LOS magnetograms at best 45 s. Vector magnetic field is measured by a set of waveplates at different angle for detecting Stokes I, Q, U, V in six observed wavelengths spanning the range ±172.5 mÅ around the central wavelength of 6173 Å. The basic cadence of vector field sequence therefore is 135 s. The vector field is computed using the Very Fast Inversion of the Stokes Vector (VFISV) algorithm based on HMI Stokes parameters [83].

CHAPTER 3

EVOLUTION OF PHOTOSPHERIC FLOW AND MAGNETIC FIELDS ASSOCIATED WITH THE M-CLASS FLARE

3.1 Introduction

Since the discovery of rapid and permanent magnetic change in the photosphere associated with flare eruptions [224, 197], impact of the large-scale reconnection on the photospheric structural evolution is broadly investigated. Recent ground-based observation reported the sudden flare-induced rotation of a sunspot using the unprecedented resolution of the recently commissioned 1.6 m Goode Solar Telescope (GST; [71, 24, 70, 216]) at Big Bear Solar Observatory (BBSO) with complementary magnetic data from SDO [123]. It is proposed the downward Poynting flux is injected into lower atmosphere from corona, by which the surface Lorentz force change plays an important role in driving the sunspot rotation.

In this work, we take advantage of the unprecedented resolution of the GST observations to investigate the photospheric flow field associated with the 2015 June 22 M6.5 flare, and also study the corresponding magnetic field using data from the Helioseismic and Magnetic Imager (HMI; [172]) on board the SDO. We concentrate on the structural evolution of penumbra near the flaring PIL, and make quantitative characterizations of the flare-related changes of the flow and magnetic properties. We compare our results with previous studies and discuss their implications in the context of the back reaction theory. The structure of this chapter is as follows. We introduce the observations and data analysis methods in Section 3.2, and describe the observational results in Section 3.3. Major findings are summarized and discussed in Section 3.4.

3.2 Observations and Data Processing

With excellent seeing condition, BBSO/GST achieved diffraction-limited imaging on 2015 June 22 during ∼16:25–22:50 UT, thanks to the high-order AO-308 system (with 308 sub-apertures) and speckle image reconstruction. The obtained multiwavelength observations have revealed many interesting properties of the fully covered M6.5 flare, including flare precursors, sunspot rotation, and various fine structures [230, 122, 100]. The essential data used in this study for tracking the photospheric flows are the images taken by the GST's Broad-Band Filter Imager at the TiO band (7057 Å, 10 Å bandpass), a proxy for the continuum photosphere, using a 2048 × 2048 pixels CCD camera with a ∼70″ field of view (FOV). The spatial resolution (at diffraction limit $\theta = \lambda/D$) of TiO images is 0.09″, and the temporal cadence is 15 s. As for magnetic field, we used 135 second cadence vector magnetograms from HMI's full-disk vector field data product [83, 199], which is provided by the Joint Science Operations Center. The pixel scale of HMI data is 0.5″. The TiO images and magnetograms are aligned based on sunspot and plage features, with an alignment accuracy within ∼0.3″, which is the best accuracy by using interpolation. Also used are the 25–50 keV hard X-ray (HXR) time profile from the Fermi Gamma-Ray Burst Monitor (GBM; [135]) for studying the timing of flare energy release, and 1700 Å continuum (5000 K) images from the Atmospheric Imaging Assembly (AIA; [111]) on board SDO for disclosing the flare precursor brightenings in the low atmosphere.

To derive the flow field on photosphere based on the TiO observation, we aligned TiO images to sub-pixel precision, normalized the intensity to that of a quiet-Sun area, and applied a 2 × 2 image binning to increase the S/N ratio; we then applied the differential affine velocity estimator (DAVE; [173]), which is a demonstrated technique for flow detection and tracking. Here we set the tracking window to 25 pixels, trying to include enough structure information and at the mean time achieving a good resolution. We estimate quantitative uncertainty by analyzing data with tracking

window range from 20 to 30 pixels, which results in a maximum relative standard deviation (RSD) as 5%. For a validity check, we repeated the flow tracking using the LCT method [146], which produced similar results. To minimize the effects of atmospheric seeing and five-minute period photospheric oscillation, a five minute running average was further made to the derived DAVE velocity vectors.

3.3 Analysis and Results

The flare-productive NOAA AR 12731 appears in the $\beta\gamma\delta$ configuration on 2015 June 22. The M6.5 flare of interest occurred in this region starts at 17:39 UT in GOES 1–8 Å soft X-ray flux, and shows three main peaks in Fermi 25–50 keV HXR flux at 17:52:31, 17:58:37, and 18:12:25 UT [122]. The separating two ribbons of the flare originate from penumbral regions very close to the PIL, and subsequently sweep across the main sunspot umbrae of opposite magnetic polarity [230, 100]. In this work we focus on the evolution of the central penumbral region of this δ configuration from the pre- to post-flare states. Similar to previous studies, stepwise changes of physical properties are observed and are quantified by fitting to a step function [197]

$$B(t) = a + bt + c\{1 + \frac{2}{\pi}\tan^{-1}[n(t - t_0)]\} \ , \tag{3.1}$$

where a and b describe the strength and evolution of the background, t is time, c represents half amplitude of the step, n controls the slope of the step, and t_0 is the middle point of the step. In this equation the time of the start of the change is $t_0 - 0.5\pi n^{-1}$.

3.3.1 Evolution of Growing Penumbra Region

From TiO continuum observation, one can easily identify the most prominent flare-related penumbral evolution, that is, one segment of the central penumbra lying in the negative field becomes much enhanced (in terms of flow dynamics) and extends

to the north, with a close temporal relationship with the flare. This can be readily seen by comparing the pre- (17:34 UT) and post-flare (19:22 UT) TiO images as shown in Figure 3.1(a) and (b), respectively. The difference image in Figure 3.1(c) (post-flare minus pre-flare state) displays a main darkened region R (encompassed by the red contour), which corresponds to the newly formed portion of the penumbra that was occupied by photospheric granulations. In Figure 3.2, we show the maps of flow vectors and azimuth derived with DAVE in the pre- and post-flare states. It is evident that after the flare, the flow vectors strengthen vastly, not only in the northern newly formed penumbral region R but also in the previously existing, common penumbral area; moreover, the azimuth of flows become more uniform, predominantly toward the north direction. An accompanying gradual increase of penumbral flow speed is shown in time-lapse flow maps. A similar overall enhancement of horizontal magnetic field across the existing and newly formed penumbra regions is also observed (cf. Figure 3.1(d) and (e)).

To better depict the temporal evolution of the penumbral structure, in Figure 3.3(a) we construct the space-time slice image for a slit (marked as the red line in Figure 3.1(a)-(c)) along the penumbral growing direction, based on the TiO intensity images, and estimate speed of segmental motions of penumbra. We see that this penumbral segment begins to grow rapidly toward north from around the time of the first HXR peak ($\sim$17:52 UT), with its northern end of fibrils extending for a distance of $2.6''$ ($\pm 0.3''$) in about 20 minutes (from which we found that the north end of fibrils extends at an average speed of $1.5(\pm 0.05)$ km s^{-1}); later on, it continues to slowly extend northward for about two hours (at an average speed of $0.17(\pm 0.01)$ km s^{-1}). We also trace several prominent evolving fibril features of the main penumbral body using red lines in Figure 3.3(a), which exhibit that after the first HXR peak, the penumbral flows become more conspicuous, with a velocity reaching up to $2.3(\pm 0.12)$ km s^{-1} (estimated based on the slope of red lines). The evolution

of flow velocity is also directly manifested in Figure 3.3(b), which is the space-time slice image for the same slit but built upon the time sequence of the velocity field derived with DAVE. The penumbral flows strengthens from an average velocity of $0.8(\pm0.04)$ km s^{-1} at 30 minutes before the first HXR peak to $2.2(\pm0.11)$ km s^{-1} at 90 minutes afterwards within the region R edges, which is comparable with the velocity estimation using the time slices. It is pertinent to point out that this velocity ($2.2(\pm0.11)$ km s^{-1}) of penumbral flows is about twice as large as that measured based on Hinode G-band images [202], presumably due to (1)the higher resolution of the TiO data used in the present analysis, and (2) intrinsic property of this specific active region we studied.

In Figure 3.4, we further plot time profiles of mean TiO intensity, flow velocity, horizontal field strength, and magnetic inclination angle (defined as the angle of magnetic field vector with respect to solar surface) of the newly developed penumbral region R, and compare their timings with the HXR emission. The results show that after about the first HXR peak, the region R begins to show an increase of penumbral flow velocity together with a penumbral darkening, an increase of horizontal magnetic field strength, and a decrease of field inclination angle. Specifically, according to the step function fittings, starting from 18:00 UT the intensity decreases $15(\pm2)\%$ in 30 minutes; meanwhile, the horizontal field increases $150(\pm15)$ G in $\sim$18 minutes from 17:50 UT to 18:08 UT, with inclination angle decreasing $5(\pm0.5)^\circ$ in the same time period. Then horizontal field continues with a gradual increase of $200(\pm20)$ G from 18:08 UT to 19:40 UT, while inclination angle decreases $6(\pm0.6)^\circ$ for that time. In contrast, the flow velocity evolves more gradually, leading to an increase of $1.2(\pm0.1)$ km s^{-1} from 30 minutes before the first HXR peak to 90 minutes afterwards.

3.3.2 Evolution of Shear Flow near PIL

By examining the time sequence of TiO flow maps, we also find pronounced shear flows along the PIL in this flaring region. As can be seen in Figure 3.2(a), around region P the flows in the eastern side of the PIL pointing toward southwest while those in the western side of the PIL pointing toward northeast, constituting a clear shear flow pattern. In the azimuth map computed using the derived flow vectors (Figure 3.2(c)), the shear flow pattern can be recognized as a green-magenta feature with the central dividing line running along the PIL. We note that (1) this shear flow region is co-spatial with a "magnetic channel" structure (with multiple polarity inversions) that can be identified using high-resolution magnetic field observations for this region [230], and is also adjacent to a low-atmospheric, flare precursor brightening kernel K (cf. Figure 3.1(f) and 3.2(a)(c)). Such a spatial correlation between shear flows and initial flare kernels was also found before using high-resolution observations [259, 53], suggesting that the shear flow may contribute to the flare triggering process. (2) Most intriguingly, the shear flow enhances and its region expands substantially after the flare (cf. Figure 3.2(a)(c) and (b)(d)). For a quantitative analysis, we define the magnitude of shear flow velocity as $v_{\rm shear} = \overline{v}_{\rm pos} - \overline{v}_{\rm neg}$, where $\overline{v}_{\rm pos}$ ($\overline{v}_{\rm neg}$) is the flow velocity in the positive (negative) field region, in the direction parallel to the PIL. For the results in this study, positive value of $v_{\rm shear}$ represents counterclock-wise direction of shear. In Figure 3.5(b), we plot the time profile of the shear flow velocity averaged over the region P (in Figure 3.2(d)). A gradual increase of shear flow is seen from the first HXR peak, and later reaches $0.9(\pm0.05)$ km s^{-1} at 19:30 UT. This magnitude of shear flows is $50(\pm5)\%$ larger than that of the maximum shear flows in the event of Tan et al. [202].

The shear flow region P has an insignificant intensity variation (within 5%) associated with the flare (Figure 3.5(a)). Nevertheless, it still shows appreciable, stepwise changes of magnetic properties. Fittings using a step function indicate that

starting from 17:50 UT (co-temporal with the first HXR peak), the horizontal field strength increases 220(±20) G from 17:50 UT to 18:20 UT (Figure 3.5(c)), while the field inclination angle decreases 5(±0.5)° from 17:50 UT to 18:20 UT (Figure 3.5(d)). Compared to the growing penumbral region R, the transition time of horizontal field changes in shear region P is longer and followed by a flater gradual increase.

3.4 Conclusions and Discussion

We have presented a detailed study of the structural evolution of photospheric flow and magnetic fields associated with the 2015 June 22 M6.5 flare, concentrating on the central penumbrae of the δ region around the flaring PIL. We tracked the penumbral flow field with the DAVE method using high-resolution TiO images from BBSO/GST, and also analyzed the associated magnetic field using SDO/HMI vector magnetograms. The main results are summarized as follows.

1. Beginning from the first HXR peak, one segment of penumbra lying in the negative field experiences a distinct grow, extending northward at 1.5 (±0.05) km s^{-1} for a distance of 2.6″(±0.3″); meanwhile, the flow velocity within the entire penumbral region becomes more pronounced, gaining a 115(±10) % increase reaching up to 2.2(±0.11) km s^{-1} at ∼90 minutes after first flare peak. These structure and flow field evolutions are accompanied by a step-like increase of horizontal magnetic field by 150(±15) G and decrease of inclination angle by 5(±0.5)° in 18 minutes from 17:50 UT to 18:08 UT.
2. A region of shear flow at the flaring PIL is found next to the location of a flare precursor brightening, and expands significantly after the flare. From the first HXR peak, the shear flow velocity increases gradually by 0.4(±0.1) km s^{-1} from 0.5(±0.05) km s^{-1} at 17:30 UT to 0.9(±0.05) km s^{-1} at 19:30 UT. As for magnetic field properties in the shear flow region, the horizontal field strength increases 220(±20) G while the inclination angle decreases 5(±0.5)° from 17:50 UT to 18:20 UT, both following a stepwise fashion. In comparison with the extending penumbral segment, the transition time of step-like magnetic field changes in the shear flow region is ∼10 minutes longer.

Our results of the strengthening of penumbral structure at the center of δ region, the associated increase (decrease) of horizontal field (inclination angle), and their close timing relationship to the flare energy release strongly favor the back reaction of

coronal fields as the underlying cause, which results in a more horizontal configuration of photospheric field. While most other work only deals with the flare-related overall intensity change of penumbral structure, we are able to study the evolution of penumbral flow field owing to the high-resolution BBSO/GST data. We show that although noticeable intensity darkening is only observed in the newly formed penumbral portion, the strengthening of penumbra is predominantly manifested as the enhancement of penumbral flow velocity and enlargement of penumbral area. The inconsistency of our results with the claim of darkening of central penumbral feature in some previous studies may due to the limitation of the used low-resolution images (e.g., [120]) and also the complexity of the central penumbral area near PIL [230].

The also revealed spatial correlation between the shear flow and flare precursor brightening kernel corroborates the importance of photospheric flow field in triggering flares. In this event, the precursor brightenings are caused by the reconnection between emerging fluxes in the magnetic channel with ambient large-scale sheared loops [230]. The produced lower-lying fields near the PIL could be readily subject to the downward collapse of coronal fields [118], which may explain the observed more rapid magnetic field changes in the shear flow region. We also remark that the change of shear flows associated with flares is an observational fact of particular interest but its study has been lacking. Like penumbral enhancement, we also tend to attribute the observed increase of shear flow after the present flare to the more horizontal photospheric fields due to back reaction. An increase of shear flows near the PIL was also found by Deng et al. [53] associated with an X10 flare in NOAA AR 10486, although the shear flows are not located in the central penumbra with accompanied magnetic field changes. To our knowledge, the study most closely related to our work was conducted by Tan et al. [202] on an X3.4 flare in NOAA AR 10930. Contrarily, the authors saw a rapid decrease of shear flow in the central penumbral region, and explained it as a signature of magnetic energy relaxation between the two major

magnetic polarities of the δ spot, one of which shows a continuous rotation before the flare. Such a relaxation could be viewed in line with the finding of sudden release of magnetic shear in the horizontal direction along the PIL of δ spots, as reported by Wang [226]. We speculate that the evolution of shear flows, due to their special locations along the flaring PILs, could be affected by both the back reaction from the above corona and the response of photospheric magnetic polarities to the energy release. The back reaction creates sheared flux system near the surface [227] that may be reflected as increased shear flow, while relaxation of large scale system may reduce shear flow.

In summary, high-resolution observations of photospheric flow field evolution from pre- to post-flare stages, together with the analysis of magnetic field changes, will be valuable in advancing our understanding of flare triggering and back reaction processes. Further studies in this direction are highly desired and would certainly contribute to the science preparation in high-resolution flare studies for the upcoming 4 m Daniel K. Inouye Solar Telescope.

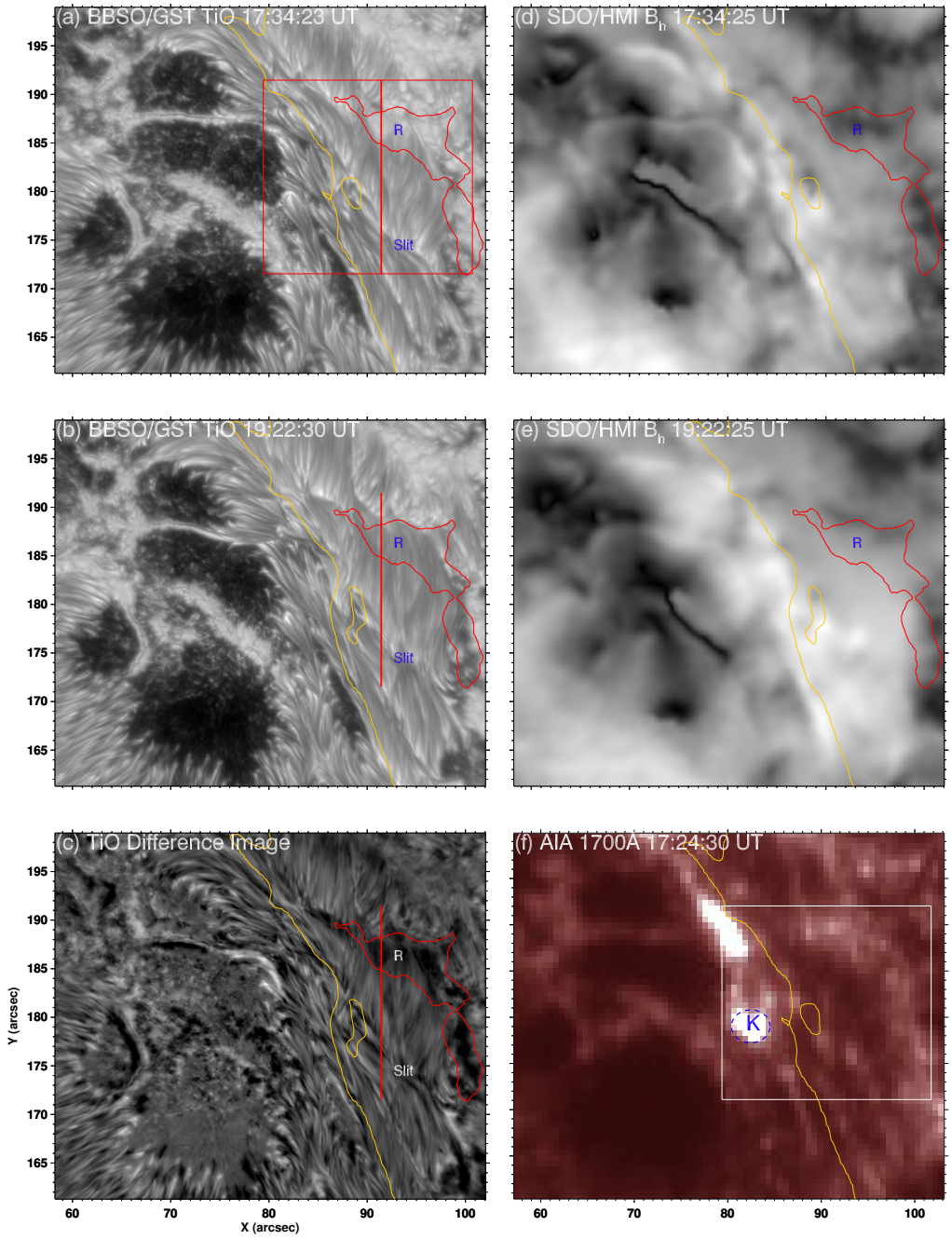

Figure 3.1 Event overview. (a–c) Pre-flare, post-flare, and difference (19:22:30 UT frame subtract 17:34:23 UT frame) BBSO/GST TiO images, overlaid with the red contour indicating the newly formed penumbral region R determined based on the difference image. The vertical red line marks the slit used for the space-time slice image shown in Figure 3.3. (d–e) Pre- and post-flare SDO/HMI horizontal magnetic field maps, also overplotted with the contour of region R. (f) Pre-flare SDO/AIA 1700 Å image, showing flare precursor K. The yellow contours superimposed in all panels represent the co-temporal PILs. The boxed region in (a) and (f) indicates the FOV of Figure 3.2.

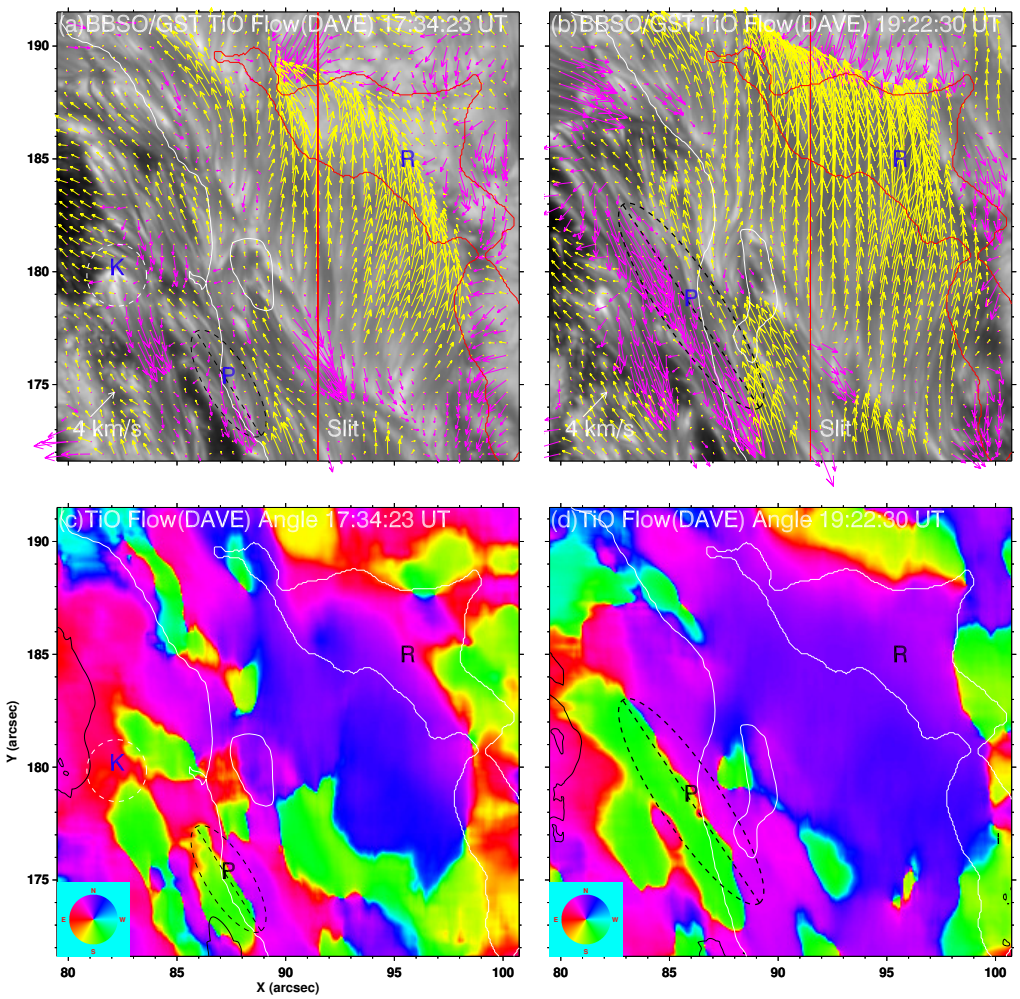

Figure 3.2 Flow field in BBSO/GST TiO band. (a) and (b) Pre-flare (at 17:34:23 UT) and post-flare (at 19:22:30 UT) TiO images overplotted with arrows illustrating the flow vectors derived with DAVE. For clarity, arrows pointing northward (southward) are coded yellow (magenta). The white and red contours denote the PIL and the region R (see Figure 3.1), respectively. (c) and (d) Azimuth maps of corresponding flow vectors in (a) and (b), also overplotted with the PIL, precursor kernel, and region R contours. The shear flow region P showing the most obvious flare-related enhancement is outlined using the dashed ellipse, with its major axis quasi-parallel to the PIL.

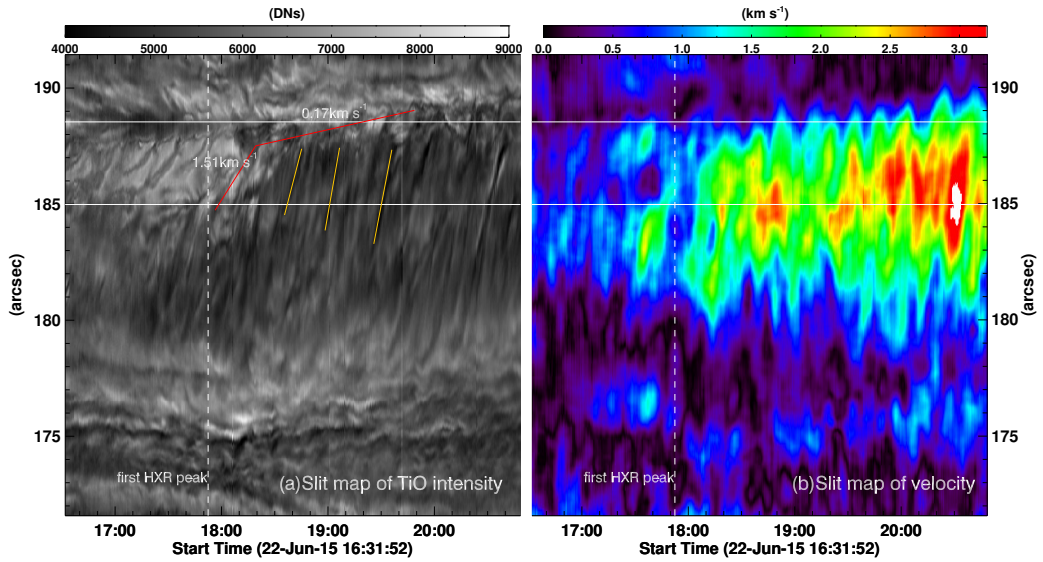

Figure 3.3 Space-time slice image based on BBSO/GST TiO intensity images (a) and the derived time sequence of DAVE velocity field (b). The slit is marked as the red vertical line in Figure 3.1(a)–(c). The vertical dashed line denotes the time of the first HXR peak at 17:52:31 UT, the horizontal solid line denotes intersections of slit with region R in Figure 3.2(a) (b). The overplotted red lines in (a) trace several prominent evolving penumbral fibril features, and are used to estimate the flow velocity based on their slope.

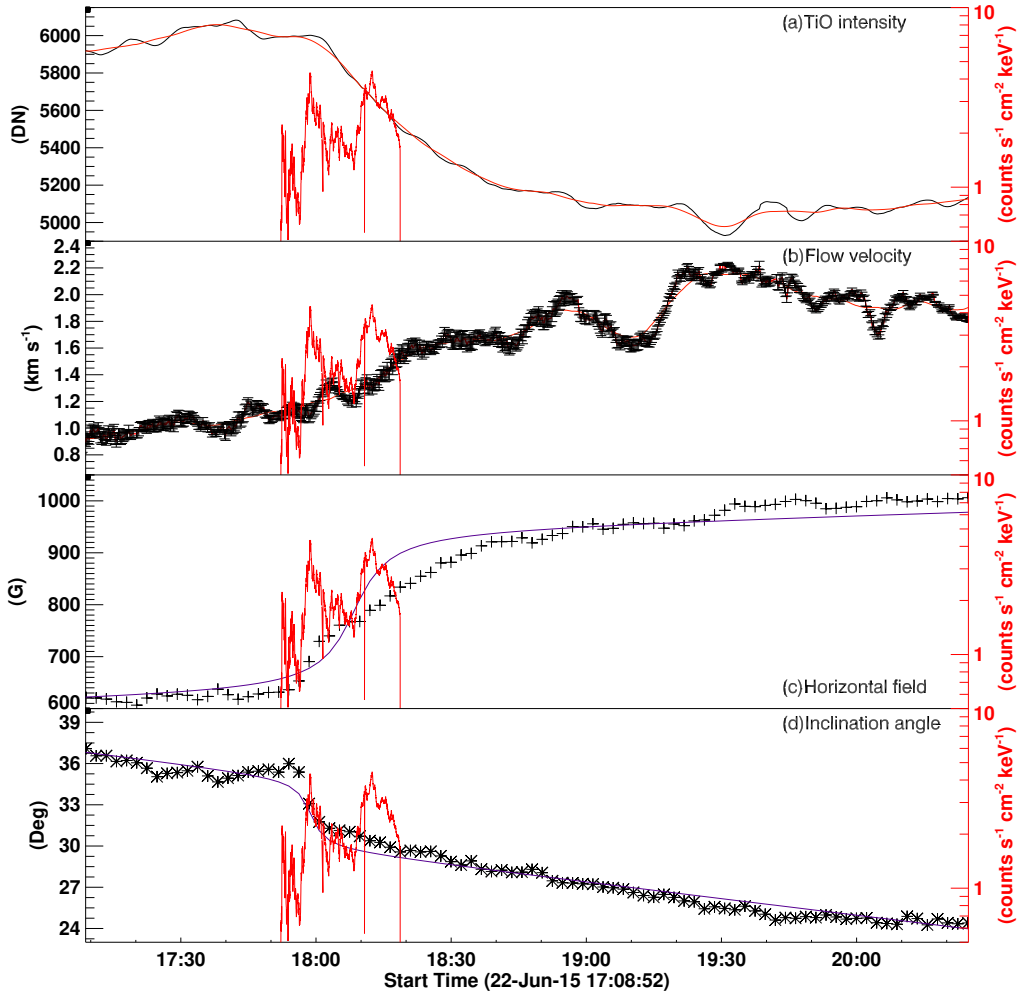

Figure 3.4 Temporal evolution of physical properties (mean values) in the growing penumbral region R. (a) TiO intensity. (b) FLow velocity. (c) Horizontal magnetic field strength. (d) Magnetic inclination angle. In (c) and (d), data are fit to a step function (see Equation (3.1)). The overplotted magenta curve represents the Fermi HXR 25–50 keV flux.

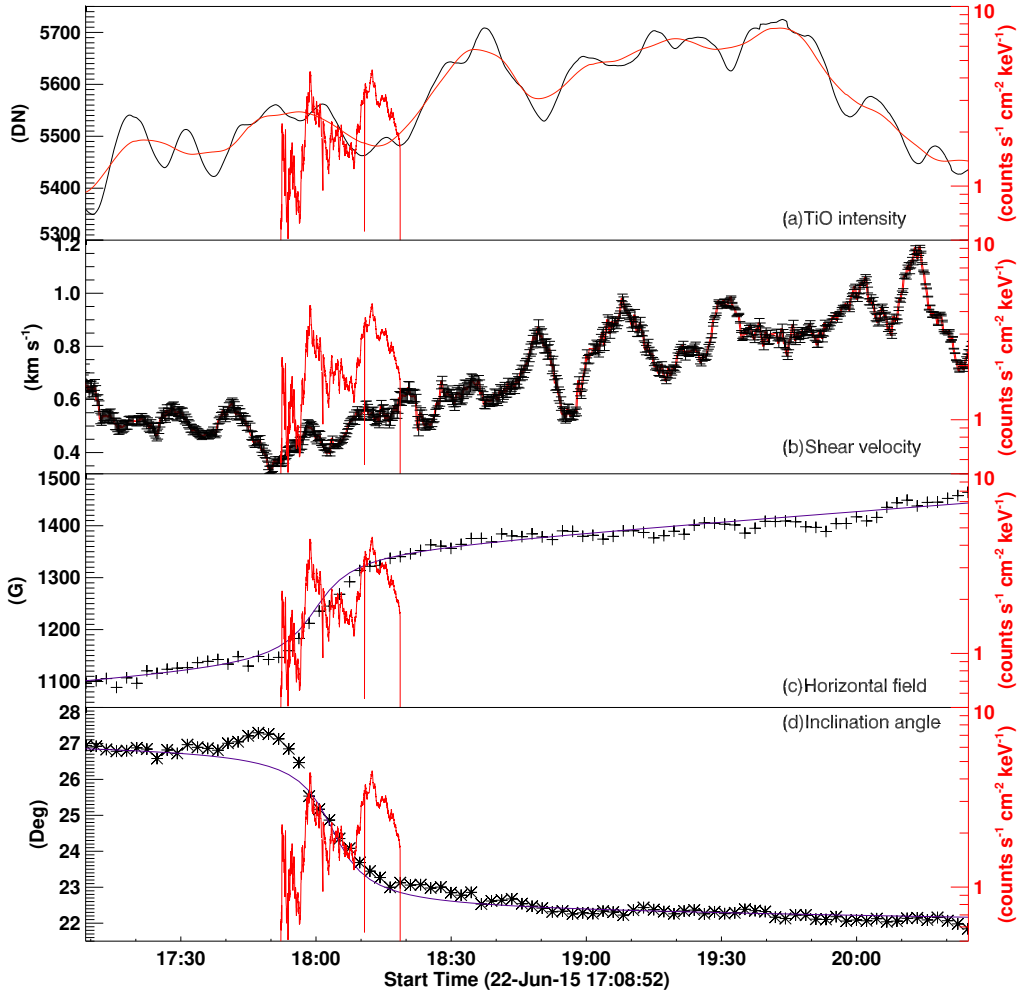

Figure 3.5 Temporal evolution of physical properties (mean values) in the shear flow region P (the elliptical region in Figure 3.2d). (a) TiO intensity. (b) Shear flow velocity. (c) Horizontal magnetic field strength. (d) Magnetic inclination angle. In (c) and (d), data are fit to a step function (see Equation (3.1)). The overplotted magenta curve represents the Fermi HXR 25–50 keV flux.

CHAPTER 4

EVOLUTION OF PHOTOSPHERIC VECTOR MAGNETIC FIELD ASSOCIATED WITH MOVING FLARE RIBBONS AS SEEN BY GST

4.1 Introduction

The reconfiguration of coronal magnetic field due to energy release is the focus of almost all models of flares/CMEs, which generally do not consider the restructuring of magnetic and flow fields in the dense photosphere partially due to the often assumed line-tying effect [163]. Nonetheless, observational evidences of rapid (in minutes), significant, and permanent photospheric structural changes apparently as a response to flare/CME occurrences have been accumulated over the past 25 years from both ground- and space-based instruments (see e.g., Wang & Liu [229] for a recent review). These include stepwise changes of line-of-sight (LOS) and vector magnetic fields (e.g., [224, 197, 228, 118, 200, 157, 117, 188, 199, 27]), morphological changes of sunspot penumbrae (e.g., [231, 120, 49, 256, 255]), changes of photospheric flow field (e.g., [202, 47, 237, 234]), and sunspot displacement and rotations ([7, 121, 237, 122, 17, 18, 255]). Although it is sometimes challenging to disentangle the cause-and-effect relationship between flare/CME processes and photospheric structural changes, studying this topic can shed new insights into the photosphere-corona coupling under the context of energy and momentum transportation in the flare-related phenomena, and help advance and constrain flare/CME models.

The aforementioned various aspects of photospheric evolution closely associated with flares/CMEs were largely studied separately. It might be possible that they can be accommodated by the back reaction of coronal restructuring on the photosphere and interior [89]. In this scenario, the coronal magnetic field would contract inward due to magnetic energy release [88], and the central photospheric field vectors may be

loosely expected to tilt toward the surface (i.e., becoming more horizontal) as a result of this contraction. Such a magnetic field change would correspond to a Lorentz-force change that is exerted at and below the photosphere [89, 61, 158]. Furthermore, the inward collapse of coronal field might also be accompanied by an upward turning of fields in the peripheral regions [120]. These are well in line with observations of flare-induced contraction of coronal loops (e.g., [128, 126, 127, 125, 73, 181, 235]), and with photospheric observations that flaring sites usually exhibit an enhancement of horizontal magnetic field B_h and penumbral structure at the center, surrounded by regions of weakened B_h and penumbrae; also, the resulting Lorentz-force change seems to be able to drive the observed surface flows and sunspot motions (see references above). It should be noted that although the overall magnetic field in three dimension (3D) must become more potential after the release of magnetic energy, the near-surface field could become more stressed after flares/CMEs (e.g., [99, 118]).

It is worth noting that due to resolution limitation imposed by data, a majority of previous studies rely on the comparative analysis of pre- and postflare structures. Meanwhile, this approach avoids the concern that heating from flare emissions change spectral line profiles, leading to *transient* anomaly in the magnetic field measurement (e.g., [156, 268, 162, 132, 199]). For flare-related *permanent* magnetic field changes, the most prominent one could be the irreversible strengthening of B_h in regions around central flaring PILs and between double flare ribbons. This has been corroborated by results from not only observations but also MHD modeling (e.g., [112, 92, 93]). However, there are only rare reports about permanent changes of photospheric magnetic and flow field in association with the spatial and temporal evolution of flare emissions, specifically, flare ribbons. Using LOS magnetograms from the Global Oscillation Network Group, Sudol & Harvey [197] pointed out in several events that the step-like LOS field change appears to propagate at a speed similar to those of ribbons. A propagating motion of B_h enhancement across the flaring region in a

major flare event was also noticed by Sun et al. [199] using vector magnetic field data from the HMI on board the SDO. Importantly, higher resolution data at both the chromospheric and photospheric levels are needed to fully exploit the association between flare ribbon motions and magnetic/flow field changes, which could provide major clues to the origin of flare-related restructuring on the surface.

Recently, based on chromospheric Hα and photospheric TiO images at unprecedented resolution obtained with the 1.6 m GST [72, 24, 70, 216] at Big Bear Solar Observatory (BBSO), Liu et al. [122] discovered that a sunspot experiences a differential rotation, where the moving front corresponds to a flare ribbon that moves across the sunspot during the 2015 June 22 M6.5 flare event (SOL2015-06-22T18:23) in NOAA active region (AR) 12371. This finding implies that the surface rotation is directly linked to the magnetic reconnection process in the corona [10]. Naturally, this revives the question of whether the photospheric magnetic field would change permanently as ribbons sweep by. Motivated by our observation, Wheatland et al. [242] presented a theoretical model in which this kind of flare-ribbon-related photospheric change results from a downward propagating shear Alfvén wave from the coronal reconnection region. Another natural question is whether the velocity u of ribbon propagation would be affected concurrently by the possible field change, since under a simplified two-dimensional magnetic reconnection model, u is correlated with the vertical field B_z on the surface as $u = E/B_z$, where E is the electric field strength in the reconnecting current sheet [21].

Several other works have also studied this 2015 June 22 M6.5 flare from various perspectives. Mainly using data from BBSO/GST's VIS and NIRIS, Wang et al. [230] reported small preflare brightenings near magnetic channels that may be precursors to the event onset. With nonlinear force-free field (NLFFF) modeling, Awasthi et al. [11] revealed that the initial magnetic reconnection may occur within a multiple flux rope system. Jing et al. [97] observed a propagating brightening in the flare

decay phase, which may be linked to a slipping-type reconnection. More relevant to the present study, Wang et al. [234] analyzed GST TiO and HMI observations and found flare-related enhanced penumbral and shear flows as well as B_h around the PIL, which could be attributed to the coronal back reaction. Using HMI observations and NLFFF models, Bi et al. [18] presented that the main sunspots on either side of the PIL rotate clockwise during the flaring period, when coronal fields are found to contract significantly. In addition, with NIRIS data Deng et al. [48] studied magnetic field property and flare-related evolution of umbral fine structures, and Xu et al. [254] showed a transient rotation of surface field vectors seemingly associated with one flare ribbon. Related discussions will be given below.

In this work, we further investigate the 2015 June 22 M6.5 flare event by comparatively studying high spatiotemporal resolution VIS chromospheric Hα off-band images and NIRIS photospheric near-infrared vector magnetograms from BBSO/GST. These state-of-the-art observations are essential for achieving our goal of scrutinizing the intimate relationship between the motion of flare ribbons and possible *permanent* changes of the local vector field, which was not studied before. Special attention is paid to B_h, which is the component exhibiting the most clear flare-related changes (e.g., [228, 229, 61]). Concerning the aforementioned flare-produced transient magnetic anomaly, we note that the contamination of NIRIS polarimetry from flare emissions was claimed not to be present in this event, as no significant changes are detected in NIRIS intensity profiles ([254], also see the Appendix and Figure A.2). Moreover, we mainly concern ourselves with permanent magnetic field changes associated with the flare. For the purposes of data validation and results corroboration, HMI vector magnetograms are analyzed as well. In order to examine the evolution of 3D magnetic field above the flaring AR, we also build a time sequence of NLFFF extrapolation models based on HMI data. The plan of this chapter is as follows. In Section 4.2, we first introduce observations and data processing procedures.

In Section 4.3, we describe results derived from analyses of observations and magnetic field models, and remark on their implications. In Section 4.4, we summarize major findings and discuss the results.

4.2 Observations and Data Processing

BBSO/GST employs a combination of a high-order adaptive optics system with 308 subapertures [180] and the post-facto speckle-masking image reconstruction technique [251]. During ∼16:50–23:00 UT on 2015 June 22, GST makes observations of the then near-disk-center (8°W, 12°N) NOAA AR 12371 and achieves diffraction-limited resolution under an excellent seeing condition, fully covering the M6.5 flare. The data taken include images in TiO (705.7 nm; 10 Å bandpass) by the Broad-band Filter Imager with a field of view (FOV) of 70″ at 0.1″ resolution and 15 s cadence, Fabry-Pérot spectroscopic observations around the Hα line center at ±1.0, ±0.6, and 0.0 Å (0.07 Å bandpass) by VIS with a 70″ circular FOV at 0.1″ resolution and 28 s cadence, and spectropolarimetric observations of the Fe I 1564.8 nm line (0.1 Å bandpass) by NIRIS with a 85″ round FOV at 0.24″ resolution and 87 s cadence (for a full set of Stokes measurement). Bursts of 100 and 25 frames are processed for speckle reconstruction at TiO and each Hα line position, respectively. In this study, we aligned Hα + 1.0 Å images with sub-pixel precision and used these Hα far red-wing images to best trace the evolution of flare ribbon fronts (e.g., [52]).

It is notable that this M6.5 flare is one of the first major flare events observed by NIRIS, which is dedicated to the 1564.8 nm doublet band observation. This spectral line is the most Zeeman sensitive probe (with the maximum splitting factor Landé $g = 3$) of the magnetic field within a small height range at the atmospheric minimum opacity, the deepest photosphere [187], and is the best spectral line for umbral magnetic field observations in the entire electromagnetic spectrum [78, 129]. Although it has a lower diffraction limit than some visible lines and the issue of thermal noise

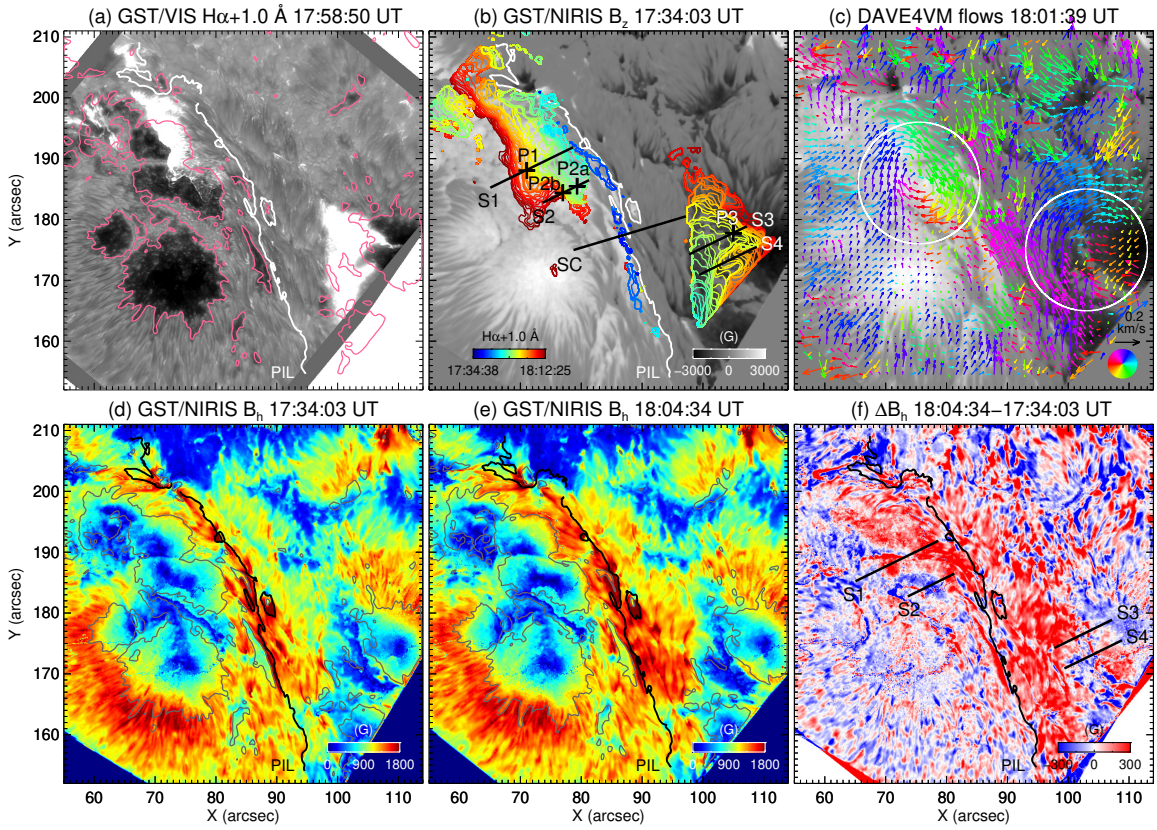

Figure 4.1 Evolution of flare ribbons and magnetic fields. (a) Hα + 1.0 Å image near the flare peak showing the two major flare ribbons. The magenta lines contour B_z map (smoothed by a window of $0.7'' \times 0.7''$) at $\pm$1600 G. (b) B_z image superimposed with curves (color-coded by time) that depict the progression of flare ribbon fronts. Note that the western ribbon and its evolution are not entirely captured due to the limited FOV of GST. The overplotted lines S1–S4 and SC indicate the slit positions of the time slices and vertical cross sections shown in Figures 4.2 and 4.5, respectively; the magnetic field evolution in several sample positions (P1, P2a, P2b, and P3) is plotted in Figure 4.3. (c) B_z image superimposed with arrows (color-coded by direction; see the color wheel) that illustrate DAVE4VM flows averaged between 17:52:56–18:13:17 UT (sunspot rotation phase; Liu [122]) subtracted by the flow field averaged between 17:32:35–17:51:29 UT. The two white circles mark the regions of rotational motion. A window size of 23 pixels was set for DAVE4VM tracking. (d)–(f) Maps of B_h in the pre- and postflare states and their difference. The PIL is overplotted in (a)–(b) and (d)–(f). All the images in this study are aligned with respect to 17:34:03 UT.

has to be mitigated, the 1564.8 nm line has lower scattered light, produces more stable images under the circumstances of atmospheric turbulence, and only exhibits emissions in some extremely energetic flares. Equipped with two Fabry-Pérot etalons in a dual-beam optical design, NIRIS captures two simultaneous polarization states and images them side-by-side onto half of a closed-cycle, helium-cooled 2048 $\times$ 2048 HgCdTe infrared array. Significant efforts have been devoted to develop the NIRIS data processing pipeline at BBSO [3, 2], which essentially includes dark and flat field correction, image alignment and destretching for dual beams (with 60 wavelength sampling), calibration of instrumental crosstalk (by measuring the detector response to pure states of polarization passing through the telescope optics), and Stokes inversion using the Milne-Eddington (M-E) atmospheric approximation (with initial parameters pre-calculated to resemble the observed Stokes profiles). For a proper exploration of NIRIS vector field measurement, we further resolved the 180° azimuthal ambiguity using the ME0 code originally developed for Hinode vector data [108, 109] that is based on the "minimum energy" algorithm [136, 137], removed the projection effect by transforming the observed vector fields to heliographic coordinates [67], and conducted a validation of data processing by comparing to HMI data products (see the Appendix and Figure A.1). The NIRIS vector magnetograms deduced from the above procedures were used in our previous study of this event [230]. Note that following the convention of Hinode, the disambiguated azimuth angle in this chapter ranges counterclockwise from $-180°$ to 180°, with the direction of zero azimuthal angle pointed to the solar west. In order to minimize the seeing effect (spatially varying image motion) in the ground-based observations, in this work we also performed image destretching to intensity images from the inversion, and then applied the determined destretch to the time sequence of NIRIS vector magnetograms. NIRIS intensity images were also used to accurately co-align NIRIS vector field observations with Hα far red-wing images through matching sunspot and plage areas.

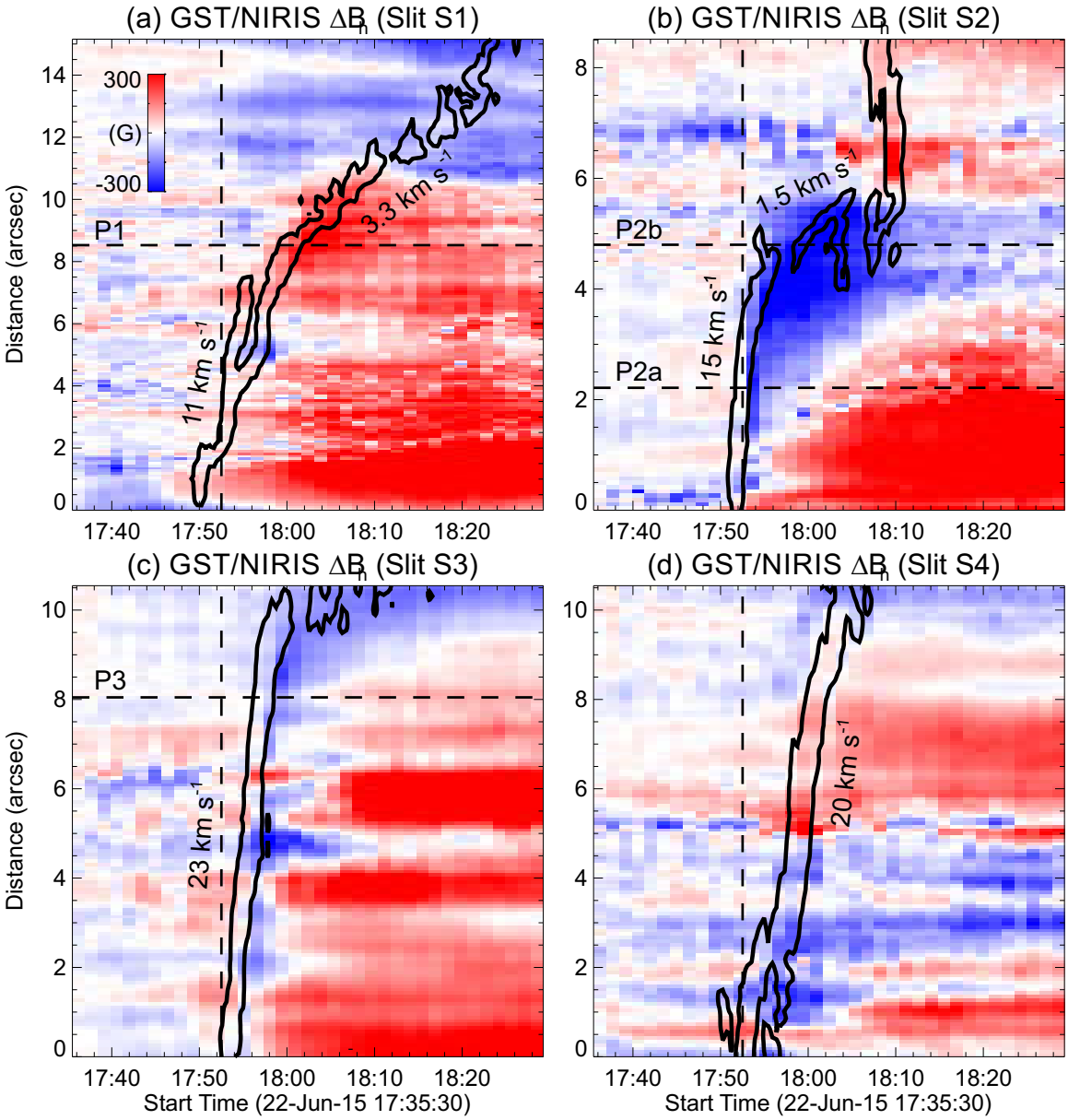

Figure 4.2 Correlation between flare ribbon motion and B_h change. The background portrays time slices for the slits S1–S4 (as denoted in Figure 4.1(b)) using the fixed difference images (relative to the preflare time at 17:34:03 UT) of B_h, showing the B_h change. The superimposed black lines are contours (at 600 DN) of time slices for the slits S1–S4 (smoothed by a window of $0.23'' \times 0.23''$) using the running difference Hα + 1.0 Å images, showing the motion of ribbon front. The estimated ribbon velocities along each slit are denoted. In particular, along the slit S2, the speed of the ribbon front is $\sim$15 km s^{-1} during 17:52–17:55 UT and $\sim$1.5 km s^{-1} during 17:55–18:06 UT, as denoted in (b). For all the slits, the distance is measured from the end closest to the PIL. The horizontal dashed lines mark the positions of P1, P2a, P2b, and P3 relative to their corresponding slits. The vertical dashed line indicates the time of the first main HXR peak at 17:52:31 UT.

The SDO/HMI observations used to accompany the NIRIS data analysis are full-disk vector magnetograms at 1″ resolution and 135 s cadence [199]. The HMI instrument takes filtergrams of Stokes parameters at six wavelength positions around the Fe I 617.3 nm spectral line. The Stokes inversion technique implemented to routinely analyze HMI pipeline data is also based on the M-E approximation [19], and a variant of the ME0 code is used for azimuthal disambiguation [83]. The retrieved HMI data were processed (mainly for combining disambiguation results with azimuth, and deprojection) using standard procedures in the Solar SoftWare (SSW) provided by the HMI team, and were expanded in size to match and align with NIRIS. For NLFFF extrapolations, we remapped HMI magnetograms of the entire AR at original resolution using Lambert (cylindrical equal area) projection centered on the middle point of the AR. After adjusting the photospheric boundary with a preprocessing procedure to better suit the force-free condition [246], we constructed a time sequence of NLFFF models using the "weighted optimization" method [243, 244] optimized for HMI data [245, 248]. The calculation was made using 2 × 2 rebinned magnetograms within a box of 472 × 224 × 224 uniform grid points (corresponding to about 348 × 165 × 165 Mm^3). In addition, soft- and hard X-ray (HXR) emissions of the 2015 June 22 M6.5 flare were recorded by the *Geostationary Operational Environmental Satellite* (GOES)-15 and *Fermi Gamma-Ray Burst Monitor* [135], respectively. In GOES 1.6–12.4 keV energy flux, the flare of interest starts at 17:39 UT, peaks at 18:23 UT, and ended at 18:51 UT, with the first main peak in Fermi 25–50 keV HXR flux at 17:52:31 UT [122].

4.3 Analyses and Results

Figure 4.1 presents an overview of the evolution of chromospheric ribbons and photospheric field in the 2015 June 22 M6.5 flare. Here the FOV of BBSO/GST covers the central core region of the flare. From images of VIS Hα + 1.0 Å and NIRIS B_z, it

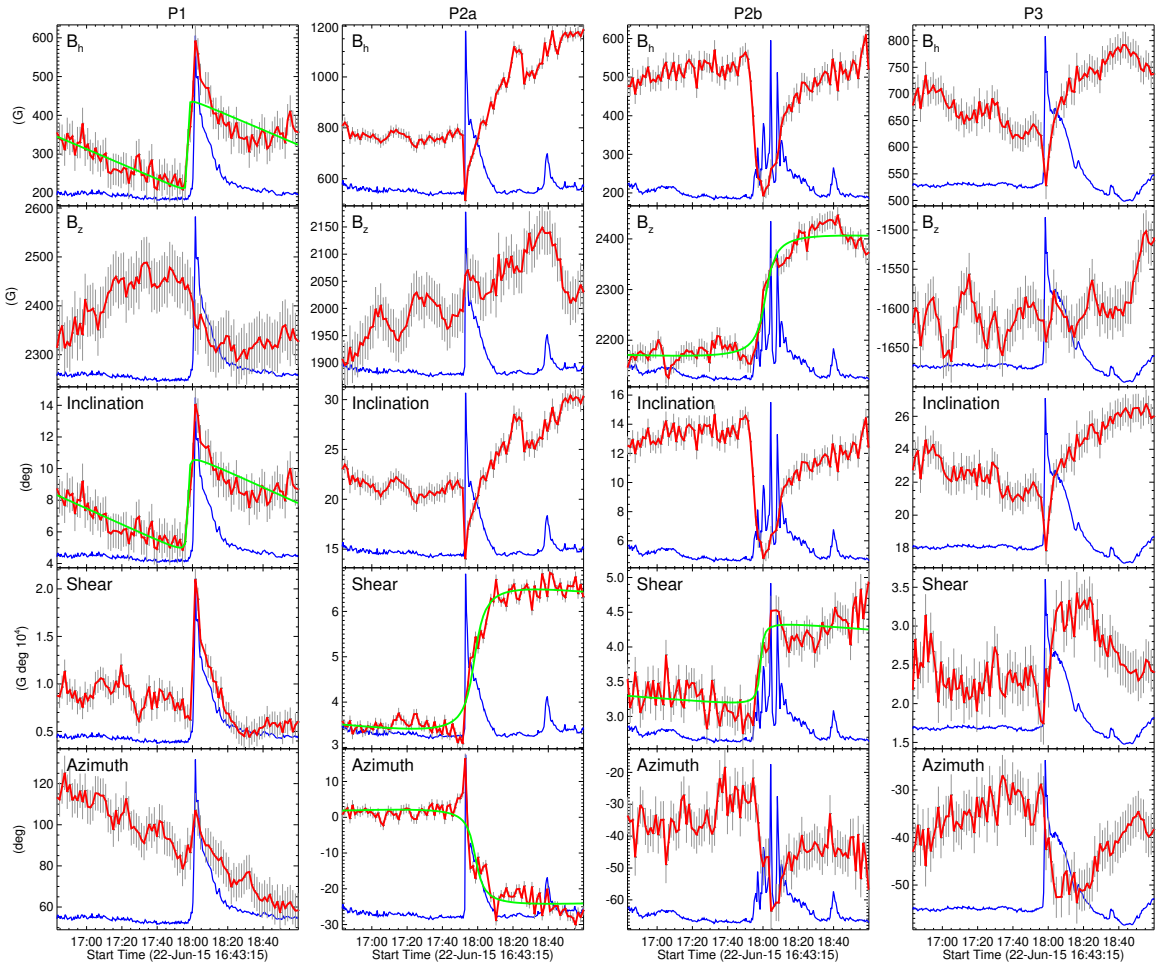

Figure 4.3 Time profiles of flare Hα + 1.0 Å emission and changes of photospheric magnetic field at sample positions P1, P2a, P2b, and P3 (as marked in Figure 4.1(b)). The Hα light curves are plotted in blue and in an arbitrary unit. The quantities plotted in red are, from top to bottom rows, B_h, B_z, inclination angle, magnetic shear, and azimuth angle. In each panel, the grey error bars indicate a 1σ level of the fluctuation of corresponding magnetic field parameter in the preflare time (from 16:43:15 to 17:38:24 UT). When appropriate, the field evolution is fitted using a step function (green lines).

can be clearly seen that (1) two main flare ribbons move away from the PIL and sweep through two sunspot regions of opposite polarities (also see Figure 4.1(a) and (b)), and (2) both sunspots undergo a clockwise rotation during the flare period, which is unambiguously demonstrated with flow tracking using the differential affine velocity estimator for vector magnetograms (DAVE4VM; [174]) method (see Figure 4.1(c)). This is consistent with previous studies using TiO and HMI observations [122, 18]. Interestingly, the southern part of the eastern ribbon apparently slows down when approaching the center of the eastern rotating sunspot (cf. Figure 4.1(b) and (c)). A similar but less obvious slowdown is discernible for the central part of the western ribbon. A comparison between pre- and postflare images (see Figure 4.1(d) and (e)) shows that there is a pronounced enhancement of B_h in an extended region mainly along the PIL (red-colored region in Figure 4.1(f)). To better disclose the B_h evolution, we make fixed difference B_h images relative to a preflare time. It is remarkable to notice that the enhancement of B_h not only shows up around the PIL [234], but also moves away from the PIL and spreads across the flaring region, mimicking the flare ribbon motion. More intriguingly, a negative δB_h front, meaning a transient weakening of B_h, appears to precede the moving B_h enhancement, especially at the southern portion of the eastern ribbon and the entire western ribbon.

To accurately characterize the B_h evolution associated with the flare ribbon motion, time-distance maps along slits S1–S4 (drawn in Figure 4.1(b)) based on the fixed difference B_h images are presented as the backgrounds of Figure 4.2. They are overplotted with contours of the same time-distance maps but based on the running difference Hα + 1.0 Å images that highlight the ribbon fronts. We constructed these slits by orientating elongated windows (with various length but a common short side of $0.78''$) approximately perpendicular to the observed ribbon motion at 26° counterclockwise from the solar west, and averaged the pixels across the short sides. The distance shown is measured from the ends of slits closest to the PIL. In

Figure 4.3, the temporal evolution of Hα + 1.0 Å emission (blue) is compared with that of vector magnetic field (red; in terms of B_h, B_z, inclination angle relative to the vertical direction, magnetic shear, and azimuth angle) at several representative positions P1, P2a, P2b, and P3 along the slits (as marked in Figure 4.1(b); values averaged over 7×7 pixels^2 centered on them). Here the magnetic shear for evaluating the nonpotentiality is computed as $B \cdot \theta$ [227, 233], where $B = |\boldsymbol{B}|$ and $\theta = \cos^{-1}(\boldsymbol{B} \cdot \boldsymbol{B}_p)/(B\,B_p)$, with the subscript p representing the potential field, which we derived using the fast-Fourier transform method [4]. When appropriate, we also fit these time profiles of magnetic properties with a step function (green lines; [197]). Based on these results, we observe the following.

Along the slit S1, there exists a close spatial and temporal correlation between the motion of the eastern flare ribbon and the enhancement of B_h (Figure 4.2(a)), especially after the time of the first main HXR peak (vertical dashed line). At P1 (see Figure 4.3, first column), with the arrival of ribbon front the photospheric field turns more inclined relative to the surface, with B_h and inclination angle increased stepwise by 244±24 G and 6.4±0.6° in ∼0.5 and 1.5 minutes, respectively; also, magnetic shear sharply increases by ∼250% but then returns to the preflare level in about 20 minutes. In contrast, B_z evolved more gradually without an abrupt change. In the meantime, a transient increase of azimuth angle meaning a temporary counterclockwise rotation of field vectors can be noticed [254].

Along the slit S2 across the center of the eastern rotating sunspot, the propagation of the eastern flare ribbon exhibits a prominent deceleration, and the arrival of the ribbon front is coincident with a transient decrease of B_h followed by an increase (see Figure 4.2(b)). At P2a (see Figure 4.3, second column), B_h and inclination angle temporarily decrease by ∼300 G and ∼8° and then increases by ∼600 G and ∼13° in ∼30 minutes, respectively; meanwhile, magnetic shear shows a step-like increase by ∼86% in ∼15 minutes. After a transient increase like at P1,

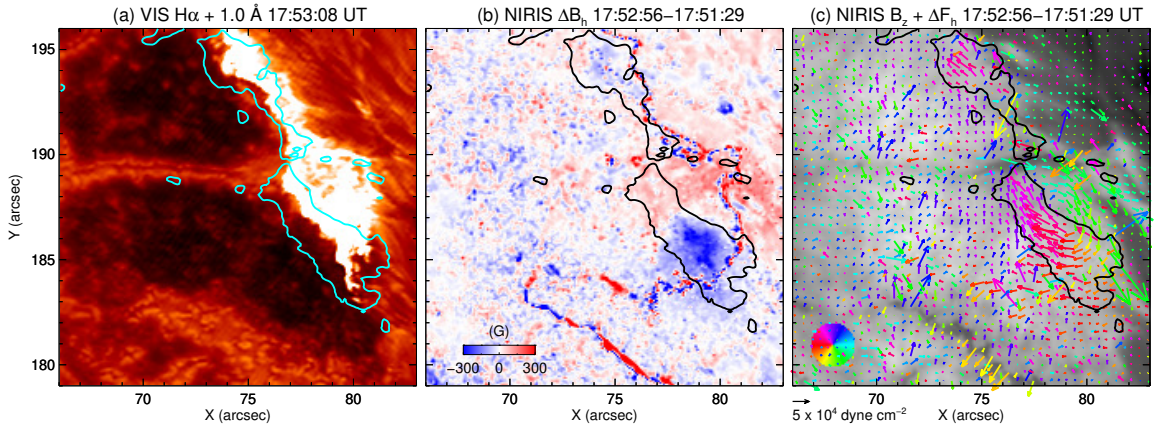

Figure 4.4 Flare ribbon and induced Lorentz-force change. (a) Hα + 1.0 Å image at 17:53:08 UT near the first main HXR peak, overplotted with contours (smoothed by a window of $0.55'' \times 0.55''$) at 600 DN (same level as that used in Figure 4.2) based on the running difference Hα + 1.0 Å image (i.e., 17:53:08 minus 17:52:40 UT) that highlight the ribbon front. (b) Running difference image of B_h at about the same time. (c) The corresponding B_z image (scaled from −1000 to 3000 G) overplotted with arrows (color-coded by direction; see the color wheel) representing δF_h vectors. The contours in (b) and (c) are the same as those plotted in (a).

azimuth angle begins to decrease, connoting the observed clockwise sunspot rotation [122] that drags the magnetic field with it. Compared to P2a, the magnetic field evolution at P2b (around the rotation center) bears a resemblance but displays a more prolonged decrease of B_h and inclination angle; remarkably, B_z at P2b undergoes a permanent increase of 266±20 G in ∼13 minutes around 18 UT (see Figure 4.3, third column), when the speed of the flare ribbon has evidently reduced (Figure 4.2(b)). Since darker umbrae evince stronger vertical fields [131], the irreversible increase of B_z of this rotating sunspot is also evidenced by a ∼7% decrease of its overall intensity in TiO and 1564.8 nm after the flare [122, 48]. A line profile analysis further corroborates that the transient decrease of B_h (and also increase of B_z) at P2b is irrelevant to magnetic anomaly due to flare heating (see the Appendix and Figure A.2). Assuming a uniform reconnecting electric field along the entire eastern ribbon, the observed slowdown of flare ribbon motion with concurrent increase of B_z at a portion of the

ribbon could be expected [21]. From about 18:08 UT, the northern section of the ribbon curves southward and overtakes the motion of the ribbon along S2.

In Figure 4.4, we further compare the locations of the eastern flare ribbon front, δB_h, and the horizontal Lorentz-force change $\delta \mathbf{F}_{\rm h} = \frac{1}{4\pi} \int dA \delta(B_{\rm r}\mathbf{B}_{\rm h})$ [61], at a time close to the first main HXR peak. Note that the newly brightened ribbon region (e.g., the ribbon front) is cospatial with the region of decreased B_h. This, together with the increased B_h at the region just swept by the ribbon, yields a vortex pattern in the $\delta \mathbf{F}_{\rm h}$ map. Obviously, the torque provided by this $\delta \mathbf{F}_{\rm h}$ vortex has the same direction (i.e., clockwise) as the observed sunspot rotation. This implies that the B_h decrease preceding its increase may create a moving horizontal Lorentz-force change to drive the differential sunspot rotation as observed [122].

Along the slit S3, the motion of the western ribbon is correlated with magnetic field changes in a way similar to those found along the slit S2, e.g., showing a transient decrease followed by an increase of B_h and inclination angle (see Figure 4.2(c) and light curves of P3 in the fourth column of Figure 4.3). A ribbon deceleration together with a prolonged decrease of B_h also seems to be present along the slit S4 across the center of the western rotating sunspot (see Figure 4.2(d)). It is worthwhile to mention that despite of a lower resolution, vector magnetograms from HMI show very similar magnetic field changes related to flare ribbon motions as described above (see the Appendix and Figure A.3), which substantiates the NIRIS results.

Finally, we investigate the flare-related coronal field evolution in terms of the distribution of horizontal component of the total electric current density $|J_h| = (J_x^2 + J_y^2)^{1/2}$ in several vertical slices to the extrapolated 3D coronal magnetic field. These slices intersect with the surface at locations of the same slits S1 and S3 as above through the regions of flare ribbons and another slit SC perpendicularly across the central PIL (as denoted in Figure 4.1(b)). Plotted in the top and bottom rows of Figure 4.5 are the distributions of J_h for the pre- and postflare states, respectively, in

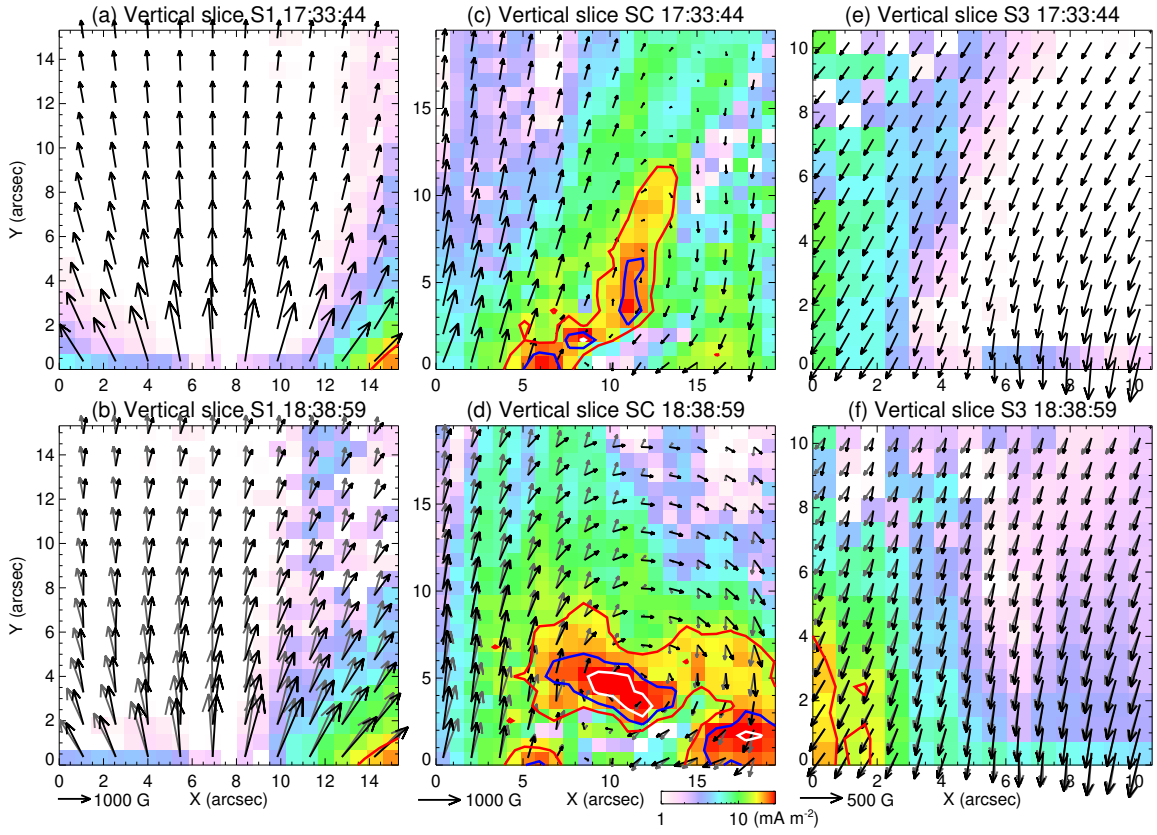

Figure 4.5 Distributions of magnetic field and current in the preflare (a, c, e) and postflare (b, d, f) states in vertical cross sections S1, SC, and S3, the bottom sides of which are slits S1, SC, and S3, respectively, as denoted in Figure 4.1(b). The distance on the surface is measured from east to west for all slices. The background shows J_h in logarithmic scale, overplotted with black arrows representing the transverse field vectors in the vertical slices. The preflare field vectors are also shown in gray in the corresponding postflare maps. The red, blue, and white contours are at levels of 0.015, 0.023, and 0.031 A m^{-2}, respectively.

these vertical slices, which are superimposed with arrows representing the transverse magnetic field vectors. From the results spanning the flaring period, it transpires that a downward collapse of coronal field occurs intimately associated with the flare (e.g., [200, 118, 117]). This is visualized by the dramatic change of the coronal currents above the PIL, from a vertically elongated source reaching 12″ to a substantially enhanced, horizontally elongated source concentrated close to the surface below 9″ (cf. Figure 4.5(c) and (d)). We further show that the collapse is also manifested by the clockwise (counterclockwise) turning of magnetic field vectors in the east (west) side of the PIL (except that the near-surface region in S3 has a clockwise turning), which leads to a more horizontal (i.e., inclined) configuration of magnetic fields at and above regions of the PIL and flare ribbons, conforming to the observed surface B_h enhancement therein. We note that (1) field vectors in the far east portion of S1 (and also the upper portion of S3) become more vertical after the flare. This reflects the fact that in the outer flaring region, B_h is observed to decrease (see Figures 4.1(f) and 4.2(a)) together with weakened penumbral features (not shown), which may be coherent with the collapse of the central fields (e.g., Liu et al.[120]). (2) Although not well demonstrated by the present extrapolations, it is plausible to expect that a time sequence of coronal field models with higher spatial and temporal resolution might show the successive turning of field vectors with the motion of flare ribbons.

4.4 Summary and Discussion

In this study, we take advantage of BBSO/GST high-resolution observations of both chromospheric ribbons in VIS off-band Hα and NIRIS photospheric vector magnetic fields in near infrared during the 2015 June 22 M6.5 flare to carry out a detailed investigation of photospheric vector magnetic field changes with related to flare ribbon motions, which were not studied before. This large and complex event shows not only the separation of flare ribbons but also the flare-related rotations of sunspots. We

analyzed the permanent surface magnetic field changes in the flare ribbon regions with a focus on B_h, using time-distance maps and temporal evolution plots. We also explored the 3D coronal restructuring with aid from the NLFFF modeling based on SDO/HMI vector magnetograms. Major findings are summarized as follows.

1. In the photosphere, B_h increases with the flare occurrence and this enhancement propagates away from the central PIL across the flaring region, exhibiting a close spatial and temporal correlation with the flare ribbon motion especially after the first main HXR peak (Figure 4.2). As seen in several representative positions (Figure 4.3), the strengthening of B_h (by $\sim$300 G) at the arrival of the flare ribbon front is accompanied by an increase of inclination angle (by $\sim6^\circ$), indicating that magnetic field becomes more inclined to the surface; also, the nonpotentiality as represented by magnetic shear generally enhances.
2. At the locations where azimuth angle sharply decreases indicating the sudden sunspot rotation, B_h and inclination angle decrease transiently before being enhanced. Particularly, the flare ribbon decelerates toward the sunspot rotation center where B_z becomes greatly intensified (Figures 4.2 and 4.3).
3. In the corona, a downward collapse of coronal magnetic field by $\sim3''$ toward the photosphere is clearly portrayed by the evolution of the vertical profiles of J_h around the PIL [200, 118, 117], which changes from a vertically elongated source to an enhanced, horizontally elongated source close to the surface (Figure 4.5). Correspondingly, above the PIL and flare ribbon regions, magnetic field becomes more inclined, which is consistent with the observed enhancement of B_h. We surmise that a successive turning of field vectors associated with the flare ribbon motion might be visualized given coronal field models with a sufficiently high resolution.

The increase of B_h at flaring PILs between flare ribbons has been known from the previous observations (e.g., [200, 118, 238]). The distinctive finding made in this investigation is that B_h enhances not only at the PIL region, but at the locations of the flare ribbon fronts. As the flare ribbons move away from the PIL, such enhancements also propagate successively with the ribbons. This discovery of the flare-ribbon-related photospheric field changes could be made owing to the high resolution of NIRIS observations, and is also substantiated by the HMI data. Since it has been well established that flare ribbon fronts are the footpoints of the newly reconnected field lines in the corona, the vector field changes spatiotemporally correlated with the

ribbon fronts must be a nearly instantaneous response of photospheric fields to the coronal restructuring, specifically, the reconnection of individual flux bundles.

We also want to point out that the correlation between the eastern flare ribbon and its related vector field change is complicated by the fact that ahead of the eastern ribbon, there is another elongated small brightening that propagates from north to south, along a line of high values of the squashing factor Q (Titov et al.[207]; see the Appendix and Figure A.4(a)). The high-Q lines correspond to the footprints of quasi-separatrix layers [46, 45], which are known to be favorable positions of flare ribbons. This brightening joins with the main eastern ribbon in the north (out of the FOV of GST) to form a continuous ribbon structure. To check whether this extra flare ribbon introduces magnetic field changes, we place a slit S5 perpendicular to the northern portion of the eastern ribbon (Figure A.4(a)) and repeat the analysis as done in Figure 4.2. Both the results using NIRIS and HMI data evince that the enhancement of B_h not only appears to follow the movement of the main eastern ribbon, but also occurs ahead of it, distending to the region of the extra ribbon (see Figure A.4(b) and (c)). We consider this as an additional piece of evidence that the photospheric vector magnetic field may respond nearly instantaneously to the coronal reconnection.

There are a few models that may help understanding the present observations. The series of force-free field models give only snapshots of equilibrium states rather than dynamic evolution; nevertheless, the disclosed redistribution of electric current system may reflect a coronal field restructuring following magnetic energy release in the corona (e.g., [88]). A back reaction of such coronal magnetic reconfigurations on the photosphere and interior may be expected [89], but it only loosely points to a more horizontal photospheric field, i.e., an increase of B_h; further, it does not necessarily explain why the magnetic shear should also increase. The shear Alfvén wave model [242] can explain both the increase of B_h and magnetic shear, in which the

shear Alfvén waves launched from the coronal reconnection region travel downward to impact the flare ribbon regions. In 3D, these waves correspond to the torsional Alfvén waves so that the rotation of plasma and magnetic field at the ribbon location is also expected. In addition, we have presented an idea that the B_h decrease preceding its increase may create a moving horizontal Lorentz-force change (Figure 4.4) to drive the differential sunspot rotation as observed [122]. It remains puzzling why B_h decreases at the region of the newly brightened ribbon.

Our main intention of this study is to present the details of the new phenomenon of the flare-ribbon-related photospheric magnetic field changes. It remains to see whether these vector field changes as found in this event are a generic feature of all flares or simply a peculiarity of this event. Certainly, more simultaneous high-resolution observations of chromospheric flare ribbons and photospheric vector magnetic fields throughout the flaring period are much desirable to further elucidate the photosphere-corona coupling in the flare-related phenomena.

CHAPTER 5

HIGH-RESOLUTION OBSERVATIONS OF SMALL-SCALE FLUX EMERGENCE BY GST

5.1 Introduction

Flux emergence, through which magnetic fields are transported to the solar atmosphere from sub-surface, is considered to be generated by convective motions and aided by magnetic buoyancy in solar interior [170, 171]. Flux emergence on different scales is important for energy release in different forms, inlcuding the small-scale brightenings and large-scale solar eruptions. The typical scenario of emergence is that magnetic fields being twisted underneath the photosphere due to flows and rise to form an Ω-loop due to magnetic buoyancy [155, 56]. Observations of emissions in the solar atmosphere such as in UV/EUV provide evidence that energy may be released due to reconnection during the process of emergence. The magnetic fields emerging through convection zone are not constrained to rise in an aligned orientation with the pre-existing field, so the magnetic reconnection is expected to occur between the emerging fluxes and pre-existing fluxes. Overall, on the large scale in the solar photosphere, the orientation of emerging fields is roughly aligned with the direction connecting paired polarity spots [149, 28].

Taking advantage of high-resolution ($\sim$0.3$''$) observations, De Pontieu [41] found that magnetic concentrations emerge within the granule interior and quickly ($\sim$10–15 minutes) disperse following granule flows. The author speculates such flux emergence initiates with horizontal magnetic structures. The study of Cheung et al. [35] supported these findings from the simulation perspective. They found that emerging magnetic elements with sufficiently high field strength can also impact on the granular structure. The elongated granule and intergranular lane darkening are

reported on the photosphere with observations in visible wavelengths [270, 114, 260]. On the other hand, the recent study of Campos Rozo et al. [22] showed that while small magnetic elements are advected to upper layers on the surface through normal convection, emergent magnetic fields with B$\geq$50 G tend to in turn induce the photospheric motions by governing the plasma flows. The authors also found that such emergent-flux-related flow fields change velocity distributions as well as granule elongation.

Besides the dynamic magnetic characteristics observed on the photosphere, variations of brightness from continuum images provide clear indications of magnetic flux emergence. Yurchyshyn et al. [263] found that small-scale flux emergences have associated bright points on the photosphere, mostly inside solar granulation, in which the field emerges at a size scale less than 1–2 Mm (e.g., [115, 41]). They suggested that the emergence of relatively strong fields create bright points at the footpoints of magnetic loops, which intrude into intergranular lanes. Ellerman bombs (EBs) [54], the bright signatures essentially observed in Hα wings, are found at locations where magnetic elements with opposite polarities are close to each other. They are likely linked with the dips of the serpentine magnetic field through the surface [152, 15]. The previous studies of EBs conclude that such photospheric heating processes are caused by photospheric reconnection of strong opposite-polarity field and are not directly associated with chromosphere and transition region dynamics (e.g., [240, 219, 218]).

Since the first observational report of granulation scale emergence events [41], high-resolution polarimetric observations focus more frequently on small-scale flux emergence events together with observations of flow motions. In the high-resolution ($\sim$0.32$''$) observation of small-scale flux emergence reported by Centeno et al. [30], by using analysis of local thermodynamic equilibrium (LTE) inversion of full Stokes measurements, the author found horizontal field emergence prior to the appearance of vertical flux elements in the typical granulation time scales (10 minutes). With the

advance of observational technology, the existence of flux loops have been witnessed (e.g., [130, 204]). By implementing magnetohydrodynamic (MHD) simulations of magnetoconvection, Moreno-Insertis et al. [144] detected two types of flux emergence events: magnetic loop emergence and flux sheet emergence. In previous observations of the flux loop emergence with Hinode (e.g,. [30, 130, 182]), the authors summarized physical characteristics of the emergence: the horizontal field enhances within a well-established granule structure followed by emerged vertical fields drifting in intergranular lanes. The vertical field elements are connected by horizontal magnetic patches. Recent studies by Centeno et al. [29] and Fischer et al. [60] have reported the flux-sheet emergence events, which have different signatures from flux loop emergence. Instead of evolving within granules, the horizontal field enhances together with the expansion of a granule. This forms an organized sheet-like mantle that spans both in the emerging direction and to sides. The sheet covers the entire granule, and the emerged longitudinal flux in footpoints is also in the order of 10^{18} Mx.

In this work, we study the magnetic field structure and evolution during the flux emergence in the NOAA active region (AR) 12665 on July 13, 2017. Taking advantage of the exceptionally high resolution of the 1.6 m off-axis Goode Solar Telescope (GST; [70]) at Big Bear Solar Observatory (BBSO), we are able to observe fine magnetic structures on sub-arcsecond level ($0.1''$ to $0.2''$) and study the magnetic properties in both flux emergence scenarios as described above. We also investigate photospheric and chromospheric brightness variation, especially Ellerman bombs, associated with the small-scale flux emergence. The structure of this chapter is as follows: We introduce our observations and data processing methods in Section 5.2; In Section 5.3, we present analyses of observational results; Key findings are summarized and discussions are presented in Section 5.4.

5.2 Observations and Data Processing

As the Sun enters the activity minimum, observations of ARs are less often obtained. On the other hand, with the routine operation of GST at BBSO, the quiet Sun and less complicated ARs are more feasible targets. Aided by the high-order adaptive optics system with 308 sub-apertures [180] and completion of the second generation of spectro-polarimetric instrument – the Near Infra-Red Imaging Spectro-polarimeter (NIRIS; [23]), BBSO/GST obtained observations near the main magnetic polarity inversion line (PIL) of NOAA AR 12665 (31°W, 6°S) during ∼20:16–22:42 UT on 2017 July 13. Under the excellent seeing conditions, the observations achieved diffraction-limited imaging with a resolution of 0.1″ to 0.2″. The data includes spectro-polarimetric observations of full sets of Stokes measurement at the Fe I 1564.8 nm line (0.25 Å bandpass) by NIRIS with a round field of view (FOV) of 80″ at 0.24″ resolution and 56 s cadence, Fabry-Pérot spectroscopic observations around Hα line center at ± 1.0, ± 0.6, ± 0.4, and 0.0 Å (0.08 Å bandpass) by the Visible Imaging Spectrometer (VIS) with a 70″ circular FOV at 0.1″ resolution and 33 s cadence, and images in TiO (705.7 nm; 10 Å bandpass) by the Broad-band Filter Imager with a 70″ circular FOV at 0.1″ resolution and 15 s cadence. TiO and Hα observations achieved a diffraction-limited resolution in the order of 0.1″ with speckle-masking image reconstruction [251], while NIRIS achieves a spatial resolution of 0.24″ without speckle reconstruction.

Alignment among Hα images, TiO images, and magnetograms are processed by matching the most stable sunspot and plage features in the FOV. After data noise deduction, the essential vector magnetograms from NIRIS are obtained through Stokes inversion based on Milne-Eddington approximation (see Methods in Wang et al. [230]) and aligned by using interpolation to achieve sub-pixel precision. Vector magnetograms in the local coordinates were deduced after removing the 180° azimuthal ambiguity with the AUTO-AMBIG code by Leka et al. [108, 109], which

is an optimized dis-ambiguation method originally intended for *Hinode* vector data. It uses the minimum energy algorithm [136] to find a minimum of field divergence ($\nabla \cdot$B) and current density (J) in the FOV. To assist in tracking magnetic elements and quantification of magnetic flux, we applied the Southwest Automatic Magnetic Identification Suite (SWAMIS) [44], which is a demonstrated technique for magnetic identification and tracking. Here we set the threshold of the vertical magnetic field to 100 G. Based on visual inspection, this threshold allows us to include as many detected magnetic elements as possible while maintaining a high S/N ratio.

5.3 Results and Analysis

GST observation was centered at the flare productive NOAA AR 12665 at (432″,-164″). The AR is classified as the $\beta\gamma$ magnetic configuration. Figure 5.1 shows an overview of the AR in magnetograms, TiO images, and Hα images at +1.0 and -0.4 Å. During the period of observation, there is obvious magnetic flux emergence of opposite polarities at the main PIL. Emerging magnetic elements actively diverge from the PILs and eventually merge into the nearby sunspots. The TiO visible images clearly show that granules near the PIL exhibit elongating patterns. Such evolving granular structures are typical photospheric signatures of flux emergence. Simultaneous magnetic field measurements taken by NIRIS reveal an enhanced horizontal field accompanied by the elongating granules. Concentrated magnetic elements of opposite polarities are located at the two ends of the central region with the enhanced horizontal field.

In Figure 5.1(b), the Hα image clearly exhibits brightenings at the footpoints of the emerging fibrils associated with the new flux emergence and growing pores. The green circles outline the locations of small-scale flux emergences labeled 1 to 9. The diameters of circles correspond to the size of the associated granules in TiO images. The white dashed boxes F1 and F2 indicate the regions of events that we will discuss

in Sections 5.3.1 and 5.3.2. The vertical component of magnetic fields is shown in Figure 5.1(a), which saturates at ±500 G. From the TiO continuum observation, one can see that the magnetic flux is transported to the photosphere through individual episodes in the scale of granules during flux emergence. Subsequently, the Sun's pore areas are expanded as the same polarity fluxes are merged to them. From Hα off-band images, flows in dark fibrils are observed streaming toward or away from the concentrated magnetic footpoints.

During the observation time window, we identified eight good events (see Table 5.1) of small-scale flux emergence that have high-quality data in all wavelengths obtained. The magnetic topology of event 5 can not be clearly interpreted because the magnetograms lack the accuracy of azimuthal disambiguation in this event area. For a similar reason, we exclude some emergence events seen in continuum images. Each of them has an emerged total unsigned flux in the order of 10^{18} Mx and shows prominent magnetic structure changes on the photosphere. The observed lifetime of these emergence events is ∼10 minutes, which is on the same scale as the lifetime of granulation. Thus the observed flux emergence events are considered as granular-sized magnetic flux emergence. Different magnetic characteristics are observed in these small-scale flux emergence events with high-resolution data. In the case studies of observed emergent events, we are able to distinguish two different types of flux emergence processes, i.e., flux sheet emergence and flux loop emergence (e.g., [130, 29, 60]). In the case studies of the observed emergent events, the two types of flux emergence events are categorized based on geometric properties of the field evolution and correspondent structure changes.

5.3.1 Detailed Study of a Flux Sheet Emergence

Since the observed emergence events are visible in granule-sized scale and often adjacent to actively evolving granules, the clear event episodes are selected manually

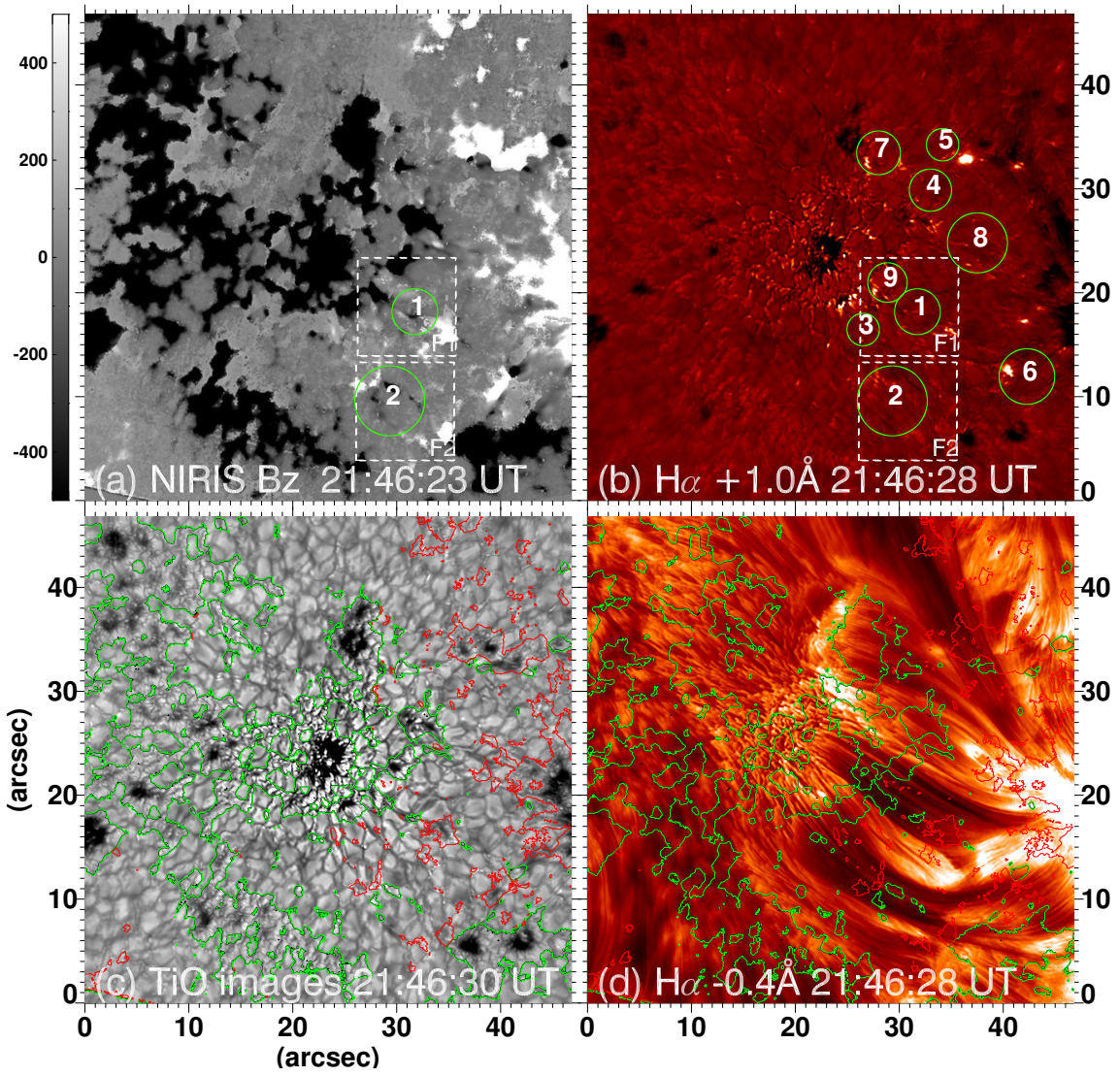

Figure 5.1 Overview of the emergence observations. Multi-wavelength observations from GST at 21:46 UT is displayed in the figure. Panel (a) shows vertical magnetic field map, whose magnitude is represented in gray scale with black (white) meaning negative (positive) polarity. Grayscale of the vertical field map saturates at ±500 G. Panel (b) and (d) show Hα images at +1.0 and −0.4 Å, respectively. Green circles indicate regions of observed emergence events and white dashed boxes (F1 and F2) indicate FOV of 5.2 and 5.5 Panel (c) is TiO image that shows photospheric structures. Panel (c) and (d) are overplotted with vertical field contours of ±150 G, in which green (red) indicate negative (positive) values.

after implementing the SWAMIS feature tracking method. In the five identified events of flux sheet emergence among all eight selected events, an enhanced horizontal field is seen to emerge within small granules as well as in the intergranular dark lane that

Table 5.1 Magnetic Properties of the Observed Events[a]

(1)	(2)	(3)	(4)	(5)	(6)	(7)	(8)
Event Number	Horizontal Field (G)	Vertical Field (G)	Vertical Flux (10^{18} Mx)	Maximum Distance ($''$)	Separation Speed ($km\ s^{-1}$)	Doppler Speed ($km\ s^{-1}$)	EBs occurrence (Y/N)
1⋆	390/280	250/250	4.4/2.0	4.4	1.6	0.45	N
2◇	180/148	500/298	1.0/1.2	7	1.3	0.98	Y
3⋆	378/225	320	1.7/2.5	3.3	0.9	2.53	N
4◇	280/200	435/150	1.9/0.39	4.2	1.5	2.45	Y
5	360/230	400	3.8/0.6	3	2.0	2.64	Y
6◇	328/240	530	5.8/6	5.5	1.2	1.70	Y
7⋆	303/155	220±40	1.29/0.98	4.3	1.8	1.47	N
8⋆	425/318	310/574	8.6/5.6	6	3.5	0.9	N
9⋆	500/350	260	0.98	3.8	/	0.64	N

[a]9 Flux sheet emergence events are labeled as (⋆) and flux loop emergence events are labeled as (◇) after event numbers. Maximum/average field strengths of each event are presented in columns (2) and (3). Positive/negative vertical flux increments of through the emergence are presented in column (4). Maximum distances and speed of oppsite polarity separation in the emergence phase are presented in column (5) and (6), respectively. LOS Doppler upflow speeds are presented in column (7). Emergence event associated with EB observation in Hα is labeled as Y and emergence without EB association is labeled as N in column (8). Event 5 is excluded from discussion in Section 5.3.3.

later forms a newly emerged granule cell. The emerging horizontal field expands its boundaries in the directions both along and across the field lines while the field lines within granule cells are aligned between concentrated footpoints of opposite polarities. We also found that on average the horizontal magnetic field strength (265 G) is comparable with the vertical field (272 G) in the emergent area as both

are enhanced during sheet emergence. Despite small variations in individual cases, the emerging flux expands its front at a speed of 1.5 km s^{-1}($\pm$0.55 km s^{-1}). In event 1 we observed the highest speed of emerged footpoints at 2.1 km s^{-1}, and in event 8 we observed the lowest speed at 0.8 km s^{-1}. TiO images show that the photospheric granular structures associated with emerged footpoints' separations undergo expansion during the flux emergence process, then follow the typical life cycle of photospheric granulation.

By reviewing the time-lapse movies of event 1 in multi-wavelengths, we identified continuous flux emergence and evolving granulation structure, which belong to the flux-sheet emergence type. The event 1 lasts $\sim$50 minutes, during which the TiO images and horizontal magnetic field maps clearly show two stages of the emergence process. Figure 5.2 shows the temporal evolution of magnetic and continuum structures of this event. Figure 5.2(a1–a8) present snapshots of image sequence from 21:46 UT to 22:06 UT of vertical field superimposed with horizontal field vectors, whose directions are represented by colors and magnitude is represented by arrow length. The cutoff value of the horizontal field vectors is 100 G. Figure 5.2(b1–b8) show TiO images overlaid with the same horizontal field vectors as in Figure 5.2(a1–a8). From Figure 5.2(b3–b4), we clearly observe that the disoriented field vectors overlap entirely an expanding granule. Figure 5.2(c1–c8) present TiO images superimposed with vertical magnetic elements, with the green (red) contours representing negative (positive) magnetic field at a magnitude of 150 G. The concentrated magnetic elements are seen to be located at the intergranular boundaries as new fluxes emerge to the photosphere [96]. In the region where flux emergence occurs (blue circle in Figure 5.2(a3) and (b3)), concentrated magnetic elements divert along the intergranular lanes near the western edge of the region and eventually merge with pores of the same polarities (as shown throughout Figure 5.2(a1–a8)). For a very short period of $\sim$10 minutes (as seen in first four columns in Figure 5.2), a granule

cell appears near the edge (centered at [X,Y]∼[5″,5″]) of a pre-existing granule and grows in the circled region with the overlying horizontal field emerging in the direction nearly perpendicular to the predominant direction of ambient fields. The translational motion of negative magnetic elements along the intergranular lane is observed at the western side of the circled area in Figures 5.2(a5–a7) and (c5–c7).

The background field in the studied region is approximately in the east-west direction. At the start of the time sequence in Figure 5.2, granulation is accompanied with the growth of a new granule cell. Along with the disoriented granule expansion occurrence (Figure 5.2(b3)), the accompanying horizontal field emerges in an organized direction different from the pre-existing field. The newly emerged horizontal field extends its boundary as it enhances in 8 minutes. In Figure 5.3, enhanced horizontal field patches are observed at ∼21:47 UT and two minutes later, the enhanced fields reach the boundary of the co-spatial granule, where vertical magnetic fields concentrate into footpoints as indicated by the red and green contours (shown in Figure 5.3(a4–a6)). The noticeable enhancement of the horizontal field at the granule's west edge as seen in Figure 5.3(a5) is associated with a developing dark lane. When the vertical field is concentrated to the extended intergranular lanes as shown in Figure 5.2(a6), the horizontal field continues to enhance (Figure 5.3(a5–a7)). The most prominent enhancement covers the elongated granule and intergranular dark lane. From the dopplergrams in Figure 5.3(b1–b8), both upflows and downflows are observed in the flux sheet area (centered at ∼[4″,5″] in Figure 5.3(b3–b4)). Strong Doppler blue-shifts (red-shifts) with upflow (downflow) velocity up to 1.8 km s^{-1} are observed at the positive (negative) footpoints in the intergranular lanes (centered at ∼[6″,6″] in Figure 5.3(b6)). Very weak blue-shifts are seen within the granular cell (centered ∼[4″,6″] in Figure 5.3(b6)), where the average Doppler upflow velocity is ∼0.4 km s^{-1}. This is roughly two times smaller than that of emerging flux in the

previous study of Centeno et al. [29], and is also smaller than the average upflows (downflows) of 0.64 (0.49) km s^{-1} as found by Oba et al. [147].

To further analyze the magnetic evolution associated with flux emergence, we present the time-distance diagrams of horizontal field and TiO image in Figure 5.4(a)–(d), which display the time-distance evolution of two slits across the flux sheet and along negative footpoint trail indicated in Figure 5.4(f) as red and yellow curves, respectively. Figure 5.4(a) clearly shows the enhancement of horizontal field in the expanding granule, in which the separating bright lanes represent the emerging horizontal field with a magnitude over 150 G. The associated bi-directional extending granule boundaries are presented in Figure 5.4(b) based on TiO observations. The observations show that the emergence in the granulation starts at 21:46 UT, when the horizontal field starts to increase from the background field and fills the granule interior. The ongoing emergence lasts ∼15 minutes before dark intergranular lanes form in place at ∼22:02 UT. The concentrated footpoints (as indicated by the green contours in Figure 5.4(e)) at the boundary continue to evolve with an expansion speed of ∼1.7 km s^{-1}. Associated with the horizontal field emergence in the transverse direction, the front of the growing granule as indicated by TiO dark lanes (seen in Figure 5.4(b)) expands at the same speed. The time-distance diagram (shown in Figure 5.4(c)) along the yellow slit indicates that the motion of the negative magnetic element resides in the intergranular lane. Its speed of motion along the slit is 2 km s^{-1}. Figure 5.4(d) shows the co-spatial TiO evolution in the intergranular lane. Although granular boundaries are observed as dark lanes in TiO images, we find that the concentrated magnetic elements are associated with transient TiO bright points. The negative magnetic elements and the co-spatial TiO bright points drift together along the intergranular lane. The horizontal field in the flux sheet emergence event 1 increases throughout the 20 minutes evolution, reaching up to 450 G. The newly emerged vertical flux at the negative footpoint is 1.3×10^{18} Mx.

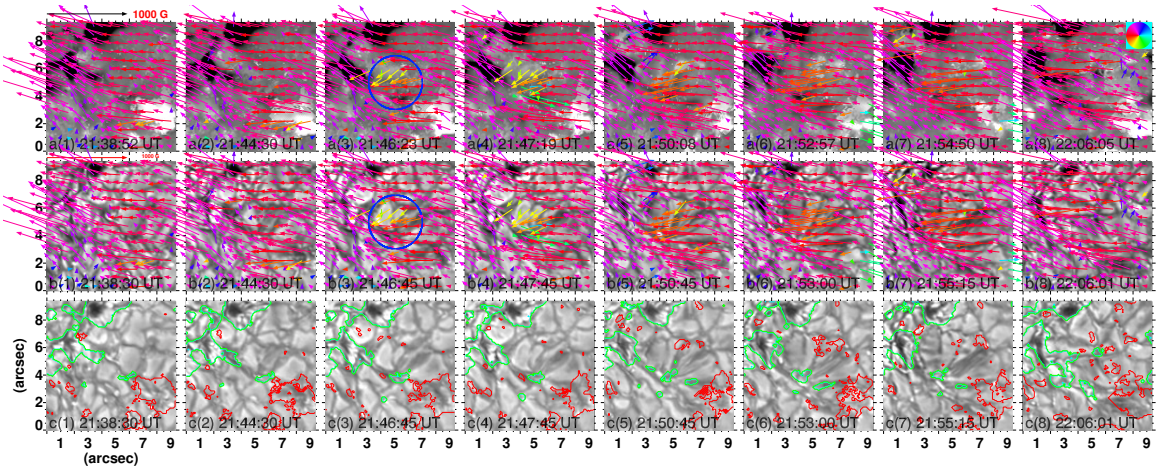

Figure 5.2 Temporal evolution of emergence event 1. The figure shows snapshots of emergence event 1 from 21:46 UT to 22:06 UT. Panels (a) show vertical field superimposed with horizontal field vectors, whose directions are represented by vector colors and magnitude is represented by length. Panels (b) show horizontal field on top of TiO images. Panels (c) show TiO images overlied with vertical magnetic elements, the red (green) contours represent positive (negative) magnetic elements at level of 150 G. The blue circle in Figure 5.2(a3) and (b3) indicates the location of emergent flux sheet with correspondent expanding granule in the background.

5.3.2 Detailed Study of a Flux Loop Emergence

On the other hand, in regions where events of emerging granules take place less often, we observed dumbbell-like features in magnetograms representing flux loop emergence events, with two ends of loops rooted in opposite magnetic polarities. The emergence of magnetic concentrations originates in the boundaries of neighboring granules and then the emerged elements move along the magnetic network. A relatively weak field connects the two emerged footpoints. It is seen that the emerged magnetic footpoints do not alter the overall evolution of their nearby granules. The passage of flux loop footpoint motions shifts following the nearby granule emergence and decay, which means that the merged flux loop does not dominate the local magnetic field and structure evolutions. By comparing averaged field strength we found that the emerged vertical field is 326 G, which is ∼120 G (60%) higher than the emerged horizontal field (∼200 G). We observe TiO and Hα brightenings more often in this

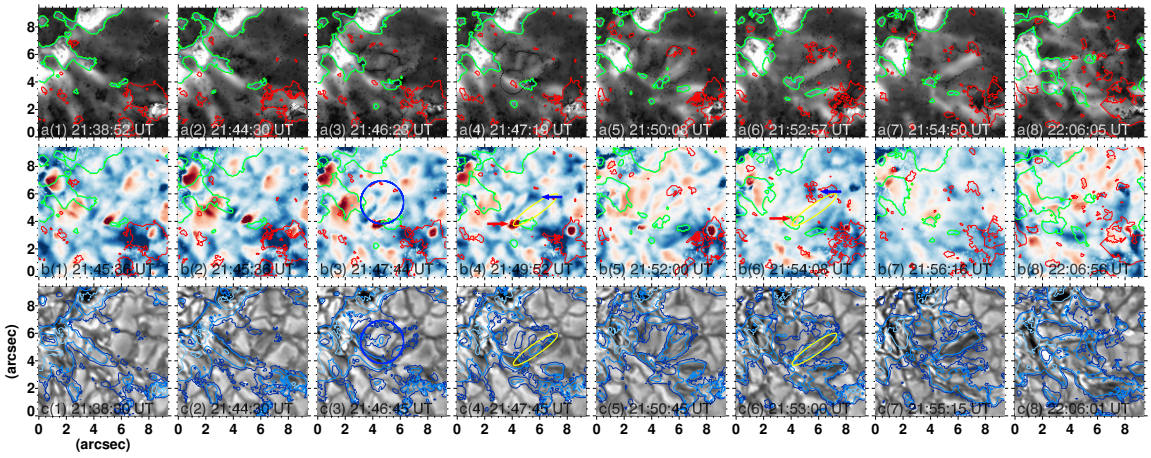

Figure 5.3 Horizontal field and dopplermaps in event 1. Panels (a) show horizontal field map superimposed with vertical field contours at level of 150 G. Panels (b) show upflows (downflows) of Dopplergrams in blue (red) color. The line-of-sight component the correspondent velocity is in range of ± 3.0 km s^{-1}. Panels (c) present TiO images superimposed with horizontal field contours at levels of 200 G and 400 G, indicated by dark and light blue, respectively. The green (red) contours in (a) and (b) represent magnetic elements of negative (positive) polarity at level of 150 G. Blue circle in (b3) and (c3) indicate the location of expanding granule. intergranular lane is outlined with ellipse in (c4) and (c6). Blue (red) arrows in (b4) and (b6) indicate strong Doppler blue-shift (red-shift) at footpoints.

flux loop type of emergence. In particular, all three events are seen to be spatially associated with Hα brightenings near the emerged magnetic footpoints.

Event 2 (indicated by the box F2 in Figure 5.1) is one of the distinctive magnetic loop type of flux emergence in our observations, in which the emerging magnetic footpoints travel in the network along intergranular dark lanes and are connected by an arched magnetic field. With the aid of Hα off-band images, we also observe Ellerman bombs at the negative polarity footpoint and additional brightenings at the central location in this event.

Figure 5.5 shows the temporal evolution of the elementary flux emergence that forms a magnetic loop configuration using the magnetic and continuum observations. In the snapshots of vector magnetic field maps (as shown in Figure 5.5(a1–a4)), horizontal field vectors are superimposed on vertical fields and are also overplotted

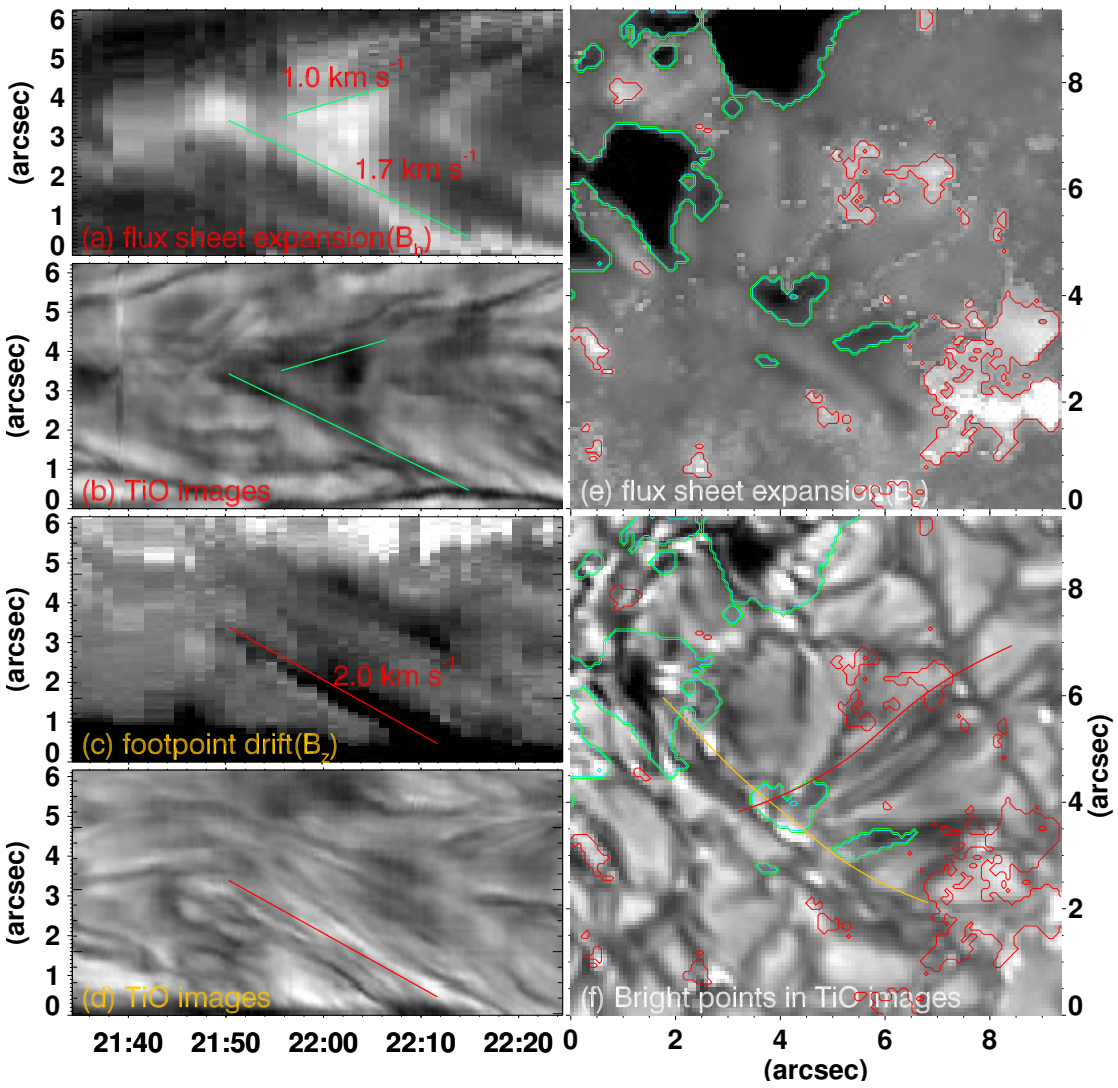

Figure 5.4 Time-space diagram of event 1. Panels (a) and (b) show time-space diagrams of horizontal field and TiO along the red slit as shown in (f), which correspond to flux sheet emergence stage. Green lines in (a) and (b) trace the expanding granule. Panels (c) and (d) show time-space diagrams of vertical field and TiO along the yellow slit as shown in (f), which represent negative footpoint motions in the intergranular lane. Red lines in (c) and (d) trace and are used to estimate speed of motion of the magnetic element. Green (red) contours in (e) and (f) outline the concentrated negative (positive) magnetic elements.

on TiO images (Figure 5.5(b1–b4)). The direction of the horizontal field is indicated by the direction of the arrow and displayed in different colors for each direction, and the positive (negative) vertical field is indicated by the white (black) background. Figure 5.5(c1–c4) and Figure 5.5(d1–d4) show Hα images at +1.0 and −0.4 Å,

respectively, with the overplotted green (yellow) contours representing the negative (positive) magnetic elements at the level of 150 G. From the image sequence, we can see consecutive episodes of flux emergence during the time of observation in the event 2 region.

Starting from 21:13 UT, a new pair of magnetic elements appear at $\sim$[4.5″,3.5″] (Figure 5.5(a1)). The concentrated magnetic elements of opposite polarities continue to strengthen as they separate (as shown in Figure 5.5(a1–a3)). It is noticeable from vector maps that the horizontal field enhances in place with the emerged magnetic elements and connects the diverging footpoints. A loop-like magnetic field structure is observed between the footpoints FP2 and FP3 at 21:46 UT, and the width of the field loop reaches $\sim$1″ as observed for its horizontal field component (Figure 5.6(a3)). There is no obvious granular elongation observed to be associated with this horizontal field enhancement, while a deformed granule is accompanied by a transient magnetic enhancement between the footpoints FP2 and FP3 (see Figure 5.5(a3)). The diffuse field can also be observed in Figure 5.6(a1–a4), which show the horizontal field map superimposed with vertical field contours at the level of 150 G. The green and red contours represent negative and positive magnetic elements, respectively. The Dopplergrams in Figure 5.6(b1–b4) show obvious red-shifts at footpoints and two blue-shifted patches connecting the footpoints at $\sim$21:35 UT. This indicates that the loop between footpoints has an upward motion and the footpoints have downward flows. The upflow speed reaches up to 1.8 km s^{-1}. The emerging magnetic footpoints start to cancel with the preexisting magnetic fields of opposite polarities from 21:46 UT. Such configuration of the emerged magnetic arc and the nearby preexisting footpoints in the north of the region may indicate the emergence of an undulating field in the emergence on the photosphere. Adjoining footpoints of opposite polarities in the emergent undulating field can easily organize a U-shaped or Ω-shaped bald patch. According to previous studies (e.g., [152, 209]),

the photospheric locations of bald patches of serpentine magnetic fields are very likely to be associated with EBs. In the event 2, we witnessed bald patch associated EBs between the footpoints FP1 and FP2 (see Figure 5.5 a4 and c4), where the brightening in Hα wing occurs when the magnetic concentrations of opposite polarities approach each other. The separation of emerged magnetic footpoints eventually reaches a maximum distance of 5 Mm at 22:02 UT. In Figure 5.5(c4), Hα brightenings at +1.0 Å off-band are observed at the magnetic footpoints ([2″,7″]) of the emerging flux at 22:02 UT, when the magnetic flux cancellation occurs. At the same time, one can clearly observe a brightening in Hα −0.4 Å centered at ∼[4″,3″] (Figure 5.5(d4)) between the magnetic footpoints.

The time-distance diagrams in Figure 5.7 display bidirectional motions of the emerging magnetic elements. Similar phenomena were reported by Yang et al. [260] with TiO broadband filter images. The slit cuts along the extending magnetic loop as shown with the yellow curve in Figure 5.7(c). Based on the time-distance diagrams, the magnetic footpoints diverge at a speed of 0.6–1.4 km s^{-1}, which is much slower than previous results (3.8 km s^{-1} in Yang et al. [260]). While the vertical fields follow confined separating traces, slightly weaker horizontal fields develop between the extending front of the horizontal field as seen in Figure 5.7(b). This is consistent with the observation from vector magnetic field maps that the magnetic footpoints are connected by diffused horizontal fields [30, 130].

To understand the relationship between flux emergence and Hα brightenings, we plot the temporal evolution of footpoint magnetic flux, Hα intensities at −0.4 Å and +1.0 Å, and horizontal field strength in Figure 5.8. Figure 5.8(a) shows the averaged vertical flux in the positive (negative) footpoints as a red (blue) curve. Figure 5.8(b) shows the normalized intensity of Hα −0.4 and +1.0 Å in the central loop (blue) and footpoint (red) regions, respectively. Figure 5.8(c) shows averaged horizontal field in the same central loop (blue) and footpoint (red) regions. In the first phase

of emergence, there is no visible Hα response, while we observe brightenings in the loop corresponding to the second horizontal field increase starting from 21:46 UT. Comparing the light curves of the horizontal field at different locations, we find that the field strength increases at footpoints while decreases in the loop at ∼22:02 UT, which is co-temporal with Hα brightenings. Meanwhile, the vertical flux increases at the negative polarity footpoint. We speculate that Hα brightenings in the loop are produced by the magnetic reconnection between the newly emerged magnetic loop with the overlying background field. On the other hand, the Hα brightenings at footpoints are likely to be signatures of EBs between FP1 and FP2 (see Figure 5.5(a3)). The LOS velocity maps of event 2 in Figure 5.6(b1)-(b4) show that the central loop and magnetic footpoints of the emerged flux loop is clearly associated with bi-directional shifts. At 21:13 UT, the velocity of blue-shift corresponding to the emerging loop is 0.45 km s^{-1}. It increases to 0.98 km s^{-1} at 21:28 UT then decreases to 0.37 km s^{-1} at 21:46 UT. The separating footpoints are observed to experience red-shifts with a maximum speed of 1.3 km s^{-1} at 21:28 UT.

5.3.3 Properties of Other Events

Starting from 21:00 UT, with best-seeing quality of the day, we observe other small-scale flux emergence cases in ∼70 minutes, which demonstrate similar magnetic properties. The derived parameters of magnetic field evolution observed in nine events are given in Table 5.1, including horizontal field, vertical field, vertical flux increments, the maximum distance of emerging bipolar magnetic elements, correspondent separation speed, LOS Doppler velocities, and associated EB occurrence. The maximum distance and correspondent average speed are measured in the emergence phase, which starts from the emergence of opposite polarities till both separation and flux enhancement cease. As listed in Table 5.1, five of the eight selected events in the observation can be categorized as a flux sheet type of emergence.

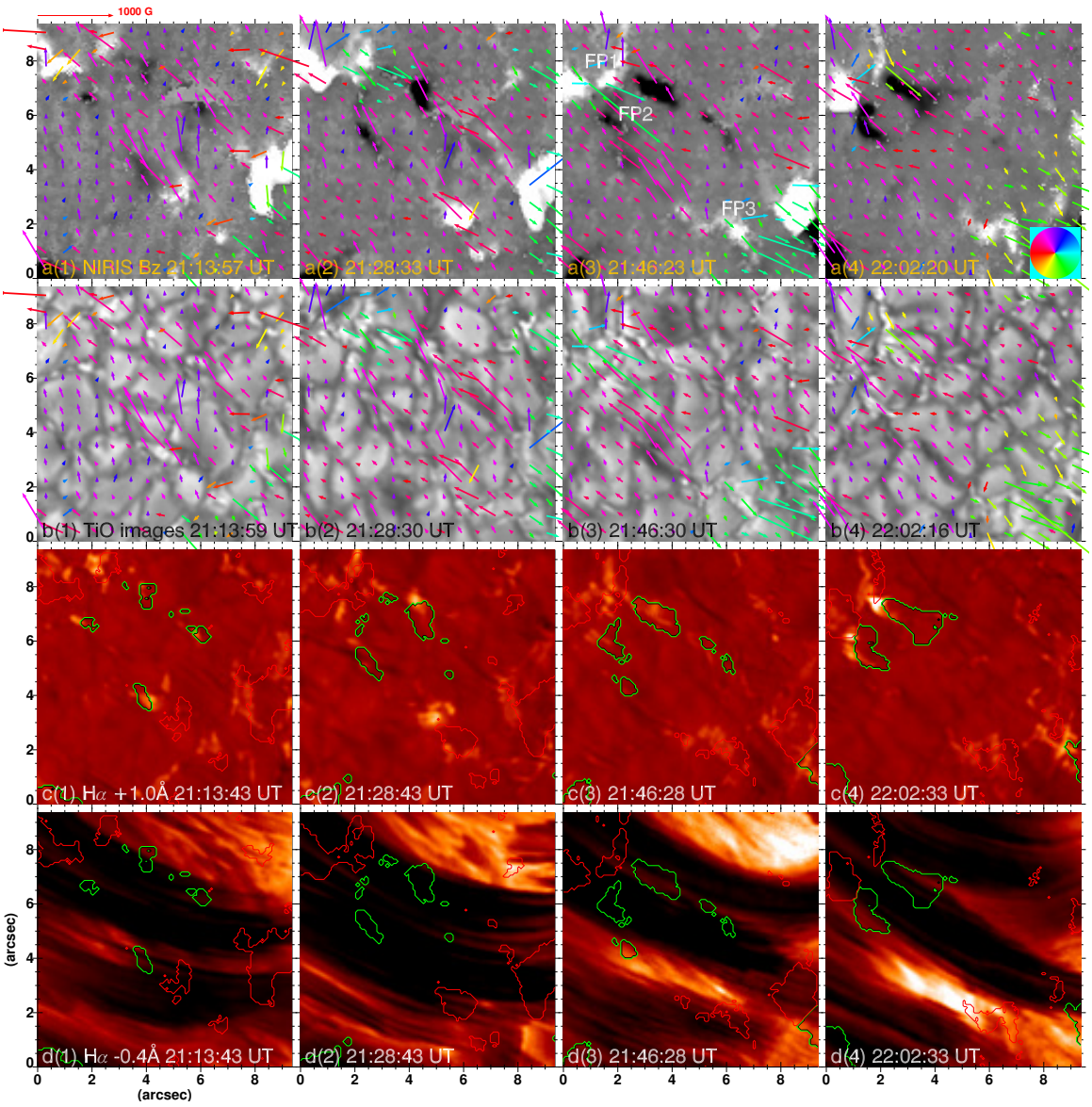

Figure 5.5 Temporal evolution of emergence event 2. The figure shows snapshots of emergence event 2 from 21:13 UT to 22:02 UT. Panels (a) show vertical field superimposed with horizontal field vectors, whose directions are represented by vector directions and magnitude is represented by length. Panels (b) show TiO images overlied with horizontal field vectors. Panels (c) and (d) show Hα images at +1.0 and −0.4 Å, the green (red) contours represent negative (positive) magnetic elements at level of 150 G.

We find that although the time interval between horizontal field emergence and the corresponding expanding granule boundaries is within 10 minutes, which is at the same time scale as summarized in previous studies [29, 144], magnetic elements in the

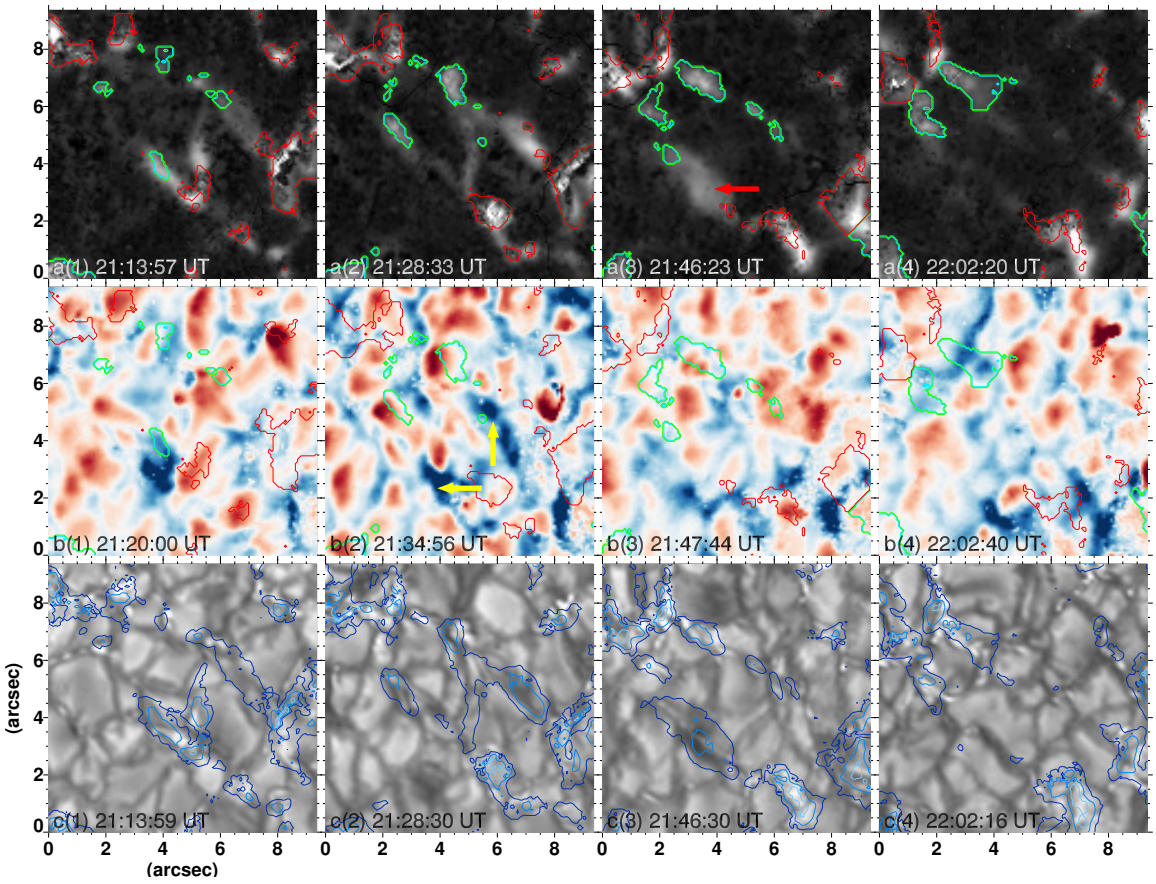

Figure 5.6 Horizontal field and dopplergrams in event 2. Panels (a) show horizontal field map superimposed with vertical field contours at level of 150 G. Panels (b) show upflows (downflows) of Dopplergrams in blue (red) color. The line-of-sight component the correspondent velocity is in range of ± 3.0 km s^{-1}. Panels (c) present TiO images superimposed with horizontal field contours at levels of 200 G and 400 G, indicated by dark and light blue, respectively. The green (red) contours in (a) and (b) represent magnetic elements of negative (positive) polarity at level of 150 G. The red arrow in (a3) indicates horizontal component of the magnetic loop. The yellow arrows in (b2) indicate Doppler blue-shifts between the magnetic footpoints.

granule boundaries continue to enhance as horizontal field increases and then either merge with adjacent magnetic fields or cancel with elements of opposite polarities. The flux sheet emergence events 1 and 8 are observed to originate from intergranular dark lanes and form new expanding granular cells in the emergence locations. While the other three emergent flux sheets (events 3, 7, and 9) do not show a direct linkage to pre-existing intergranular dark lanes, they are found to be located near the newly

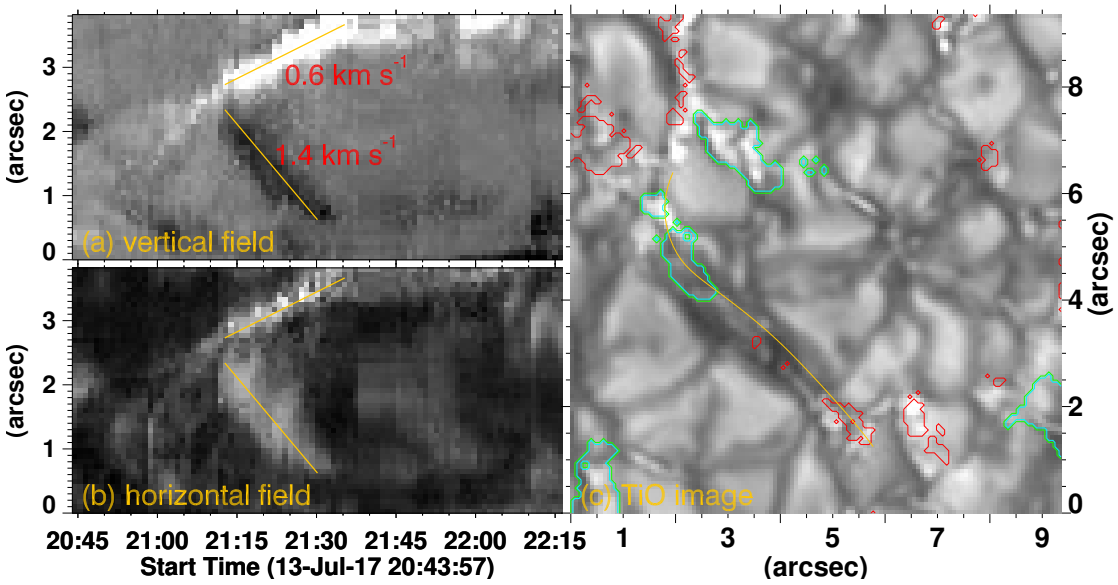

Figure 5.7 Time-space diagrams of event 2. Panels (a) and (b) show time-space diagrams of vertical and horizontal field along the slit in the TiO image as shown in (c). Yellow lines in (a) and (b) trace and are used to estimate the speed of separation of the emerged magnetic polarities. Green (red) contours outline the magnetic elements of negative (positive) polarity.

formed pores. The vertical flux brought into the solar surface through emergence, which is associated with the expanding granules, is in the range of 0.9–11.6$\times$ 10^{18} Mx. As the edge of the emerging magnetic field that envelopes the granule expands at a speed of 1.5 km s^{-1}, the granule cells undergoing emergence are averaged 4.3″, which grow by 0.7–1.5″. Although we observed a close connection between magnetic flux emergence and changes of photospheric granule structure, Hα brightenings are rarely observed to be associated with flux sheet emergence. Hα bright bursts captured in the event 9 region are closely associated with magnetic flux cancellation starting from 20:16 UT. During its emergence, TiO brightening at the granular boundary is observed at 21:36 UT.

Summarizing the flux loop cases, we find that the vertical flux enhancement in this type of events is 3.0$\pm$0.9$\times$ 10^{18} Mx.while the separation speed of the emerging loop footpoints is 1.2 km s^{-1}, which is similar to the expanding speed of horizontal

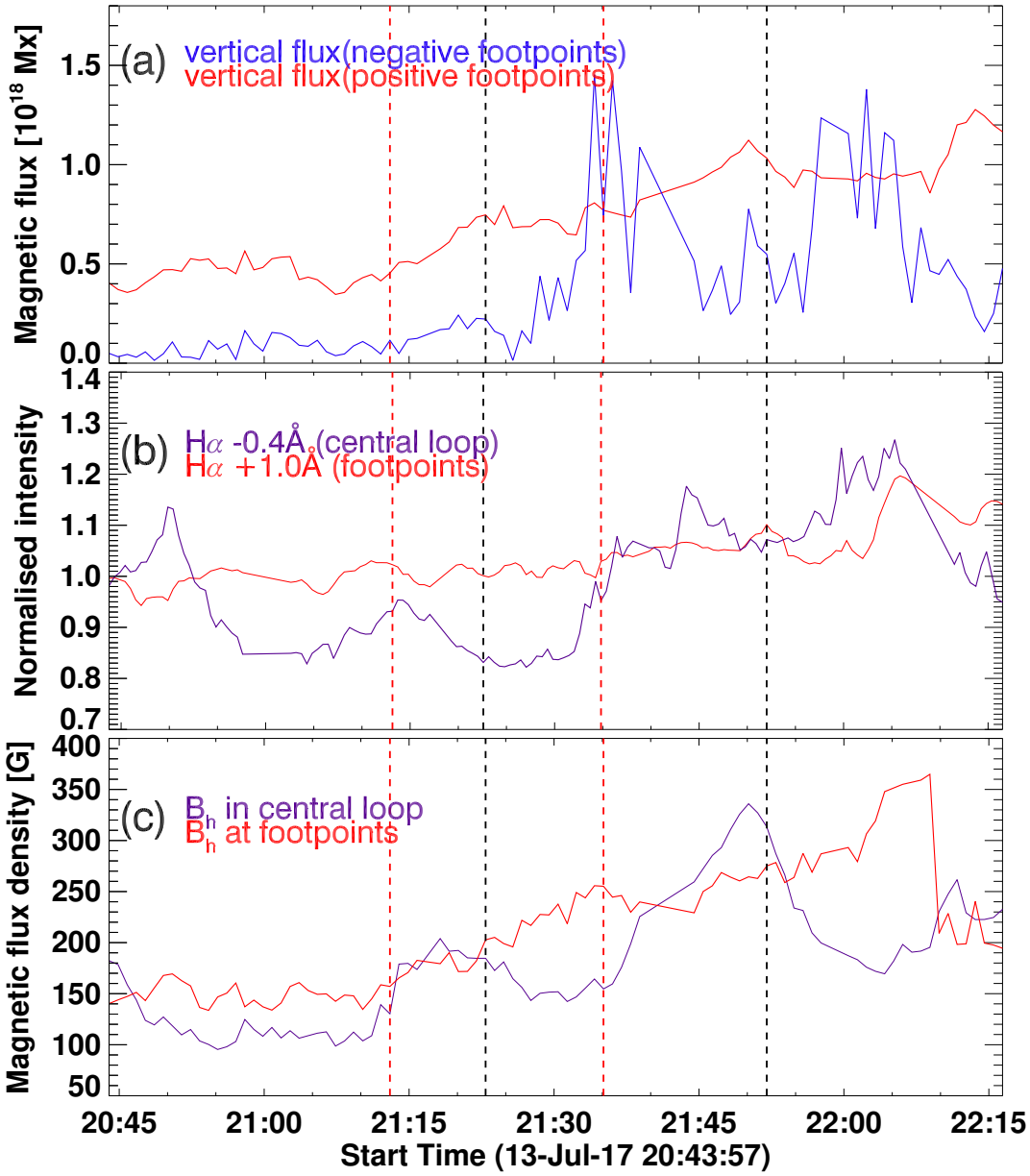

Figure 5.8 The evolution of magnetic flux, mean brightness, and magnetic fields in event 2. Red and blue light curve in (a) shows averaged vertical flux evolution at footpoints FP3 and FP2 in Figure 5.5, respectively, in unit of 10^{18} Mx. Blue (red) light curve in (b) shows normalized intensity of Hα -0.4 Å($+1.0$ Å) in the loop (at footpoint FP1). Blue (red) light curve in (c) shows horizontal field in the loop (footpoints) in unit of Gauss. Dashed lines in figure mark two episodes of flux emergence, with red (black) dashed line represents start (end) time.

field in flux sheet emergence, the maximum distance of opposite polarities reaches $5.5\pm1.5''$. The difference of maximum separation is consistent with flux sheet and

loop topology as magnetic footpoints of emerging flux loops are expected to extend further in the granular network. Despite that Hα brightenings are observed in event 2 at end of the flux emergence, the most prominent Hα response occurred 38 minutes later. In the other two flux loop emergence events (event 4 and 6), we also observed Hα brightenings close to the emerged footpoints of these two events, while time intervals between emergence and Hα brightenings do not show a similarity. In event 6 Hα brightenings are observed three minutes after loop emergence. Among the studied events, five events are spatially associated with Hα brightenings, including all three flux loop emergence and two flux sheet emergence. From Doppler velocity maps of the flux emergence events, we find that the active region generally shows an upflow of 0.8 km s^{-1} in the background. Three of the listed emergence events (events 3-5) have blue-shifts over 2 km s^{-1}, which is comparable to previous observational results of photospheric Doppler velocity [148]. Event 5 is excluded from the categorization of magnetic topology because azimuthal ambiguity is not well resolved at the event location and Doppler red-shift is observed between opposite polarities. It is interpreted as a U-shaped field.

5.4 Summary and Discussion

In this study, we have presented a detailed study of small-scale flux emergence near the central PIL of NOAA AR 12665 on 2017 July 13. The study is particularly focused on magnetic characteristics of two different kinds of flux emergence derived using the near-infrared polarimetric data obtained by NIRIS at BBSO/GST. In addition, we studied photospheric evolution and chromospheric responses to the flux emergence using TiO and Hα time-sequence images. Our main results are summarized below.

1. In event 1, a typical sheet emergence case, an organized sheet-like structure of enhancing horizontal magnetic flux is seen to span over an entire granule, which expands at a speed of 1.6 km s^{-1}. The magnitude of the horizontal field in the flux sheet increases for $\sim$20 minutes, reaching up to 450 G. The emerged flux at footpoints reaches $\sim$1.8$\times$ 10^{18} Mx. In a subsequent second stage, the

negative polarity footpoints and the co-spatial TiO bright points move along the intergranular lanes at a speed of $\sim$2 km s^{-1}.

2. In event 2, a typical loop emergence case, magnetic footpoints at the two ends (the concentrated opposite-polarity flux component) emerge and move in the intergranular lanes with a separation speed of 1.2–1.7 km s^{-1}; meanwhile, a horizontal field lying in-between enhances, forming elongated, loop-like structures (the central diffused component). The positive vertical flux increases by $\sim$0.5$\times$ 10^{18} Mx. Later at $\sim$22:00 UT, horizontal field decreases in the central loop region while it increases at footpoint regions.

3. Analysis of extended samples shows that all the eight events have a strongly emerged horizontal field of $\sim$450 G at maximum. While in the flux sheet emergence vertical field is comparable with the horizontal field($\sim$270 G), in the loop emergence vertical field is 120 G stronger than the horizontal field. In the five flux sheet emergence events, the horizontal field enhances and hovers the emergent granule cells as the granules grow. The concentration of field strength in the granule boundaries at the late phase of the emergence is observed in both horizontal and vertical magnetograms. Three out of the eight emergence events are observed to have a magnetic loop topology, in which the emergence of magnetic elements happens in intergranular lanes. The loop-like emergence carries $\sim$10^{18} Mx of flux to the surface.

The results of the two types of flux emergence, with one experiencing an enhanced horizontal field hovering over the granule and the other following the typical Ω–loop configuration, have advanced our understandings of small-scale flux emergence and formation of active regions. It is worth noting that observations of flux-sheet emergence in both active regions [29] and quiet Sun [60] are rare. The numerical study by Moreno-Insertis et al. [144] suggested that the occurrence rate of loop-like emergence (1–3 day^{-1} Mm^{-2}) is $\sim$3 times higher than that of the sheet-like events (0.3–1 day^{-1} Mm^{-2}) in the quiet Sun. In our study, we found more frequent occurrence of flux-sheet emergence events (1.8$\pm$0.1 day^{-1} Mm^{-2}) than of loop-like emergence (1.1$\pm$0.06 day^{-1} Mm^{-2}). We suspect that in the active region sub-surface magnetic tubes rising up to solar surface can break their original bipolar structure and emerge sideways due to the active and dynamic transverse motions. Frequent granulation observed in the active region provides higher opportunity than in quiet Sun to have magnetic tubes emerge with growing granules, which eventually form

an emerging flux sheet. In comparison with a previous study, Fischer et al. [60] observed that the transverse flux density reaches up to 194 Mxcm^{-2}, corresponding to a maximum horizontal field of ∼300 G. Our results show that the horizontal field reaches up to 450 G while the total flux is comparable to previous studies. Based on our results, five out of the eight observed flux emergence episodes in the FOV follow the flux-sheet type of emergence, and the rest follows the loop type emergence. Further, the flux sheets often appear in the emergence sites that are closely associated with newly evolving granulations. Such a preference leads us to speculate that not only magnetic buoyancy instability but also transverse tension contribute to the flux-sheet emergence. In both types of flux emergence, the maximum distance of footpoint separation and speed of Doppler shift vary with cases. Base on the results of our analyzed events, we conclude that despite differences in magnetic field topology and field strength distribution, the flux sheet and flux loop emergences share some similarities in terms of the emerging process. As an indication of Ellerman bombs, Hα brightenings in our observations are found to have a close connection with magnetic loop emergence, in which the migrating footpoints collide and cancel with elements of opposite polarity in the intergranular lanes.

The magnetic-loop emergences observed by us may evolve in the form of an undulating serpentine field. The three confirmed loop type emergences are observed in the magnetic intranetwork. As magnetic footpoints diverge along the intergranular lanes, the emergent horizontal field is observed to enhance the field strength of network in magnetograms with correspondent dark lanes seen in TiO images. Despite different emergence topology, the total emerged magnetic flux in the loop emergence events is comparable with that in the flux-sheet emergence events, and is an order of magnitude higher than previous studies of granule-sized magnetic loops [69]. As presented in the sample event 2, the magnetic footpoints of opposite polarities originate within neighboring granules and move apart along the intergranular lanes. Thus as they

approach the adjacent footpoints of the emerged field, a U-shaped field line can be formed across the surface. Such magnetic field configuration is one type of bald patches that are found to have a strong connection with EBs [152, 95]. Vissers et al. [218] found that similar to EBs, flaring arch filaments could also exist in the emerging active region but are often observed as brightenings at Hα core. This phenomenon is believed to be related to the reconnection of curved fields. In comparison, our results in Section 5.3.2 reveal Hα brightenings at the central loop location (in -0.4 Å) as well as at the footpoints (in $+1.0$ Å). These may be interpreted as the reconnection between the emerging flux loop (footpoints) with the pre-existing overlying field (opposite polarity elements).

In summary, with high-resolution and high-cadence vector data, we have studied small-scale flux emergence from the observational perspective. We confirm that magnetic fields of granule-sized flux emergence have two different topologies, magnetic loop and flux sheet. The primary difference of magnetic properties between the two types of emergence is that the magnetic field of flux sheets tend to be more inclined than arched magnetic loops. In association with the flux emergences, Hα brightenings are more favorable to the footpoints of the emerging magnetic loops. Also, despite their different locations in the observed AR, both types of emergence bring 1–6$\times$ 10^{18} Mx of flux to the solar atmosphere.

CHAPTER 6

A HIGH-RESOLUTION STUDY OF MAGNETIC FIELD EVOLUTION AND Hα SPICULES AROUND A CORONAL HOLE

6.1 Introduction

In general, network field, intranetwork (IN) field, and ephemeral regions form the quiet Sun (QS) magnetic field. Coronal holes in the QS regions are usually seen as dark regions in the X-ray and EUV observations due to reduced emissivity in X-ray and EUV wavelengths (for reviews see, e.g., [39, 239]). Formation of the non-polar region coronal holes can be resulted from decay of active regions [101, 68] and eruptive activities [80]. One of the important photospheric magnetic characteristics is the highly unbalanced magnetic flux residing in the concentrated flux tubes in coronal holes [84], which leads to dominance of a certain polarity in the coronal holes. Plumes, fountain-like coronal structures, are often observed in the unipolar magnetic concentrations in coronal holes [249]. Although the unipolar magnetic flux tubes are considered as a fundamental sector of a coronal hole and dominate its evolution, high-resolution magnetograms show that opposite polarities of small-scale magnetic elements have a random distribution in the QS as well as in the coronal hole. [247] studied magnetic properties of twelve coronal holes and eight QS regions using magnetograms taken by Michelson Doppler Imager (MDI) on the solar and heliospheric observatory (SOHO) for comparisons. The authors found that a significant amount of signed magnetic flux (77$\pm$14%) in the coronal hole is stored in open field, while the short and low-lying closed-loop field is reported in both the coronal hole and QS regions. These closed loops in the coronal holes may play an important role in the "switchbacks" in the solar wind [62], in which the interchange reconnection is proposed to occur between the coronal loop and open field and results

in a smaller loop and enhanced open magnetic flux transport. With new observations by the Parker Solar Probe (PSP), [63] validated that open magnetic flux is transported by interchange reconnection and the accompanying spikes occur in all types of solar wind (e.g., slow solar wind, fast solar wind, Alfvénic slow solar wind near coronal hole boundary).

On the other hand, photospheric magnetic field measurements have been taken to study small-scale magnetic transients. Ubiquitous magnetic flux cancellations often occur in the network field of granules, mesogranules, and supergranules with convergence of opposite polarities. The problem of chromospheric and coronal heating can be addressed by studying cancellations of magnetic flux from convection flows in association with small-scale jet-like ejections. For decades, the study of spicules has been a hot topic and our understandings of enegy budget in QS and coronal holes are greatly advanced with improvement of spatial and temporal resolutions of observational instrument. Such small-scale jet-like ejections are characterized as short-lived eruptive plasma bounded at network boundary of opposite magnetic polarities (for a review see, e.g., [212]). [225] proposed Hα macrospicules as a manifestation of magnetic reconnection, likely caused by the network-ephemeral region or network-IN interactions. With high-resolution observations from solar optical telescope (SOT) of Hinode, [42] found two types of spicules: "Type-I" spicules that are driven by shock waves through global oscillation and convective flows leaked into the solar atmosphere on timescales of 3–7 minutes, and dynamic "Type-II" spicules that are formed through magnetic reconnection process in vicinity of magnetic flux concentrations in plage and network.

Recent Interface Region Imaging Spectrograph (IRIS) observations foud that the small-scale network jetlets propagate at speeds of 70 km s^{-1} in average lifetimes of 3 minutes [151]. The authors speculated that such network jetlet eruptions are small-scale analogs of large-scale coronal jets. Using high-resolution Hα and magnetic

field observations by Goode Solar Telescope (GST; [70]) at Big Bear Solar Telescope (BBSO), [169] found close connections between the generation of fine-scale spicules and interactions of underlying network field with ambient weak field of opposite polarity, in forms of magnetic flux cancellation and emergence. [193] argued that the emergence episodes that initiate enhanced spicular activities actually might be preparations for magnetic cancellations. They proposed a microfilament eruption model of solar spicules, which is morphologically similar to erupting minifilaments that drive coronal jets.

However, questions that are still not fully understood are whether properties of magnetic energy budget through small-scale magnetic flux evolution are universal or differ between QS and coronal hole regions, and whether the heated plasma through small-scale reconnection is sufficient for coronal heating. In this study, we present statistical properties of magnetic cancellation events and study small-scale Hα ejections associated with magnetic evolution around the boundary of a low-latitude coronal hole on 2018 July 29. Data of the high-resolution observations are taken by BBSO/GST. The structure of the chapter is organized as follows. We introduce data observation and processing methods in Section 6.2. Magnetic properties of the coronal hole and the surrounding QS regions and jet-like ejections associated with magnetic cancellations are presented in Section 6.3. Discussions based on the observational results are presented in Section 6.4.

6.2 Data and Processing Methods

On 2018 July 29, BBSO/GST observed the boundary section of a quiet Sun coronal hole located at [604″ E, 125″ S] on the solar disk with on-site post-focus instrumentations, including broad-band filter imager (BFI), visible imaging spectrometer (VIS), and near-infrared imaging spectropolarimeter (NIRIS; [23]). Taking advantage of high-order correction by adaptive optics system with 308 sub-apertures (AO-308; [24])

and solar speckle interferometric data reconstruction technique [251], the observation during ∼16:31–18:44 UT achieved diffraction-limited resolution under a favorable seeing condition. The obtained data include images in TiO filter (705.7 nm; 10 Å bandpass) by BFI with a field of view (FOV) of 77″ at 0.1″ resolution and 20 s cadence, Fabry-Pérot spectroscopic observations of the Hα line at ±1.0, ±0.8, ±0.6, ±0.4, ±0.2, and 0.0 Å (0.08 Å bandpass) by VIS with a 70″ circular FOV at 0.1″ resolution and 40 s cadence, and spectroscopic polarization measurement of the Fe I 1565 nm (0.25 Å bandpass) by NIRIS with a round FOV of 80″ at 0.24″ resolution and 42 s cadence. Each burst takes 100 and 60 frames for speckle reconstruction of TiO and Hα lines, respectively. Line-of-sight (LOS) magnetograms are reduced by performing an area integration of the Stokes V profile along the wavelength. EUV data at 193 Å from the Atmospheric Imaging Assembly (AIA; [111]) on board the Solar Dynamic Observatory (SDO) are used to identify the coronal hole and any connection with chromospheric eruptions.

In this study, Hα images and magnetograms by GST are aligned to sub-pixel presicion by matching chromospheric network. Validation of NIRIS magnetograms are conducted with LOS magnetic field measurement provided by the Helioseismic Magnetic Imager (HMI; [172]). The results show a correlation coefficient of 0.98 at strong field areas and an overall correlation coefficient of 0.72. To identify on-disk spicules, Hα intensity images at ±0.8 Å are used to calculate two-dimensional Doppler signals (DS), in which the upward moving chromospheric materials are represented as bright strands. The evolution of small-scale magnetic elements is tracked with the Southwest Automatic Magnetic Identification Suite (SWAMIS; [44]), by which the magnetic cancellation events are detected and their corresponding magnetic fluxes are calculated. In SWAMIS, we set 3 pixels (0.24″) as the minimum size of magnetic field elements for detection. To evaluate the noise in the magnetic field measurement, we select a quiet Sun area of 16×16 pixels that is away from magnetic network and has

a minimal flux variation. We then take the full-width half-maximum of a Gaussian fitted profile to the field strength of these pixels as the noise level, which is about 20 G.

6.3 Results

In the ∼90 minutes of high-resolution GST observations near the targeted coronal hole, we have observed small-scale magnetic field evolution and Hα ejections. With magnetic fields of mixed polarities filling the intranetwork around coronal hole boundary networks, chromospheric spicules are observed to actively evolve with time. The FOV of GST observation is centered at the southeast edge of the coronal hole. This coronal hole is at its end phase of boundary growth. Time lapse of magnetic evolution in the following results is with respect to the start time (16:34:18 UT) of GST observation.

Figure 6.1 shows magnetic field, EUV image, and corresponding Hα blue-wing images at 16:46:44 UT. Hα spicular activities are present in Figure 6.1(a)(d), which are mostly anchored at boundaries of the magnetic network. Plumes are also observed outside the coronal hole near the southeastern corner of the FOV during ∼17:00 UT–17:40 UT. Figure 6.1(b) shows that small bright loops that lie along the coronal hole boundary. The coronal hole boundary region is dominated with negative magnetic field with an averaged strength (defined as total flux divided by area of magnetic element) of 220 G, which is about twice the strength of positive field. Magnetic elements of positive and negative polarities are labeled as blue and red features in Figure 6.1(c). 3127 cancellation events are identified in the total of 72000 episodes of magnetic evolution.

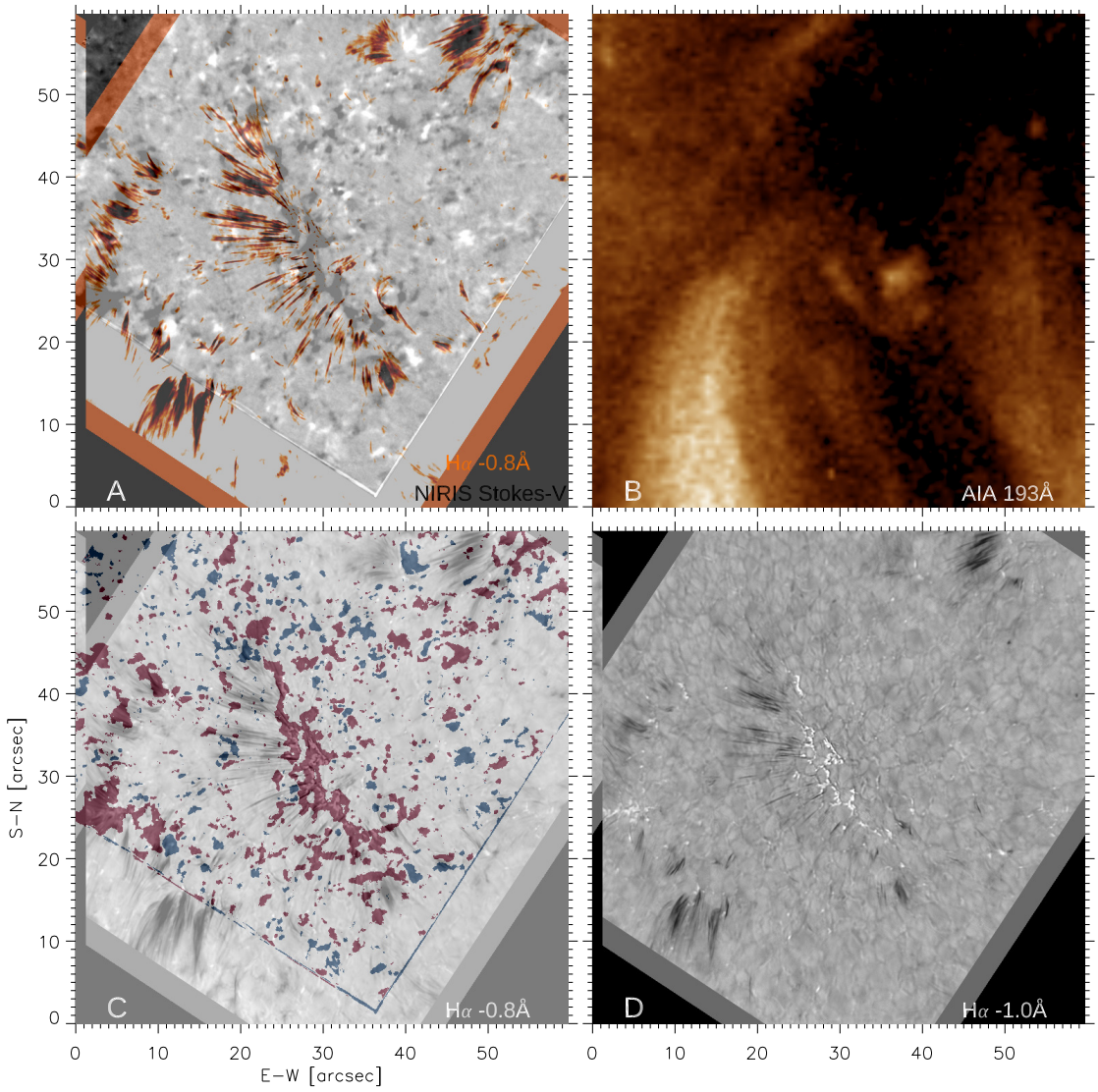

Figure 6.1 Identification of cancelling magnetic elements with corresponding Hα spicules and EUV eruptions. Panel (A) shows magnetograms at 16:46:44 UT superimposed with Hα blue wing image at -0.8 Å off linecenter. Panel (B) shows AIA 193 Å image of the same FOv, with dark area indicating the coronal hole. Panel (C) shows locations of cancellations of opposite magnetic elements with Hα -0.8 Å image in the background. Panel (D) shows Hα blue wing image at -1.0 Å off linecenter.

6.3.1 Magnetic Cancellations at Coronal Hole Boundary

Figure 6.2(a) shows the sites of cancellation events (marked as green stars) in the entire FOV. The mid-point between closest points on the edge of adjacent two

magnetic features with opposite polarities is identified as the cancellation site, which is also on the motion path of the cancelling elements. The cancellation sites are also marked in Figure 6.2(b)(c). It is noticeable that the cancellations have a higher probability of occurrence in the weak magnetic field regions than in the concentrated negative unipolar field at the coronal hole boundary. There are 1245 magnetic flux cancellation events inside the coronal hole (located northwest of purple boundary defined using the AIA 193 Å image in Figure 6.1(b)), 1589 magnetic flux cancellation events in the quiet Sun outside the coronal hole, and 222 magnetic flux cancellation events at the coronal hole boundary region (defined here as the belt region between the gray lines). The results show that the highest occurrence rate of flux cancellations, which is 1.5 Mm^{-2} hr^{-1} inside the coronal hole, While in the quiet Sun region and coronal hole boundary, the occurrence rate is 1.2 and 0.5 Mm^{-2} hr^{-1}, respectively. The yellow and purple stars in Figure 6.2(b) and (c) show locations of cancellation events that are associated with strong eruption-like events in Hα. Details of the two events located in the coronal hole (Figure 6.2(b)) and at the coronal hole boundary (Figure 6.2(c)) are discussed in Section 6.3.2.

NIRIS magnetograms show that the negative unipolar magnetic cluster along the coronal hole boundary contains $1.2\pm0.4\times10^{29}$ ergs of magnetic energy E, which is defined as

$$E = \frac{1}{8\pi}\int_0^L \int_A B^2\, dA\, dl \tag{6.1}$$

where L represents scaled height with estimated value of 100 km. The above magnetic energy makes up 63% of the total energy in the coronal hole boundary region. Figure 6.3(a) shows that the energy released by magnetic flux cancellation over the 90 minutes is in total 9.9×10^{27} ergs (red curve), with a corresponding energy release rate of 5.3 ergs cm^{-3} s^{-1}. This is comparable with energy release rate of intranetwork cancellations ($\sim$4.7 ergs cm^{-3} s^{-1}; [74]). As shown in Figure 6.3(b), the net flux of the

cancellation events increases in the negative polarity. The average net flux changes from 1.6×10^{16} Mx at beginning of the cancellations (blue bar) to -3.0×10^{16} Mx at end of cancellations (yellow bar). The size distribution of detected cancelling magnetic elements is shown in Figure 6.3(c). The lower limit of flux element size is 0.03 Mm^2, which is set by the parameter of magnetic feature size in the SWAMIS method. It is seen that 97.7% of the cancelling magnetic elements have a size under 3.0 Mm^2. The mean size of the magnetic flux elements is 0.73 ± 0.03 Mm^2 after cancellations, which is 0.8 Mm^2 smaller in area as compared to before cancellation. The lifetime of the magnetic elements has a low threshold of 45 s as limited by image cadence. Figure 6.3(d) shows that 43% of flux cancallations have a lifetime below 6.5 minutes, with a mean value of 3.7 minutes. As a result, the averaged magnetic flux cancellation rate is 1.02×10^{18} Mx Mm^{-2} hr^{-1}.

6.3.2 Magnetic Cancellations Inside and Outside of Coronal Hole

Magnetic flux emergence and cancellation in the coronal hole are related to the coronal hole's decay and growth. The AIA 193 Å observation shows that the coronal hole experiences growth in area from 2018 July 28 10:00 to 16:00 (+1) UT. During the GST observation period under study (from 2018 July 29 16:34:18 to 18:04:54 UT), the boundary of the coronal hole remains stationary. We divide the FOV of GST observation into the coronal hole region and the outside quiet Sun region, and study their magnetic field properties and evolution separately.

Figure 6.4(a) shows the averaged magnetogram over 90 minutes in the coronal hole. The average positive and negative longitudinal flux density in the coronal hole are 80 G and -130 G, respectively. The strong negative flux concentrations close to the curved edge are labeled as part of the unipolar cluster at the coronal hole boundary in SWAMIS tracking results. Hα images in Figure 6.1(a)(d) shows that flux cancellations are less often associated with enhanced spicular activities as

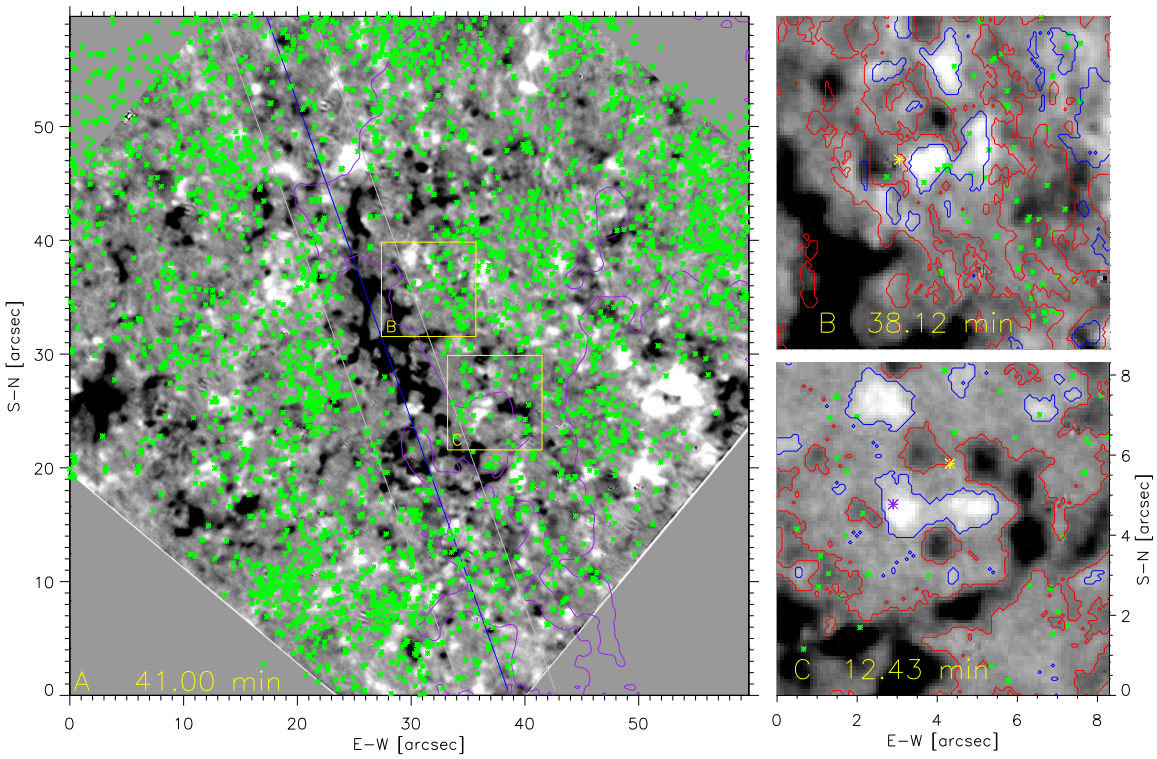

Figure 6.2 Identification of cancellation site in magnetogram. Panel (a) show locations of cancellation events occurrence. The green star symbols indicate where the opposite magnetic flux cancel out (with unsigned flux decrease). The purple contours represent boundaries of the coronal hole in the FOV, of which the northwest region is inside coronal hole. The belt between gray lines is a rough dividend of coronal hole and QS. Panels (b) and (c) show two cases of cancellation events in the coronal hole and at coronal hole boundary, respectively. Blue and red contours indicate positive and negative magnetic conponents at ±100 G.

described in the study of [169]. Figure 6.4(b) shows light curves of photospheric magnetic energy evolution. The blue curve represents the total magnetic energy. The magenta curve represents the total magnetic energy stored in the elements that experience flux cancellations, and the red curve shows the cumulative magnetic energy release through flux cancellations. The corresponding magnetic energy release rate is 15.7 ergs cm^{-3} s^{-1}, which is ∼2 times larger than that at the coronal hole boundary. Figure 6.4(c) shows the distribution of net flux at the beginning (blue bar) and end (yellow bar) of magnetic flux cancellations. It shows a tendency of enhancement in the negative polarity after cancellations. The average net flux changes

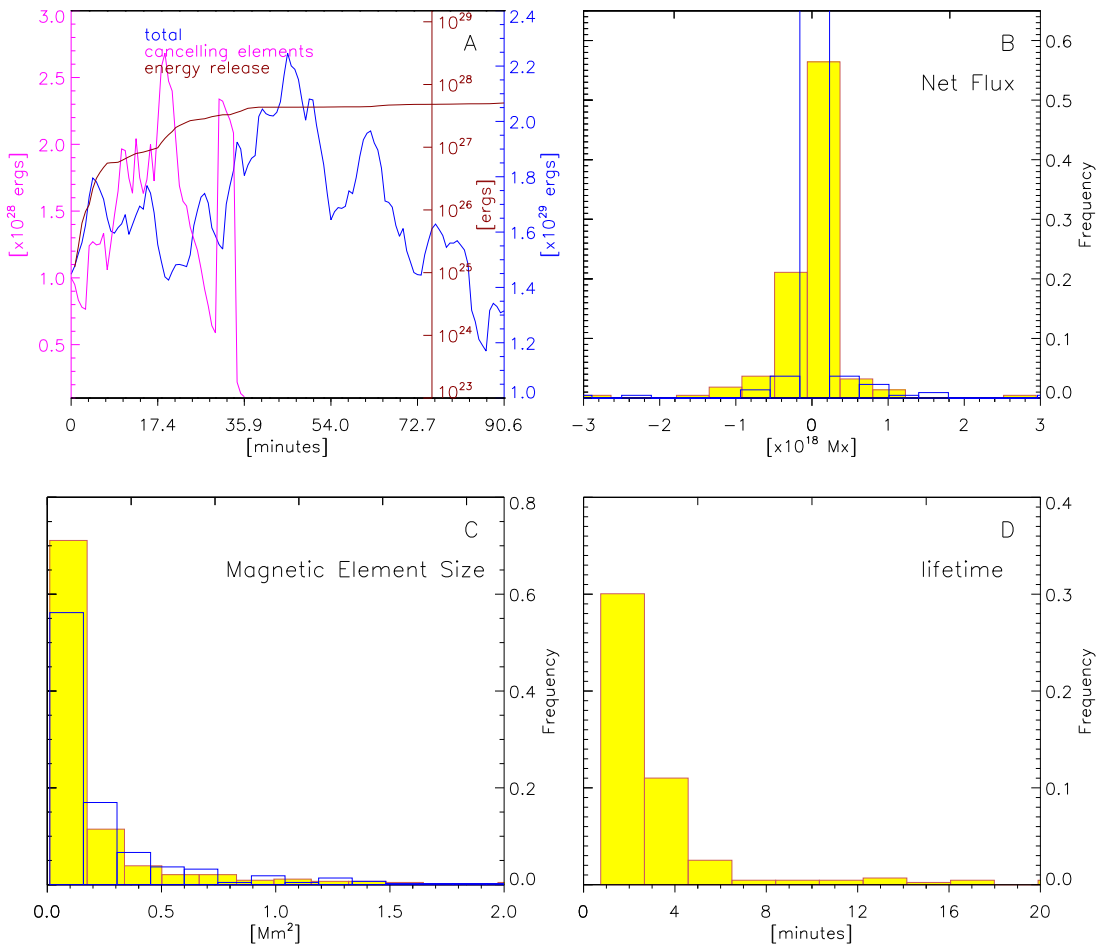

Figure 6.3 Magnetic field properties at coronal hole boundary. Panel (a) show time evolution of total magnetic energy, energy of cancelling magnetic flux, and cumulative released energy through cancellations. Panel (b)-(d) show distribution histograms of net flux, size of cancelling magnetic elements, and lifetime of cancellation events, respectively.

from 4.6×10^{16} Mx before flux cancellations to -2.2×10^{17} Mx afterwards. The size distribution of cancelling magnetic elements is shown in Figure 6.4(d). The mean size is 0.53 Mm^2 (0.39 Mm^2) before (after) flux cancellations. As shown in Figure 6.4(e), 32.5% of the cancellation flux elements have a lifetime shorter than 8 minutes and

the average lifetime is 2.4 minutes. The flux cancellation rate in the coronal hole is 2.0×10^{18} Mx Mm^{-2} hr^{-1}.

Figure 6.5(a) shows the average magnetogram in the quiet Sun region out of the coronal hole. The studied region excludes an area of $\sim$100 Mm^2 outside of the coronal hole centered at about [53″,20″] (see Figure 6.2(a)), as magnetic evolution in this area is not fully covered by NIRIS magnetograms. The average positive and negative longitudinal flux density in the quiet Sun region are 65 G and -160 G, respectively. The artificial dark lines at the lower left corner are due to rotation and shift of the GST's pointing. Enhanced spicular activities are observed to be anchored at edges of strong negative flux concentrations. Figure 6.5(b) shows light curves of photospheric magnetic field changes. The total magnetic energy increases by 1.9×10^{29} ergs in $\sim$20 minutes from +22 minutes of the observation, followed by 30 minutes of magnetic energy dissipation (blue curve). The energy is released through small-scale magnetic flux cancellations at a linear rate of 8.2×10^{26} ergs Mm^{-3} hr^{-1} (red curve). Figure 6.5(c) shows the distribution of net flux before (blue bar) and after (yellow bar) the occurrence of magnetic flux cancellation events. The numbers of positive and negative magnetic elements remained after flux cancellations become balanced, whereas the average net flux changes from 7.8×10^{16} Mx to -1.0×10^{17} Mx. The element size of cancelling magnetic flux shows a similar distribution as that in the coronal hole. The mean size is 0.45 Mm^2 after cancellations. The mean flux size at beginning of cancellations is 0.82 Mm^2. Figure 6.5(d) shows that $\sim$97% of cancellation events occur in 8 minutes. The average lifetime of cancellation events is 3.4 minutes. The flux cancellation rate in the quiet Sun region is 8.8×10^{17} Mx Mm^{-2} hr^{-1}. To calculate the small-scale energy release rate per unit area, we only consider magnetic elements with flux under $\sim10^{19}$ Mx and exclude elements below the noise level. The unit energy release rate is 3.7 ergs cm^{-3} s^{-1}.

In summary, the cancelled magnetic flux in the coronal hole and in the quiet Sun (outside the coronal hole) is 5.4×10^{20} Mx and 2.1×10^{20} Mx, respectively. However, 19.5% of the cancellation events start with emergence of magnetic flux of opposite polarities, which contributes to the increase of net flux. In addition, flux emergence inside the coronal hole has an occurrence rate comparable to that of cancellation events. The net flux of negative polarity increases 9.7×10^{19} Mx in 30 minutes.

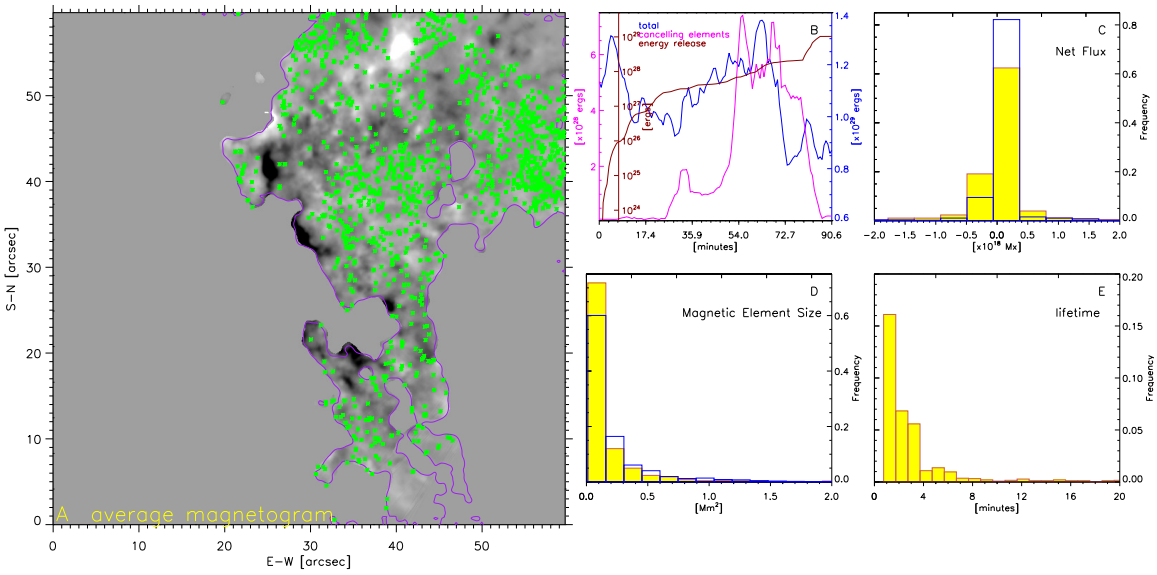

Figure 6.4 Magnetic field properties in coronal hole. Panel (a) show the magnetic field in coronal hole with cancellation site indicated by green star symbols. Grayscale of the magnetogram is in range of -400 G to 200 G. Panel (b) show time profile of total magnetic energy, energy of cancelling magnetic flux, and released energy through cancellation. Panel (c)-(e) show distribution histograms of net flux, size of cancelling magnetic elements, and lifetime of cancellation events, respectively. Blue box in panel (c) show net flux distribution before before cancellation of each event.

6.3.3 Hα Ejections Associated with Magnetic Cancellations

Hα spicules in the observation are mainly located at the coronal hole boundary, where there is the unipolar negative magnetic cluster. We observe recurrent spicular activities seemingly stemming from this negative magnetic network as shown in Figure 6.1. The spicules observed in Doppler signals are mostly rooted at edges of the strong

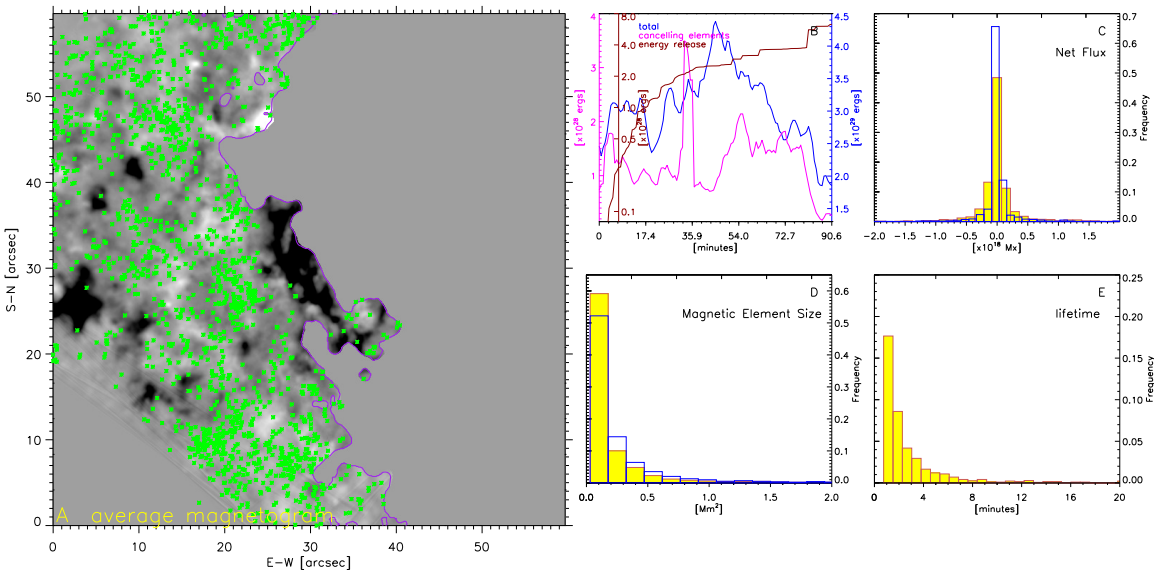

Figure 6.5 Magnetic field properties outside coronal hole. Panel (a) show the magnetic field in the QS with cancellation site indicated by green star symbols. Panel (b) show time profile of total magnetic energy, energy of cancelling magnetic flux, and released energy through cancellation. Panel (c)-(e) show distribution histograms of net flux, size of cancelling magnetic elements, and lifetime of cancellation events, respectively.

negative magnetic concentrations with weak ambient positive fields. Previous studies found a close connection between spicules and opposite-polarity magnetic fluxes. We use Doppler signals from Hα +/− 1.0 Å images to locate eruptive spicules, in which positive values of Doppler signals indicate Hα upflows. During the magnetic flux emergence phase, small brightening loops are observed at the coronal hole boundary, which indicates chromospheric heating due to magnetic reconnection. In this section we present details of magnetic evolution associated with jetlet eruptions and spicular activities.

Figure 6.6(a) and (b) show Hα eruptions in event 1 at the western footpoints of EUV brightening loops along the coronal hole boundary. At 16:42:33 UT (+8.28 minutes), two strands of Hα spicules rooted between the opposite polarities, which later erupt in opposite directions, are observed to be cospatial with the brightening. Both spicules are elongated across the adjacent opposite polarities. About 1.4

minutes later, an arched Hα dark material (indicated by yellow arrow) is formed between the roots of the two spicules, with a faint spire (indicated by red arrow) extending southwest. This resembles coronal hole jets depicted by [150], except that the presented events are on a much smaller scale. At the same time, both of the preexisting spicules pointing opposite directions experience eruptions sequentially from north to south. As seen in Figure 6.6(c), the photospheric magnetograms show positive magnetic elements surrounded by the semi-circular negative network field where the spicules are rooted. A small segment of negative magnetic element separates from the network field and converges with the positive magnetic element. Figure 6.7 shows the evolution of the average positive (negative) magnetic flux of the converging elements in blue (red) curve. The black and red vertical dashed lines mark the times of formation of the arched Hα dark feature and onset of the Hα eruptions, respectively. The light curves show that the positive magnetic flux enhances until the onset of the eruption of the north-pointed spicule, then decreases from $3.9\pm0.5\times10^{18}$ Mx to $2.5\pm0.4\times10^{18}$ Mx in $\sim$3.4 minutes. The rapid decrease of negative flux occurs 2 minutes before the decrease of positive flux and is cotemporal with the formation of arched Hα dark material. The uncertainty of magnetic flux measurement is estimated by calculating the unsigned flux density in a region away from strong network magnetic fields and then multiply it with the measured element size of converging magnetic polarities. The AIA images at 171 Å in Figure 6.6(d) show that EUV brightenings appear at the edge of the negative magnetic polarity (centered at [5″, 2.5″]) when the two spicules become noticeable. Then the brightenings associated with eruptions roughly evolve northward along the spicules. The transverse speed is $\sim$18 km s^{-1}. The chromospheric counterparts of the magnetic reconnection are seen to continue moving northward and later, a small loop brightening is observed at 16:51:41 UT (+17.4 minutes).

Figure 6.8 and shows the magnetic evolution and Hα activities at the east footpoint of the small EUV loop. As seen in Hα images (Figure 6.8(b)), there are multiple strands of recurrent spicules rooted at the Hα bright points, which correspond to network edges in magnetograms (see Figure 6.8(c)). At 16:45:21 UT (+11.05 minutes), the enhanced positive magnetic element starts to merge with the strong negative network field, which is cotemporal with Hα eruptions in event 1. At 17:08:04 UT (+33.8 minutes), enhanced spicular activities are observed to accompany the magnetic cancellation of opposite polarities. Upflow motion of the spicular activities is detected in the Hα Doppler maps (see Figure 6.8(a)). Such enhancement of Hα spicules is similar to the spicular activity observed by [169]. AIA images in Figure 6.8(d) show an EUV brightening at roots of the enhanced spicules. However, along the spicular spires no EUV reponse is observed. Figure 6.9 shows the temporal evolution of magnetic flux of the adjacent opposite magnetic polarities, where Hα spicules are rooted as indicated by the dashed box. The negative magnetic elements that cancel with the positive magnetic elements are at the edge of the unipolar clustered negative field, which also has cancellations in other edge locations. We only measure negative flux in the dashed box to avoid impact from other magnetic evolution. As shown in the light curves, both positive and negative fluxes have a quasi-periodic oscillation of 10.8 minutes and 7.5 minutes, respectively, with damped peak values. After screening out flux changes due to the oscillation by integrating over each period, the average positve (negative) flux dereases 0.96×10^{18} Mx (1.22×10^{18} Mx). The positive flux starts to decrease at 17:08:04 UT (+33.8 minutes), when the enhanced spicular activity is observed and the flux evolution no longer exhibits oscillations. The negative flux decreases by 11.2×10^{18} Mx from 17:14:35–17:23:58 UT. Despite that spicules continuously appear in the network edge, the enhancement and upflow motion of the spicules are only observed to last $\sim$2 minutes from 17:06:37 UT.

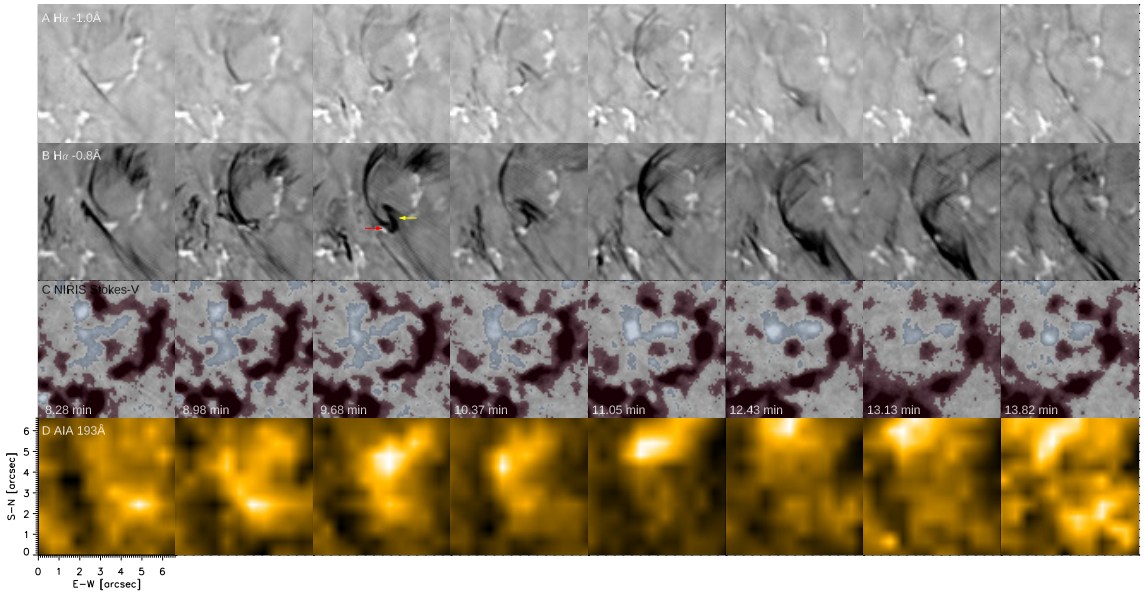

Figure 6.6 Magnetograms and Hα images of the evolution of cancellation event 1. Panels (a)–(d) show Hα images (-1.0, -0.8 Å), magnetograms, and AIA 193 Å images of the small-scale cancellation associated with jetlet eruptions from location in Figure 6.2(c). Yellow and red arrows in third frame of panel (b) indicate base and spire of the jetlet, respectively. Blue and red in panel (c) represent positive and negative polarities above 200 G of field strength.

6.4 Discussion

With the high-resolution GST observations, we study small-scale magnetic transients and corresponding chromospheric Hα eruptions near a coronal hole boundary on the quiet Sun region. The study particularly focuses on statistical magnetic properties of the small-scale flux cancellations in and outside the coronal hole, as well as correspondence between Hα spicules and underlying magnetic evolution. Based on the magnetic analysis by using automatic magnetic feature tracking method (SWAMIS), main results in this work are summarized as follow:

1. During the magnetic energy release process in the small-scale magnetic flux cancellation events, there is a tendency to reduce the magnetic flux of both positive and negative polarities and reinforce the dominance of negative polarity inside the coronal hole. The vertical magnetic flux decreases on the order of 10^{18} Mx Mm^{-2} hr^{-1}, which is consistent with the flux cancellation rate in the quiet Sun intranetwork.

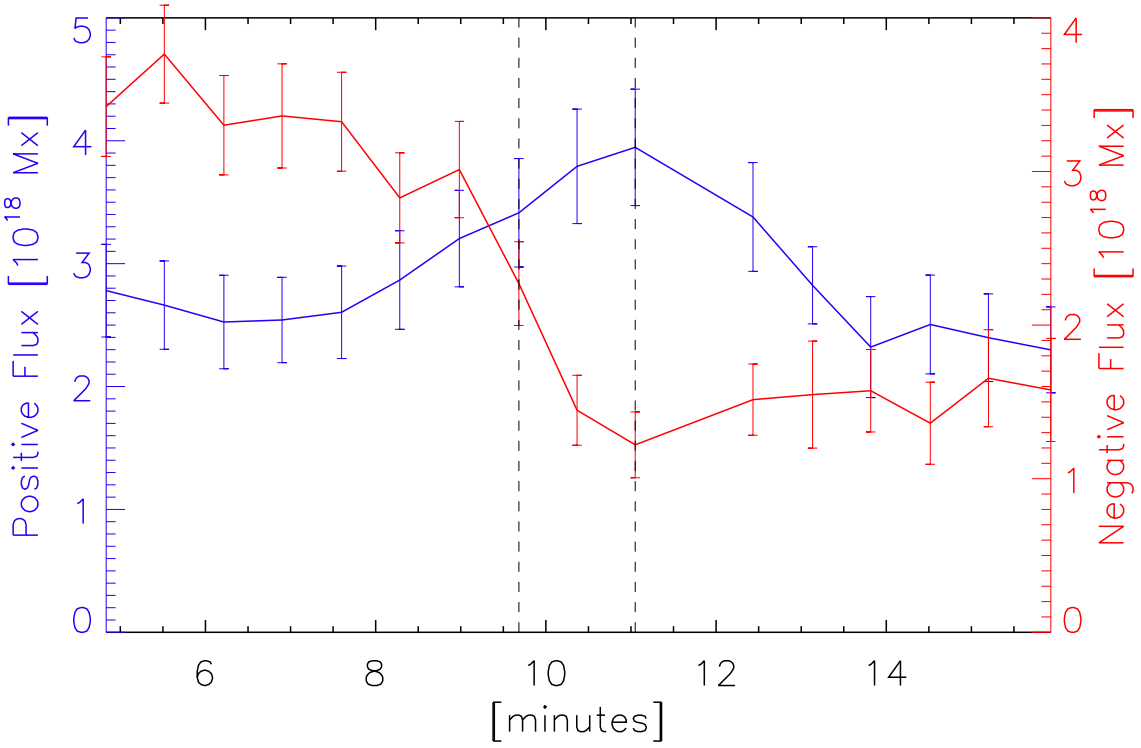

Figure 6.7 Time evolution of vertical flux of event 1. The temporal evolution from 16:39:08–16:50:14 UT of converging positive (negative) magnetic flux in the Figure 6.6 is displayed in blue (red) curve. The black and red vertical dashed lines represent formation of arched Hα dark feature and onset of the Hα eruptions, respectively. Error bars of each curve represent uncertainty of measured magnetic flux from noise of magnetograms.

2. Despite a comparable occurrence rate in the coronal hole (1.5 Mm^{-2} hr^{-1}) and the surrounding quiet Sun region (1.2 Mm^{-2} hr^{-1}), contribution of energy release through small-scale magnetic flux cancellations in the coronal hole is $\sim$3.7 higher than outside the coronal hole (0.7×10^{29} $ergs$).

3. Magnetic reconnection could terminate the periodic oscillation and initiate small-scale Hα ejections. Most of the enhancement of spicules are associated with small-scale magnetic flux cancellations.

4. The EUV responses of enhancement of spicule events show rare (7 of 88 enhanced spicules) but close connection between the base brightening and small-scale reconnection site.

In the coronal hole boundary region defined in Section 6.3.1, 36 cancellation events that are associated with Hα eruptions occur between the unipolar negative field and ambient positive magnetic elements prior to 17:23:58 UT (+49.7 minutes),

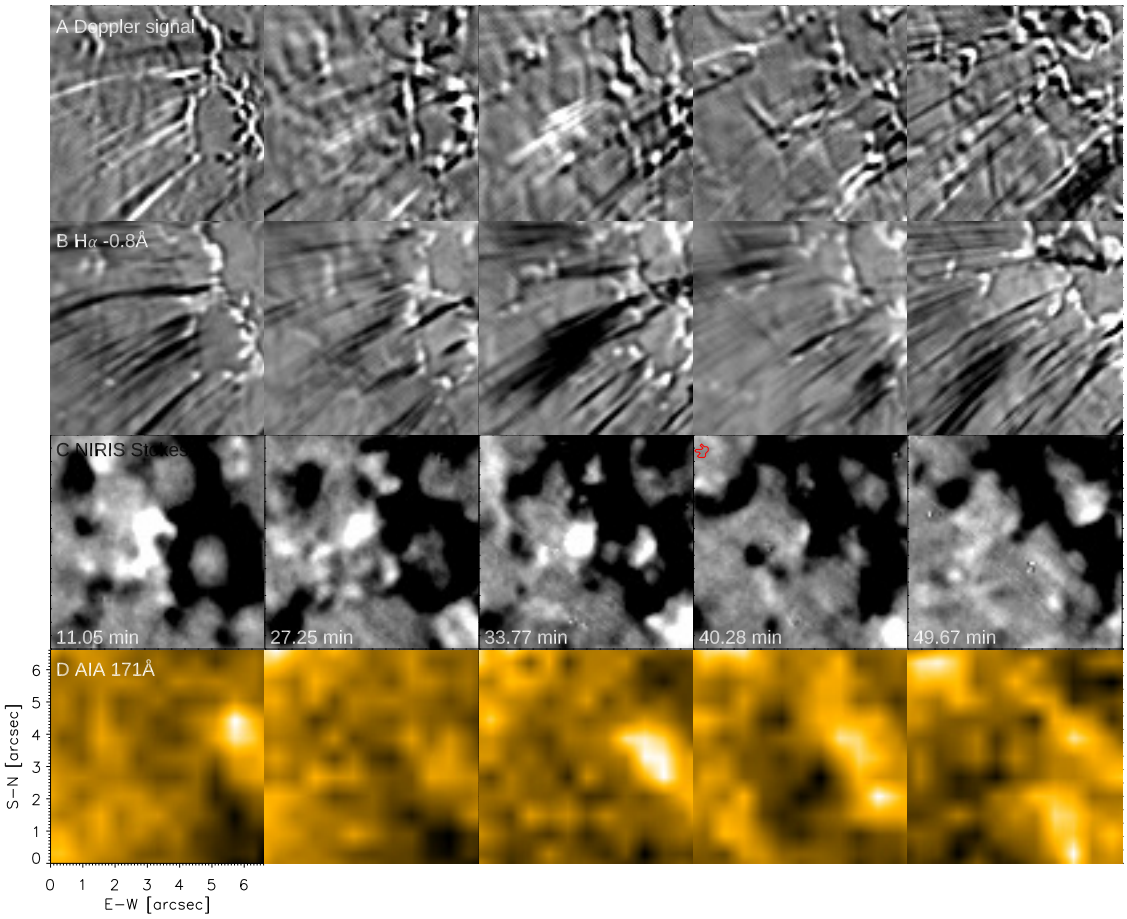

Figure 6.8 Magnetograms and Hα images of the evolution of cancellation event 2. Panels (a)–(d) show Hα images (-1.0, -0.8 Å), magnetograms, and AIA 193 Å images of the small-scale cancellation associated with Hα spicular activities from location in Figure 6.2(b). Blue and red in panel (c) represent positive and negative polarities above 200 G of field strength.

and 31 cancellation events occur afterward. The total magnetic flux in the coronal hole boundary region enhances in the first ∼50 minutes of observation, and then decreases with ∼15 minutes oscillations. Similarly, the individual spicular activities associated with magnetic cancellations in event 2 display quasi-periodic oscillations in magnetic flux evolution. Before the prominent upward motion of the enhanced Hα spicules, 60% of flux change in the positive polarity comes from oscillatory flux variation within one period, and 40% is due to continuous flux decrease between

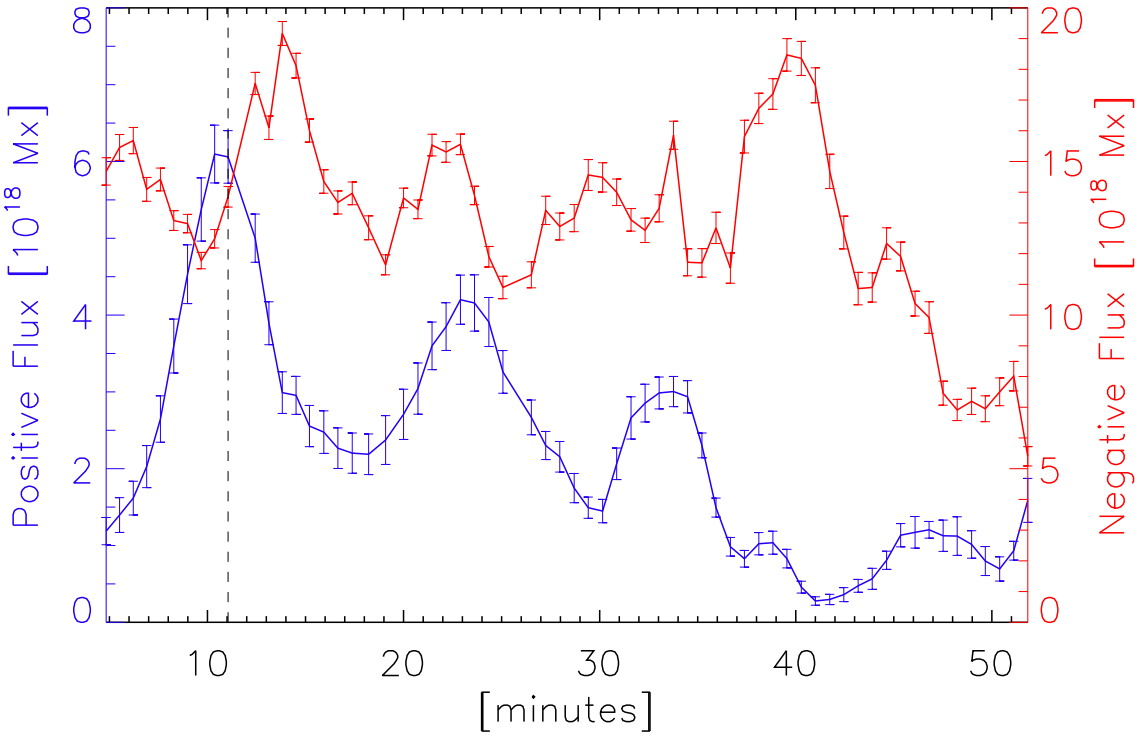

Figure 6.9 Time evolution of vertical flux of event 2. The temporal evolution from 16:39:08–17:26:08 UT of positive (negative) magnetic flux in the Figure 6.8 is displayed in blue (red) curve. The black vertical dashed lines represent onset of the Hα eruptions as seen in event 1. Error bars of each curve represent uncertainty of measured magnetic flux from noise of magnetograms.

consecutive periods. In the negative polarity, oscillatory flux change is ∼4 times as much as continuous flux decrease (1.22×10^{18} Mx) over periods. However, the dynamic spicular activity is only associated with magnetic flux cancellation of the converging opposite polarities.

We inspected other cancellation events at the unipolar magnetic field, and found that the ∼5–10 minutes magnetic flux oscillation is universal in the cancellation sites at the coronal hole boundary. In 34 the cancellation events, such quasi-periodic flux variation is damped out shortly after spicule enhancement, usually with one period. This result indicates that the spicules in the coronal hole boundary network are triggered by both Alfvén waves of p-mode oscillations and small-scale magnetic flux cancellations. Specifically, the recurrent spicules are more likely to be triggered by

Alfvén waves [42], and the enhanced spicules are more likely generated by magnetic flux cancellation. We speculate that after flux cancellation the upward spicular motion carries plasma to upper atmosphere and the local pressure perturbation is no longer sustained, which temporarily terminates magnetic flux oscillation.

In the relatively weak field regions in and outside the coronal hole, magnetic flux evolution of the cancellation events (including event 1) associated with Hα eruptions do not show obvious periodic variations. In the event 1, the Hα eruption is triggered by magnetic flux cancellation while both the positive and negative fluxes continue to emerge. The formed arched dark feature in Hα images is likely due to magnetic reconnection between the two parallel dipoles. We interpret the scenario as follows. When the negative field of the north-pointing spicule merges with the positive field of the south-pointing spicule, the two spicule fields reconnect at the merging opposite polarities and the plasma is temporarily wrapped in the newly formed field. Then it experiences a microfilament eruption as proposed by [190]. The loop brightening in EUV images (AIA 171 and 193 Å) becomes visible $\sim$4 minutes after the microfilament eruption, and continues to enhance with flux emergence at the loop footpoints. This temporal evolution indicates that the erupted plasma with an upward propagation speed below 20 km s^{-1} may play a role in the chromospheric heating. The occurrence rate of magnetic flux cancellation events in and outside the coronal hole is comparable, while fewer eruptive Hα spicules (6 spicule enhancements) are observed in the coronal hole than outside the coronal hole (15 spicule enhancements). This could be due to the fact that the vertical field topology in the chromosphere makes the Hα spicule in the coronal hole less detectable.

In the total 88 enhanced spicules observed in the FOV, there are three events originate from center of the unipolar magnetic elements without cancellation detected associated with the spicular enhancement. Other spicule events exhibit close temporal and spatial correlation with flux cancellation between their underlying magnetic

elements and adjacent magnetic elements of opposite polarities. However, the magnetic cancellation detected by SWAMIS demonstrates ubiquitous characteristics of the small-scale reconnection, which has exceedingly high occurrence rate (3127 events in ∼90 minutes). Total magnetic energy released through magnetic cancellation in the FOV is 3.3×10^{29} $ergs$, of which 2.6×10^{29} $ergs$ and 0.7×10^{29} $ergs$ corresponds to the events in the coronal hole and outside the coronal hole, respectively. In EUV observations, hot plasma is seen to be ejected to upper atmosphere with enhancement of spicules. Seven events are associated with EUV brightening (as seen in AIA 171 Å) at base of the enhanced spicules. Particularly, with dim background of AIA 171 Å in the coronal hole, a faint spire becomes visible extending from the bright base in event 1 about 3 minutes after the spicule eruption. Observation of such jetlike feature support the microfilament eruption model of spicules [193].

CHAPTER 7

SUMMARY OF THE DISSERTATION

The work presented in this dissertation focuses on the photospheric magnetic structures associated with solar activities. The mystery of evolution of magnetic structures and their relation to energy storage and release is addressed from two aspects: (1) the rapid and permanent photospheric structural and magnetic changes in response to solar flares, and (2) the connectivity between small-scale magnetic transients in the photosphere and energy release and heating of upper atmosphere. The relations between solar flares and complexity of magnetic field were previously considered to be only coronal interaction and do not alter photosphere due to the line-tying effect in high plasma-β photosphere. Since the first photospheric magnetograph observations of rapid change of vector magnetic field in the flaring region over two decades ago [224, 227], substantial amounts of effort have been put to the study of photospheric magnetic field in solar flares. Particularly, the transverse field change due to flare eruptions is interpreted as driven by vertical Lorentz force change in the photosphere. The fundamental process of magnetic energy build-up is flux emergence, which varies widely in size. On small scale, such emergent magnetic flux can cause ejecting features such as EBs and spicules through reconnection. Using unique high-resolution GST observations in multiple wavelengths, the research investigated flow fields change and evolution of magnetic fields in the flaring core region of the well-captured M6.5 flare by GST, events of small-scale magnetic flux emergence in a flare productive AR, and statistical properties of magnetic transients around a coronal hole. Key findings of these observational studies are summarized in the following sections.

7.1 Flow and Magnetic Field Change Associated with the M6.5 Flare

7.1.1 Flow Field Near the PIL of Flaring δ-region

Chapter 3 presents a detailed study of the structural evolution of penumbra and shear flows near the PIL of the δ-region associated with the 2015 June 22 M6.5 flare in NOAA AR 12371, using high-resolution imaging observation in the TiO band taken by the 1.6 m GST at BBSO. The penumbral flow field is tracked with aid of the differential affine velocity estimator method. The accompanied photospheric vector magnetic field changes are also analyzed using data from the Helioseismic and Magnetic Imager. The main results are summarized as follows.

1. The central penumbra lying near the PIL of the flaring δ-region experiences distinct growth following the signal of flare onset in HXR, which is accompanied with step-like increase of horizontal field. The entire penumbral region becomes more pronounced as seen in continuum image and in the horizontal flow field.
2. Close the the PIL of the flaring core region, enhancing shear motion is revealed next to the flare precursor with high-resolution spectroscopic observation and expands significantly after the flare.

Notably, high-resolution data used for the flow tracking results in higher flow velocity comparing to previous studies [202]. The evidence against previous claim that the central penumbra darkens after flares favors the back reaction theory, in which the central field across the PIL turns inclined.

7.1.2 Magnetic Field Change in the Flaring Region

In Chapter 4, the relationship between the dynamics of flare ribbons in the chromosphere and variations of magnetic fields in the underlying photosphere is explored, using high-resolution off-band Hα images and near-infrared vector magnetograms of the M6.5 flare on 2015 June 22 observed with the 1.6 m Goode Solar Telescope. The results show that changes of photospheric fields occur at the arrival of the flare ribbon front, thus propagating analogously to flare ribbons. The 3D coronal restructuring

is also explored with aid from the NLFFF modeling based on SDO/HMI vector magnetograms. Major findings are summarized as follows.

1. Horizontal field increases with flare occurrence in the photosphere and its correlation with flare ribbon motion is exhibited by propagation of horizontal field enhancement. The strengthening of horizontal field at the arrival of the flare ribbon front is accompanied by an increase of inclination angle. The nonpotentiality is increased with the permanent surface magnetic field changes.

2. At the locations where azimuth angle sharply decreases indicating the sudden sunspot rotation, B_h and inclination angle decrease transiently before being enhanced. Particularly, the flare ribbon decelerates toward the sunspot rotation center where B_z becomes greatly intensified.

3. In the corona, a downward collapse of coronal magnetic field by $\sim 3''$ toward the photosphere is clearly portrayed by the evolution of the vertical profiles of J_h around the PIL [200, 118, 117], which changes from a vertically elongated source to an enhanced, horizontally elongated source close to the surface (Figure 4.5). Correspondingly, above the PIL and flare ribbon regions, magnetic field becomes more inclined, which is consistent with the observed enhancement of B_h. We surmise that a successive turning of field vectors associated with the flare ribbon motion might be visualized given coronal field models with a sufficiently high resolution.

In general, the horizontal field increases and the field lines become more inclined to the surface. When ribbons sweep through regions that undergo a rotational motion, the fields transiently turn more vertical with decreased horizontal field and inclination angle, and then restore and/or become more horizontal than before the ribbon arrival. The ribbon propagation decelerates near the sunspot rotation center, where the vertical field becomes permanently enhanced. Similar magnetic field changes are discernible in magnetograms from the HMI, and an inward collapse of coronal magnetic fields is inferred from the time sequence of non-linear force-free field models extrapolated from HMI magnetograms. We conclude that photospheric fields respond nearly instantaneously to magnetic reconnection in the corona.

7.2 Small-scale Flux Emergence

In Chapter 5, taking advantage of the high resolution of the 1.6 m Goode Solar Telescope, we jointly analyze vector magnetic fields, continuum images, and Hα observations of NOAA AR 12665 on 2017 July 13, with the goal of understanding the signatures of small-scale flux emergence, as well as their atmospheric responses as they emerge through multiple heights in photosphere and chromosphere. The study is particularly focused on magnetic characteristics of two different kinds of flux emergence. Main results are summarized as follows.

1. In typical sheet emergence case, an organized mantle structure of enhancing horizontal magnetic flux is seen to span over an entire granule. The magnitude of the horizontal field in the flux sheet increases with emerged flux at footpoints reaches order of 10^{18} Mx. In a subsequent stage of the emergence, the mantle structure is not maintained as the granulation topology is broken via movement of the flux footpoints

2. In typical loop emergence case, magnetic footpoints at the two ends (the concentrated opposite-polarity flux component) emerge and move in the intergranular lanes with a separation speed of 1.2–1.7 km s^{-1}; meanwhile, a horizontal field lying in-between enhances, forming elongated, loop-like structures (the central diffused component).

3. Analysis of extended samples shows that all the eight events have a strongly emerged horizontal field. Horizontal field is comparable with vertical field in flux sheets, while it is 30% less than vertical field in magnetic loops. The concentration of field strength in the granule boundaries at the late phase of the emergence is observed in both horizontal and vertical magnetograms.

7.3 Small-scale Magnetic Transients Near the Coronal Hole

In Chapter 6, we analyze high-resolution magnetograms and Hα off-band images taken by the 1.6 m GST to investigate the magnetic properties in association with small-scale ejections in a coronal hole boundary region from a statistical perspective. With one hour of continuous high-resolution observations in excellent seeing, we focus on the magnetic structure and evolution at the coronal hole boundary and track the magnetic features with the SWAMIS. The magnetic field at the studied coronal hole

boundary is dominated by negative polarity with magnetic flux cancellations observed at edges of the negative unipolar cluster. Main findings in this chapter are summarized as follow.

1. During the magnetic energy release process in small-scale magnetic flux cancellation events, there is a tendency to reduce the magnetic flux of both positive and negative polarities and reinforce the dominance of negative polarity in the coronal hole regions.
2. Magnetic reconnection could terminate the periodic oscillation and initiate small-scale Hα ejections. Most of the enhancement of spicules are associated with small-scale magnetic flux cancellations.
3. Statistical study of ubiquitously small-scale reconnections indicates a higher energy release rate in the coronal hole while only small portion of the release magnetic energy directly deposit to hot plasma.

7.4 Future Perspectives

With the accumulation of high-resolution solar observations, investigation of physical properties regarding solar activities can be addressed from both case studies and statistical analysis. The potential future work extended from this dissertation is outlined below.

Parker Solar Probe (PSP) has obtained outstanding initial results (e.g., [168, 145, 138, 266, 266, 262]). One of the major discoveries is an abundance of small transients in the solar wind in the form of intermittent magnetic, velocity and plasma structures [63, 264, 59]. These are revealed as magnetic switchbacks, velocity spikes and low-energy SEPs in the solar wind, and fine-scale structures in the K-corona. The sources of these transients are still unclear, but possible drivers are small scale magnetic reconnections and associated ejections/eruptions in the lower solar atmosphere [192]. The key science question to be addressed is: what are the origins of these and other dynamic structures seen by PSP? A comprehensive observational and modeling effort can be carried out to understand the transport of small-scale ejections from the low atmosphere, to the corona, and

through the coronal/heliospheric boundary. Key candidates for such events include macro-spicules, coronal jets and mini-filament eruptions.

The above goal can be achieved by combining state-of-the art magnetic field and photospheric/chromospheric imaging observations from BBSO/GST, the 1.5-m GREGOR telescope [221] and 0.7-m Vacuum Tower Telescope (VTT; [214]) on the Canary Islands, and the 4-m Daniel K. Inouye Solar Telescope (DKIST; [38]), together with IRIS[43] UV spectroscopy of the transition region, microwave multi-frequency imaging from the Expanded Owens Valley Solar Array (EOVSA; [66]), Global Halpha Network (GHN), SDO/AIA[111], Hinode[91], SOHO/LASCO[183] and STEREO/SECCHI[86] coronal observations. Such broad data sets will provide thermal/non-thermal diagnostics in the solar corona to be correlated with disturbances in the solar wind as observed by PSP. Solar Orbiter will provide additional unique observations. This suite of instruments can be used to study the characteristics of transients observed in the solar atmosphere. PSP and other observational teams can be coordinated to identify the likely source region(s) on the solar surface prior to, during, and after each perihelion passage of PSP. Targeted observations of that region, using mosaicking if necessary to cover the entire target region, can be obtained. The resulted observations can be analyzed using manual and automated feature recognition techniques to identify energetic reconnection events and small-scale ejections. The analysis will be enhanced by modeling, both near the solar surface and into corona/heliospheric boundary.

Working with the PSP science teams, the fine structure in the solar wind, such as velocity spikes, magnetic field switchbacks (FIELDS; [12], SWEAP; [102]), K-corona density fluctuations (WISPR; [222]) and lower energy SEPs (ISOIS; [134]) can be correlated with our detailed observations of the source region. To further the research achieved in the this dissertation, a statistical analysis based on the high-resolution observation can be performed to compare the occurrence rate, duration and kinetic

of small-scale energy release in potential source regions with similar measurements in the inner solar wind. For selected larger events, in-depth analysis can be performed to trace their initiation and propagation from the solar atmosphere to the inner heliosphere.

On the other hand, Understanding what initiates and drives solar eruptions belongs to the highest priority goals in solar and heliospheric physics. The currently debated categories of ideal MHD instability and reconnection models under the energy storage-and-release paradigm correspond, respectively, to the assumptions of flux rope and sheared arcade as the magnetic structure at the onset of the main-acceleration phase. Although it is clear that a flux rope is ultimately created, it remains to be clarified whether the onset is dominated by the torus instability, reconnection, or a coupled state of both processes. There are different simulations developed with the attempt to uncover physics nature of the flare onset and eruption process, such as non-linear-force free and non-force-free modeling in the data-driven MHD simulations (e.g., [252, 87]). With the highest resolution magnetic field observation available, the accomplished work in this dissertation reveals critical quantities in magnetic and flow fields during the flare eruption. Such results of advanced data could be implemented as the initial/boundary conditions in future data-based magnetic field extrapolations and MHD modeling, especially the unprecedented flow field quantities could provide more accurate parameters in photospheric dynamics. Furthermore, combining the high-resolution NIRIS magnetic field products in the flare core regions with SDO/HMI observations in the outer flaring region, a more comprehensive understanding of the flare related magnetic field evolution can be derived from the MHD simulations.

APPENDIX A

SUPPLEMENTARY FIGURES FOR VECTOR MAGNETIC FIELD ANALYSIS

As a validation of GST/NIRIS data processing procedures, in Figure A.1 we compare vector magnetograms of NOAA AR 12371 from NIRIS and SDO/HMI obtained at about the same time right before the 2015 June 22 M6.5 flare. The HMI data used is the full-disk vector magnetic field product (`hmi.B_720s`), processed using standard procedures in SSW. It is clear that for the flare core region (white box in Figures A.1(a) and (b)), both B_z and B_h field vectors derived from NIRIS and HMI measurements have a high correlation (see Figures A.1(c)–(f)). The slope of $\sim$0.8 shown by the scatter plots indicates that NIRIS tends to produce stronger fields, presumably due to the fact that NIRIS observes at a deeper atmosphere than HMI.

In Figure A.2, we present 1564.8 nm Stokes profiles at P2b before and after the arrival of the flare ribbon, at 17:34:03 UT and 18:04:34 UT, respectively. Comparing the results, we see that the Stokes I component shows no clear and systematic changes (Figure A.2(a)), suggesting that flare heating does not alter the spectral line profiles. In contrast, the Stokes QU combination $(Q^2+U^2)^{1/2}$ that measures the overall linear polarization magnitude (e.g., [110, 50]) obviously weakens (Figure A.2(b)), while the Stokes V component representing the circular polarization enhances (see Figure A.2(c) and note the difference profile in orange). As this AR is close to the disk center at the time of the M6.5 flare, these changes of Stokes QUV profiles are consistent with the observed decrease (increase) of the horizontal (vertical) field at this location, as presented in Figure 4.3 (third column).

The presented analyses applied to NIRIS data were also carried out using HMI vector magnetograms, and generally similar results were obtained. In Figure A.3, we

show the time-distance maps along the slits S1–S4 based on the 135 s cadence HMI data. The results, despite of having a lower resolution, show evolutionary patterns that are almost identical to those obtained using the NIRIS data (see Figure 4.2).

In Figure A.4(a), an Hα + 1.0 Å image is blended with the derived map of slog$Q$, which is defined as slog$Q$ = sign(B_z)log$_{10}Q$ [208]. The calculation was conducted based on the potential field within the same box volume as the NLFFF, with the code developed by Liu et al.[124].

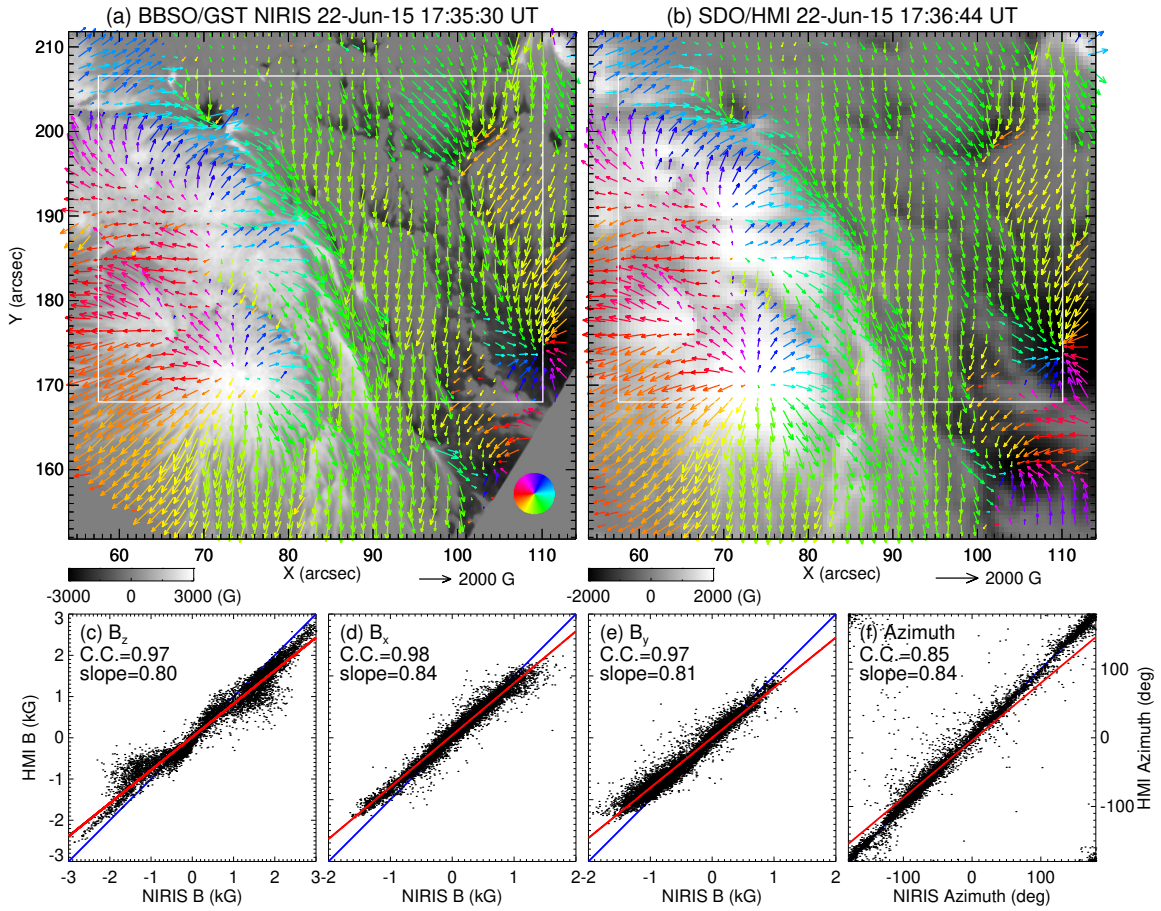

Figure A.1 Comparison between BBSO/GST NIRIS and SDO/HMI vector magnetograms of NOAA AR 12371. The data were taken at about the same time and processed in a similar fashion (Stokes inversion, azimuth disambiguation, and deprojection; see text for details). (a)–(b) Images of B_z superimposed with arrows (color-coded by direction; see the color wheel) representing vectors of B_h. (c)–(f) Scatter plots of NIRIS vs. HMI measurements of B_z, B_x, B_y, and azimuth angle for the boxed region marked in the upper panels (the higher resolution NIRIS images are downsampled by a factor of 6.4). Also indicated are the linear Pearson correlation coefficient (C.C.) and slope of linear fit of the data points (red lines). The underlying blue lines have a slope of 1.

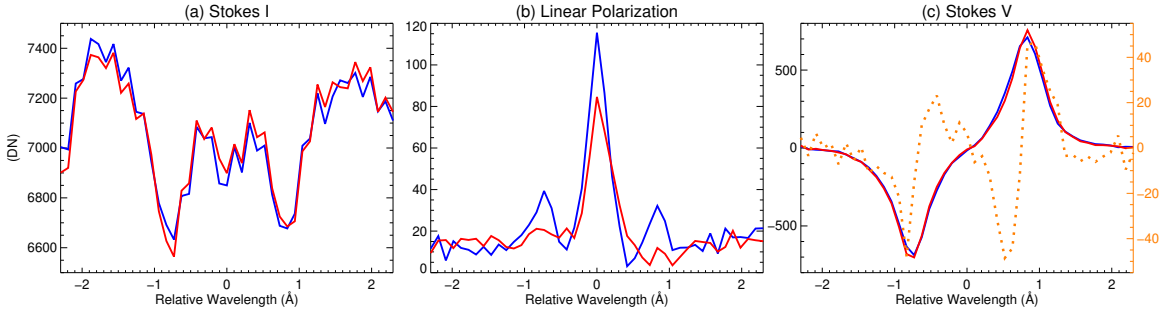

Figure A.2 Changes of 1564.8 nm Stokes profiles at P2b associated with the arrival of flare ribbon. The profiles of Stokes I (a), overall linear polarization magnitude $(Q^2 + U^2)^{1/2}$ (b), and Stokes V (c) at 17:34:03 UT (blue) and 18:04:34 UT (red) are plotted. In (c), the orange dotted line shows the difference profile (the profile at 18:04:34 UT is subtracted by that at 17:34:03 UT).

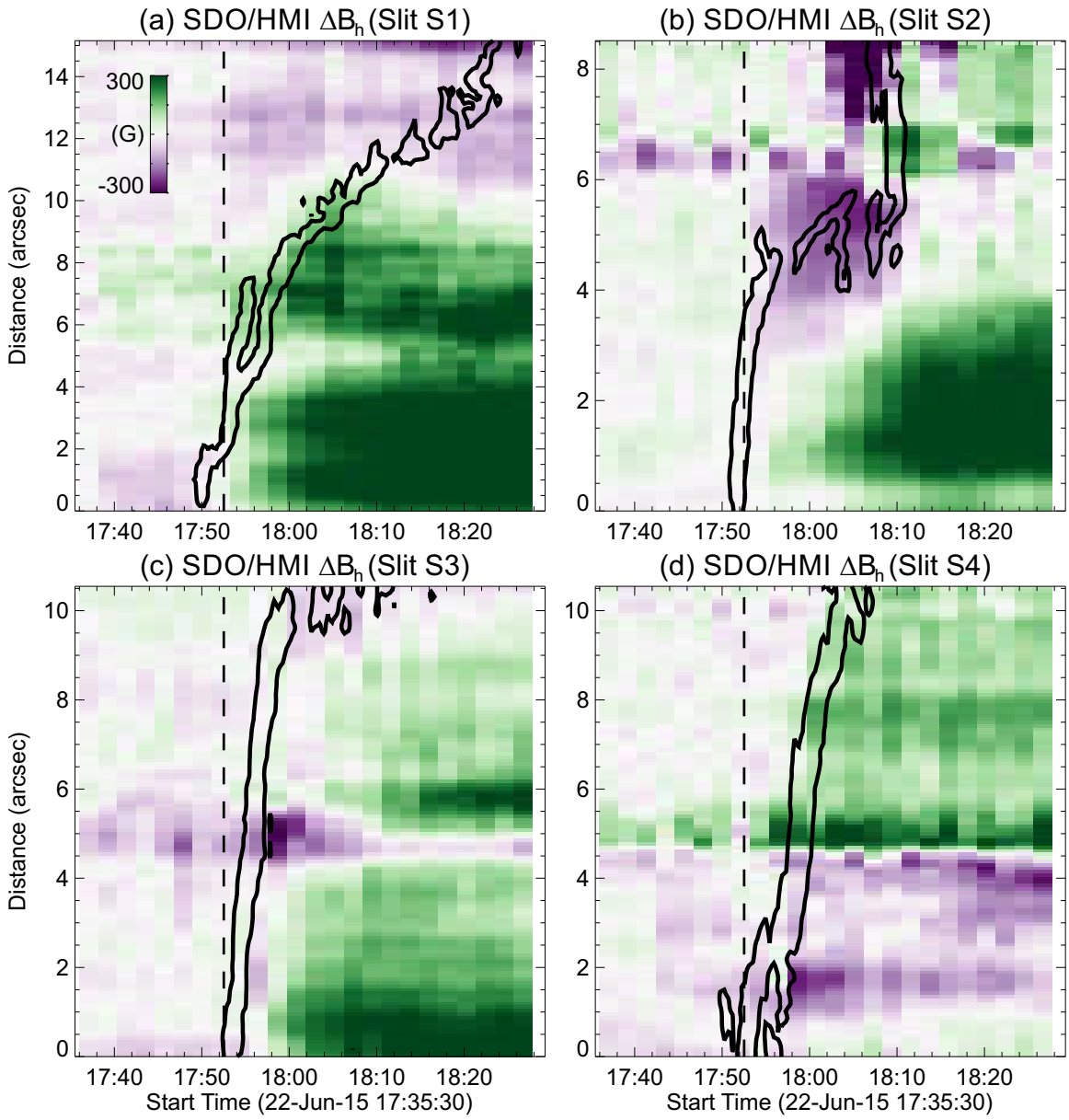

Figure A.3 Same as Figure 4.2 but the background shows time slices for the slits S1–S4 using the fixed difference images of SDO/HMI B_h.

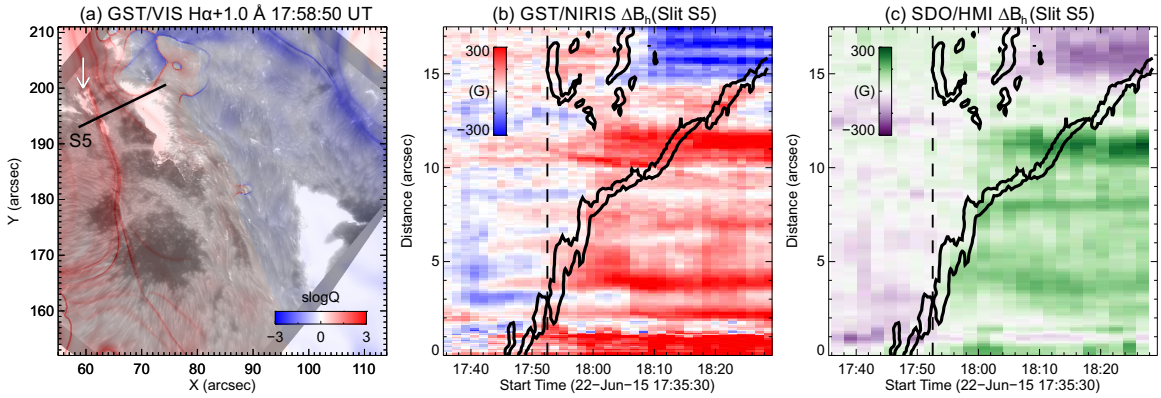

Figure A.4 Evolution of flare ribbon and magnetic field. (a) Hα + 1.0 Å image near the flare peak blended with the slog$Q$ map calculated at a preflare time at 17:36:44 UT, showing that in front of the major eastern flare ribbon, there is elongated emission as pointed to by the white arrow that is located at the high-Q line. Panels (b) and (c) are similar to those shown in Figures 4.2 and A.3, respectively, but for the slit S5 marked in (a).

REFERENCES

[1] M. Adams, A. C. Sterling, R. L. Moore, and G. A Gary. A Small-scale Eruption Leading to a Blowout Macrospicule Jet in an On-disk Coronal Hole. *The Astrophysical Journal*, 783(1):11, March 2014.

[2] K. Ahn and W. Cao. Data processing pipeline of the Near-Infrared Imaging Spectropolarimeter at the NST. *AAS/Solar Physics Division Meeting*, 48:115.04, August 2017.

[3] K. Ahn, W. Cao, S. Shumko, and J. Chae. Data Processing of the magnetograms for the Near InfraRed Imaging Spectropolarimeter at Big Bear Solar Observatory. *AAS/Solar Physics Division Meeting*, 47:2.07, May 2016.

[4] C. E. Alissandrakis. On the computation of constant alpha force-free magnetic field. *Astronomy & Astrophysics*, 100(1):197–200, July 1981.

[5] J. D. Alvarado-Gómez, J. C. Buitrago-Casas, J. C. Martínez-Oliveros, C. Lindsey, H. Hudson, and B. Calvo-Mozo. Magneto-Acoustic Energetics Study of the Seismically Active Flare of 15 February 2011. *Solar Physics*, 280:335–345, October 2012.

[6] T. Amari, J. F. Luciani, Z. Mikic, and J. Linker. A Twisted Flux Rope Model for Coronal Mass Ejections and Two-Ribbon Flares. *The Astrophysical Journal Letters*, 529:L49–L52, January 2000.

[7] B. Anwar, L. W. Acton, H. S. Hudson, M. Makita, A. N. McClymont, and S. Tsuneta. Rapid Sunspot Motion during a Major Solar Flare. *Solar Physics*, 147(2):287–303, October 1993.

[8] V. Archontis and A. W. Hood. Formation of Ellerman bombs due to 3D flux emergence. *Astronomy & Astrophysics*, 508(3):1469–1483, December 2009.

[9] V. Archontis, A. W. Hood, and K. Tsinganos. The Emergence of Weakly Twisted Magnetic Fields in the Sun. *The Astrophysical Journal*, 778(1):42, November 2013.

[10] G. Aulanier. Solar physics: When the tail wags the dog. *Nature Physics*, 12(11):998–999, November 2016.

[11] A. K. Awasthi, R. Liu, H. Wang, Y. Wang, and C. Shen. Pre-eruptive Magnetic Reconnection within a Multi-flux-rope System in the Solar Corona. *The Astrophysical Journal*, 857(2):124, April 2018.

[12] S. D. Bale, K. Goetz, P. R. Harvey, P. Turin, J. W. Bonnell, T. Dudok de Wit, R. E. Ergun, R. J. MacDowall, M. Pulupa, M. Andre, M. Bolton, J. L. Bougeret, T. A. Bowen, D. Burgess, C. A. Cattell, B. D. G. Chandran, C. C. Chaston, C. H. K. Chen, M. K. Choi, J. E. Connerney, S. Cranmer, M. Diaz-Aguado, W. Donakowski, J. F. Drake, W. M. Farrell, P. Fergeau, J. Fermin, J. Fischer, N. Fox, D. Glaser, M. Goldstein, D. Gordon, E. Hanson, S. E. Harris, L. M. Hayes, J. J. Hinze, J. V. Hollweg, T. S. Horbury, R. A. Howard, V. Hoxie, G. Jannet, M. Karlsson, J. C. Kasper, P. J. Kellogg, M. Kien, J. A. Klimchuk, V. V. Krasnoselskikh, S. Krucker, J. J. Lynch, M. Maksimovic, D. M. Malaspina, S. Marker, P. Martin, J. Martinez-Oliveros, J. McCauley, D. J. McComas, T. McDonald, N. Meyer-Vernet, M. Moncuquet, S. J. Monson, F. S. Mozer, S. D. Murphy, J. Odom, R. Oliverson, J. Olson, E. N. Parker, D. Pankow, T. Phan, E. Quataert, T. Quinn, S. W. Ruplin, C. Salem, D. Seitz, D. A. Sheppard, A. Siy, K. Stevens, D. Summers, A. Szabo, M. Timofeeva, A. Vaivads, M. Velli, A. Yehle, D. Werthimer, and J. R. Wygant. The FIELDS Instrument Suite for Solar Probe Plus. Measuring the Coronal Plasma and Magnetic Field, Plasma Waves and Turbulence, and Radio Signatures of Solar Transients. *Space Science Reviews*, 204(1-4):49–82, December 2016.

[13] H. Balthasar, C. Beck, R. E. Louis, M. Verma, and C. Denker. Near-infrared spectropolarimetry of a δ-spot. *Astronomy & Astrophysics*, 562:L6, February 2014.

[14] C. Beck, R. Rezaei, K. G. Puschmann, and D. Fabbian. Spectroscopy at the Solar Limb: II. Are Spicules Heated to Coronal Temperatures? *Solar Physics*, 291(8):2281–2328, October 2016.

[15] N. Bello González, S. Danilovic, and F. Kneer. On the structure and dynamics of Ellerman bombs. Detailed study of three events and modelling of Hα. *Astronomy & Astrophysics*, 557:A102, September 2013.

[16] L. Bellot Rubio and D. Orozco Suárez. Quiet Sun magnetic fields: an observational view. *Living Reviews in Solar Physics*, 16(1):1, February 2019.

[17] Y. Bi, Y. Jiang, J. Yang, J. Hong, H. Li, B. Yang, and Z. Xu. Observation of a reversal of rotation in a sunspot during a solar flare. *Nature Communications*, 7:13798, December 2016.

[18] Y. Bi, J. Yang, Y. Jiang, J. Hong, Z. Xu, Z. Qu, and K. Ji. The Photospheric Vortex Flows during a Solar Flare. *The Astrophysical Journal Letters*, 849(2):L35, November 2017.

[19] J. M. Borrero, S. Tomczyk, M. Kubo, H. Socas-Navarro, J. Schou, S. Couvidat, and R. Bogart. VFISV: Very Fast Inversion of the Stokes Vector for the Helioseismic and Magnetic Imager. *Solar Physics*, 273(1):267–293, October 2011.

[20] J. J. Brants and C. Zwaan. The Structure of Sunspots - Part Four - Magnetic Field Strengths in Small Sunspots and Pores. *Solar Physics*, 80(2):251–258, October 1982.

[21] D. M. Butler and K. Papadopoulos. Solar terrestrial physics : present and future : a report based on the Solar Terrestrial Physics Workshop, December 1982 to November 1983. *NASA Reference Publication*, June 1984.

[22] J. I. Campos Rozo, D. Utz, S. Vargas Domínguez, A. Veronig, and T. Van Doorsselaere. Photospheric plasma and magnetic field dynamics during the formation of solar AR 11190. *Astronomy & Astrophysics*, 622:A168, February 2019.

[23] W. Cao, P. R. Goode, K. Ahn, N. Gorceix, W. Schmidt, and H. Lin. NIRIS: The Second Generation Near-Infrared Imaging Spectro-polarimeter for the 1.6 Meter New Solar Telescope. *Astronomical Society of the Pacific Conference Series*, 463:291, December 2012.

[24] W. Cao, N. Gorceix, R. Coulter, K. Ahn, T. R. Rimmele, and P. R. Goode. Scientific instrumentation for the 1.6 m New Solar Telescope in Big Bear. *Astronomische Nachrichten*, 331(6):636, June 2010.

[25] H. Carmichael. A Process for Flares. *NASA Special Publication*, 50:451, January 1964.

[26] R. C. Carrington. Description of a Singular Appearance seen in the Sun on September 1, 1859. *Monthly Notices of the Royal Astronomical Society*, 20:13–15, November 1859.

[27] J. S. Castellanos Durán, L. Kleint, and B. Calvo-Mozo. A Statistical Study of Photospheric Magnetic Field Changes During 75 Solar Flares. *The Astrophysical Journal*, 852(1):25, January 2018.

[28] R. Centeno. The Naked Emergence of Solar Active Regions Observed with SDO/HMI. *The Astrophysical Journal*, 759(1):72, November 2012.

[29] R. Centeno, J. Blanco Rodríguez, J. C. Del Toro Iniesta, S. K. Solanki, P. Barthol, A. Gand orfer, L. Gizon, J. Hirzberger, T. L. Riethmüller, M. van Noort, D. Orozco Suárez, T. Berkefeld, W. Schmidt, V. Martínez Pillet, and M. Knölker. A Tale of Two Emergences: Sunrise II Observations of Emergence Sites in a Solar Active Region. *The Astrophysical Journal Supplement Series*, 229(1):3, March 2017.

[30] R. Centeno, H. Socas-Navarro, B. Lites, M. Kubo, Z. Frank, R. Shine, T. Tarbell, A. Title, K. Ichimoto, S. Tsuneta, Y. Katsukawa, Y. Suematsu, T. Shimizu, and S. Nagata. Emergence of Small-Scale Magnetic Loops in the Quiet-Sun Internetwork. *The Astrophysical Journal Letters*, 666:L137–L140, September 2007.

[31] J. Chae, J. Qiu, H. Wang, and P. R. Goode. Extreme-Ultraviolet Jets and Hα Surges in Solar Microflares. *The Astrophysical Journal Letters*, 513(1):L75–L78, March 1999.

[32] W.-Z. Chen, C. Liu, H. Song, N. Deng, C.-Y. Tan, and H.-M. Wang. A Statistical Study of Rapid Sunspot Structure Change Associated with Flares. *Chin. J. Astron. Astrophys.*, 7:733–742, October 2007.

[33] M. C. M. Cheung and H. Isobe. Flux Emergence (Theory). *Living Reviews in Solar Physics*, 11(1):3, July 2014.

[34] M. C. M. Cheung, M. Rempel, A. M. Title, and M. Schüssler. Simulation of the Formation of a Solar Active Region. *The Astrophysical Journal*, 720(1):233–244, September 2010.

[35] M. C. M. Cheung, M. Schüssler, and F. Moreno-Insertis. Magnetic Flux Emergence in Granular Convection: Radiative MHD Simulations and Observational Signatures. *Astronomy & Astrophysics*, 467:703–719, May 2007.

[36] M. C. M. Cheung, M. Schüssler, T. D. Tarbell, and A. M. Title. Solar surface emerging flux regions: A comparative study of radiative MHD modeling andHinodeSOT observations. *The Astrophysical Journal*, 687(2):1373–1387, November 2008.

[37] J. Christensen-Dalsgaard, D. O. Gough, and M. J. Thompson. The Depth of the Solar Convection Zone. *The Astrophysical Journal*, 378:413, September 1991.

[38] S. Craig, S. E. Bulau, K. Gonzales, E. Hansen, B. Goodrich, R. P. Hubbard, E. Johansson, C. Liang, R. A. Kneale, W. McBride, P. Sekulic, and T. R. Williams. Daniel K. Inouye Solar Telescope: integration testing and commissioning planning. *Society of Photo-Optical Instrumentation Engineers (SPIE) Conference Series*, 9150:91500C, August 2014.

[39] S. R. Cranmer. Coronal Holes. *Living Reviews in Solar Physics*, 6(1):3, September 2009.

[40] S. Dacie, P. Démoulin, L. van Driel-Gesztelyi, D. M. Long, D. Baker, M. Janvier, S. L. Yardley, and D. Pérez-Suárez. Evolution of the magnetic field distribution of active regions. *Astronomy & Astrophysics*, 596:A69, December 2016.

[41] B. De Pontieu. High-Resolution Observations of Small-Scale Emerging Flux in the Photosphere. *The Astrophysical Journal*, 569:474–486, April 2002.

[42] B. De Pontieu, S. McIntosh, V. H. Hansteen, M. Carlsson, C. J. Schrijver, T. D. Tarbell, A. M. Title, R. A. Shine, Y. Suematsu, S. Tsuneta, Y. Katsukawa, K. Ichimoto, T. Shimizu, and S. Nagata. A Tale of Two Spicules: The Impact of Spicules on the Magnetic Chromosphere. *Publications of the Astronomical Society of Japan*, 59:S655, November 2007.

[43] B. De Pontieu, A. M. Title, J. R. Lemen, G. D. Kushner, D. J. Akin, B. Allard, T. Berger, P. Boerner, M. Cheung, C. Chou, J. F. Drake, D. W. Duncan, S. Freeland, G. F. Heyman, C. Hoffman, N. E. Hurlburt, R. W. Lindgren, D. Mathur, R. Rehse, D. Sabolish, R. Seguin, C. J. Schrijver, T. D. Tarbell, J. P. Wülser, C. J. Wolfson, C. Yanari, J. Mudge, N. Nguyen-Phuc, R. Timmons, R. van Bezooijen, I. Weingrod, R. Brookner, G. Butcher, B. Dougherty, J. Eder, V. Knagenhjelm, S. Larsen, D. Mansir, L. Phan, P. Boyle, P. N. Cheimets, E. E. DeLuca, L. Golub, R. Gates, E. Hertz, S. McKillop, S. Park, T. Perry, W. A. Podgorski, K. Reeves, S. Saar, P. Testa, H. Tian, M. Weber, C. Dunn, S. Eccles, S. A. Jaeggli, C. C. Kankelborg, K. Mashburn, N. Pust, L. Springer, R. Carvalho, L. Kleint, J. Marmie, E. Mazmanian, T. M. D. Pereira, S. Sawyer, J. Strong, S. P. Worden, M. Carlsson, V. H. Hansteen, J. Leenaarts, M. Wiesmann, J. Aloise, K. C. Chu, R. I. Bush, P. H. Scherrer, P. Brekke, J. Martinez-Sykora, B. W. Lites, S. W. McIntosh, H. Uitenbroek, T. J. Okamoto, M. A. Gummin, G. Auker, P. Jerram, P. Pool, and N. Waltham. The Interface Region Imaging Spectrograph (IRIS). *Solar Physics*, 289(7):2733–2779, July 2014.

[44] C. E. DeForest, H. J. Hagenaar, D. A. Lamb, C. E. Parnell, and B. T. Welsch. Solar Magnetic Tracking. I. Software Comparison and Recommended Practices. *The Astrophysical Journal*, 666(1):576–587, September 2007.

[45] P. Demoulin, L. G. Bagala, C. H. Mandrini, J. C. Henoux, and M. G. Rovira. Quasi-separatrix layers in solar flares. II. Observed magnetic configurations. *Astronomy & Astrophysics*, 325:305–317, September 1997.

[46] P. Demoulin, J. C. Henoux, E. R. Priest, and C. H. Mand rini. Quasi-Separatrix layers in solar flares. I. Method. *Astronomy & Astrophysics*, 308:643–655, April 1996.

[47] N. Deng, C. Liu, D. Prasad Choudhary, and H. Wang. Rapid Enhancement of Sheared Evershed Flow Along the Neutral Line Associated with an X6.5 Flare Observed by Hinode. *The Astrophysical Journal Letters*, 733(1):L14, May 2011.

[48] N. Deng, C. Liu, Y. Xu, K. Ahn, J. Jing, W. Cao, and H. Wang. 1.56 Micron Spectropolarimetry of Umbral Dots and Their Evolution Associated with a Major Flare. *AAS/Solar Physics Division Meeting*, 48:300.03, August 2017.

[49] N. Deng, C. Liu, G. Yang, H. Wang, and C. Denker. Rapid Penumbral Decay Associated with an X2.3 Flare in NOAA Active Region 9026. *The Astrophysical Journal*, 623(2):1195–1201, April 2005.

[50] N. Deng, D. Prasad Choudhary, and K. S. Balasubramaniam. On the Doppler Shift and Asymmetry of Stokes Profiles of Photospheric Fe I and Chromospheric Mg I Lines. *The Astrophysical Journal*, 719(1):385–393, August 2010.

[51] N. Deng, T. Shimizu, D. P. Choudhary, and H. Wang. What Determines the Penumbral Size and Evershed Flow Speed? *International Astronomical Union Symposium*, 273:216–220, August 2011.

[52] N. Deng, A. Tritschler, J. Jing, X. Chen, C. Liu, K. Reardon, C. Denker, Y. Xu, and H. Wang. High-cadence and High-resolution Hα Imaging Spectroscopy of a Circular Flare's Remote Ribbon with IBIS. *The Astrophysical Journal*, 769(2):112, June 2013.

[53] N. Deng, Y. Xu, G. Yang, W. Cao, C. Liu, T. R. Rimmele, H. Wang, and C. Denker. Multiwavelength Study of Flow Fields in Flaring Super Active Region NOAA 10486. *The Astrophysical Journal*, 644:1278–1291, June 2006.

[54] F. Ellerman. Solar Hydrogen "bombs". *The Astrophysical Journal*, 46:298, November 1917.

[55] Y. Fan. Nonlinear Growth of the Three-dimensional Undular Instability of a Horizontal Magnetic Layer and the Formation of Arching Flux Tubes. *The Astrophysical Journal*, 546(1):509–527, January 2001.

[56] Y. Fan. The Emergence of a Twisted Ω-Tube into the Solar Atmosphere. *The Astrophysical Journal Letters*, 554:L111–L114, June 2001.

[57] Y. Fan. Coronal Mass Ejections as Loss of Confinement of Kinked Magnetic Flux Ropes. *The Astrophysical Journal*, 630:543–551, September 2005.

[58] Y. Fan. On the Eruption of Coronal Flux Ropes. *The Astrophysical Journal*, 719:728–736, August 2010.

[59] A. J. Finley, S. P. Matt, V. Réville, R. F. Pinto, M. Owens, J. C. Kasper, K. E. Korreck, A. W. Case, M. L. Stevens, P. Whittlesey, D. Larson, and R. Livi. The Solar Wind Angular Momentum Flux as Observed by Parker Solar Probe. *The Astrophysical Journal Letters*, 902(1):L4, October 2020.

[60] C. E. Fischer, J. M. Borrero, N. Bello González, and A. J. Kaithakkal. Observations of solar small-scale magnetic flux-sheet emergence. *Astronomy & Astrophysics*, 622:L12, February 2019.

[61] G. H. Fisher, D. J. Bercik, B. T. Welsch, and H. S. Hudson. Global Forces in Eruptive Solar Flares: The Lorentz Force Acting on the Solar Atmosphere and the Solar Interior. *Solar Physics*, 277(1):59–76, March 2012.

[62] L. A. Fisk. The Open Magnetic Flux of the Sun. I. Transport by Reconnections with Coronal Loops. *The Astrophysical Journal*, 626(1):563–573, June 2005.

[63] L. A. Fisk and J. C. Kasper. Global Circulation of the Open Magnetic Flux of the Sun. *The Astrophysical Journal Letters*, 894(1):L4, May 2020.

[64] T. G. Forbes and E. R. Priest. Numerical Simulation of Reconnection in an Emerging Magnetic Flux Region. *Solar Physics*, 94(2):315–340, September 1984.

[65] H. A. Garcia. Temperature and Emission Measure from Goes Soft X-Ray Measurements. *Solar Physics*, 154(2):275–308, October 1994.

[66] D. E. Gary, G. J. Hurford, G. M. Nita, G. D. Fleishman, and J. M. McTiernan. Expanded Owens Valley Solar Array Science and Data Products. *American Astronomical Society Meeting Abstracts*, 216:405.20, May 2010.

[67] G. A Gary and M. J. Hagyard. Transformation of vector magnetograms and the problems associated with the effects of perspective and the azimuthal ambiguity. *Solar Physics*, 126:21–36, March 1990.

[68] E. M. Golubeva and A. V. Mordvinov. Decay of Activity Complexes, Formation of Unipolar Magnetic Regions, and Coronal Holes in Their Causal Relation. *Solar Physics*, 291(12):3605–3617, December 2016.

[69] P. Gömöry, C. Beck, H. Balthasar, J. Rybák, A. Kučera, J. Koza, and H. Wöhl. Magnetic loop emergence within a granule. *Astronomy & Astrophysics*, 511:A14, February 2010.

[70] P. R. Goode and W. Cao. The 1.6 m off-axis New Solar Telescope (NST) in Big Bear. *Society of Photo-Optical Instrumentation Engineers (SPIE) Conference Series*, 8444:844403, September 2012.

[71] P. R. Goode, R. Coulter, N. Gorceix, V. Yurchyshyn, and W. Cao. The NST: First results and some lessons for ATST and EST. *Astronomische Nachrichten*, 331:620, June 2010.

[72] P. R. Goode, V. Yurchyshyn, W. Cao, V. Abramenko, A. Andic, K. Ahn, and J. Chae. Highest Resolution Observations of the Quietest Sun. *The Astrophysical Journal Letters*, 714:L31–L35, May 2010.

[73] S. Gosain. Evidence for Collapsing Fields in the Corona and Photosphere during the 2011 February 15 X2.2 Flare: SDO/AIA and HMI Observations. *The Astrophysical Journal*, 749(1):85, April 2012.

[74] M. Gošić, J. de la Cruz Rodríguez, B. De Pontieu, L. R. Bellot Rubio, M. Carlsson, S. Esteban Pozuelo, A. Ortiz, and V. Polito. Chromospheric heating due to cancellation of quiet sun internetwork fields. *The Astrophysical Journal*, 857(1):48, April 2018.

[75] M. Gošić, L. R. Bellot Rubio, J. C. del Toro Iniesta, D. Orozco Suárez, and Y. Katsukawa. The Solar Internetwork. II. Flux Appearance and Disappearance Rates. *The Astrophysical Journal*, 820(1):35, March 2016.

[76] H. J. Hagenaar, C. J. Schrijver, and A. M. Title. The Properties of Small Magnetic Regions on the Solar Surface and the Implications for the Solar Dynamo(s). *The Astrophysical Journal*, 584(2):1107–1119, February 2003.

[77] G. E. Hale. On the Probable Existence of a Magnetic Field in Sun-Spots. *The Astrophysical Journal*, 28:315, November 1908.

[78] J. Harvey and D. Hall. Magnetic Field Observations with Fe I λ15648 Å. *Bulletin of the American Astronomical Society*, 7:459, June 1975.

[79] K. L. Harvey and J. W. Harvey. A Study of the Magnetic and Velocity Fields in an Active Region. *Solar Physics*, 47:233–246, March 1976.

[80] S. G. Heinemann, M. Temmer, S. J. Hofmeister, A. M. Veronig, and S. Vennerstrøm. Three-phase Evolution of a Coronal Hole. I. 360° Remote Sensing and In Situ Observations. *The Astrophysical Journal*, 861(2):151, July 2018.

[81] T. Hirayama. Theoretical Model of Flares and Prominences. I: Evaporating Flare Model. *Solar Physics*, 34(2):323–338, February 1974.

[82] R. Hodgson. On a curious Appearance seen in the Sun. *Monthly Notices of the Royal Astronomical Society*, 20:15–16, November 1859.

[83] J. T. Hoeksema, Y. Liu, K. Hayashi, X. Sun, J. Schou, S. Couvidat, A. Norton, M. Bobra, R. Centeno, K. D. Leka, G. Barnes, and M. Turmon. The Helioseismic and Magnetic Imager (HMI) Vector Magnetic Field Pipeline: Overview and Performance. *Solar Physics*, 289:3483–3530, September 2014.

[84] S. J. Hofmeister, A. Veronig, M. A. Reiss, M. Temmer, S. Vennerstrom, B. Vršnak, and B. Heber. Characteristics of Low-latitude Coronal Holes near the Maximum of Solar Cycle 24. *The Astrophysical Journal*, 835(2):268, February 2017.

[85] H. Hotta and T. Yokoyama. Generation of twist on magnetic flux tubes at the base of the solar convection zone. *Astronomy & Astrophysics*, 548:A74, December 2012.

[86] R. A. Howard, J. D. Moses, D. G. Socker, K. P. Dere, J. W. Cook, and Secchi Consortium. Sun earth connection coronal and heliospheric investigation (SECCHI). *Advances in Space Research*, 29(12):2017–2026, January 2002.

[87] Q. Hu, B. Dasgupta, M. L. Derosa, J. Büchner, and G. A. Gary. Non-force-free extrapolation of solar coronal magnetic field using vector magnetograms. *Journal of Atmospheric and Solar-Terrestrial Physics*, 72(2-3):219–223, February 2010.

[88] H. S. Hudson. Implosions in Coronal Transients. *The Astrophysical Journal Letters*, 531(1):L75–L77, March 2000.

[89] H. S. Hudson, G. H. Fisher, and B. T. Welsch. Flare Energy and Magnetic Field Variations. *Astronomical Society of the Pacific Conference Series*, 383:221–226, January 2008.

[90] K. Ichimoto. The Evershed Effect with SOT/Hinode. *Astrophysics and Space Science Proceedings*, 19:186–192, 2010.

[91] K. Ichimoto and Solar-B Team. The Solar-B Mission. *Journal of Korean Astronomical Society*, 38(2):307–310, June 2005.

[92] S. Inoue, K. Hayashi, T. Magara, G. S. Choe, and Y. D. Park. Magnetohydrodynamic Simulation of the X2.2 Solar Flare on 2011 February 15. II. Dynamics Connecting the Solar Flare and the Coronal Mass Ejection. *The Astrophysical Journal*, 803(2):73, April 2015.

[93] S. Inoue, K. Kusano, J. Büchner, and J. Skála. Formation and dynamics of a solar eruptive flux tube. *Nature Communications*, 9:174, January 2018.

[94] H. Isobe, D. Tripathi, and V. Archontis. Ellerman Bombs and Jets Associated with Resistive Flux Emergence. *The Astrophysical Journal Letters*, 657(1):L53–L56, March 2007.

[95] C. Jiang, X. Feng, S. Wu, and Q. Hu. A Magnetic Bald-patch Flare in Solar Active Region 11117. *Research in Astronomy and Astrophysics*, 17(9):093, September 2017.

[96] C. Jin, J. Wang, and M. Zhao. Vector Magnetic Fields of Solar Granulation. *The Astrophysical Journal*, 690(1):279–287, December 2008.

[97] J. Jing, R. Liu, M. C. M. Cheung, J. Lee, Y. Xu, C. Liu, C. Zhu, and H. Wang. Witnessing a Large-scale Slipping Magnetic Reconnection along a Dimming Channel during a Solar Flare. *The Astrophysical Journal Letters*, 842(2):L18, June 2017.

[98] J. Jing, C. Tan, Y. Yuan, B. Wang, T. Wiegelmann, Y. Xu, and H. Wang. Free Magnetic Energy and Flare Productivity of Active Regions. *The Astrophysical Journal*, 713(1):440–449, April 2010.

[99] J. Jing, T. Wiegelmann, Y. Suematsu, M. Kubo, and H. Wang. Changes of Magnetic Structure in Three Dimensions Associated with the X3.4 Flare of 2006 December 13. *The Astrophysical Journal Letters*, 676(1):L81, March 2008.

[100] J. Jing, Y. Xu, W. Cao, C. Liu, D. E. Gary, and H. Wang. Unprecedented Fine Structure of a Solar Flare Revealed by the 1.6 m New Solar Telescope. *Scientific Reports*, 6:24319, September 2016.

[101] N. V. Karachik, A. A. Pevtsov, and V. I. Abramenko. Formation of Coronal Holes on the Ashes of Active Regions. *The Astrophysical Journal*, 714(2):1672–1678, May 2010.

[102] J. C. Kasper, R. Abiad, G. Austin, M. Balat-Pichelin, S. D. Bale, J. W. Belcher, P. Berg, H. Bergner, M. Berthomier, J. Bookbinder, E. Brodu, D. Caldwell, A. W. Case, B. D. G. Chandran, P. Cheimets, J. W. Cirtain, S. R. Cranmer, D. W. Curtis, P. Daigneau, G. Dalton, B. Dasgupta, D. DeTomaso, M. Diaz-Aguado, B. Djordjevic, B. Donaskowski, M. Effinger, V. Florinski, N. Fox, M. Freeman, D. Gallagher, S. P Gary, T. Gauron, R. Gates, M. Goldstein, L. Golub, D. A. Gordon, R. Gurnee, G. Guth, J. Halekas, K. Hatch, J. Heerikuisen, G. Ho, Q. Hu, G. Johnson, S. P. Jordan, K. E. Korreck, D. Larson, A. J. Lazarus, G. Li, R. Livi, M. Ludlam, M. Maksimovic, J. P. McFadden, W. Marchant, B. A. Maruca, D. J. McComas, L. Messina, T. Mercer, S. Park, A. M. Peddie, N. Pogorelov, M. J. Reinhart, J. D. Richardson, M. Robinson, I. Rosen, R. M. Skoug, A. Slagle, J. T. Steinberg, M. L. Stevens, A. Szabo, E. R. Taylor, C. Tiu, P. Turin, M. Velli, G. Webb, P. Whittlesey, K. Wright, S. T. Wu, and G. Zank. Solar Wind Electrons Alphas and Protons (SWEAP) Investigation: Design of the Solar Wind and Coronal Plasma Instrument Suite for Solar Probe Plus. *Space Science Reviews*, 204(1-4):131–186, December 2016.

[103] I. N. Kitiashvili, A. G. Kosovichev, A. A. Wray, and N. N. Mansour. Traveling Waves of Magnetoconvection and the Origin of the Evershed Effect in Sunspots. *The Astrophysical Journal Letters*, 700:L178–L181, August 2009.

[104] R. A. Kopp and G. W. Pneuman. Magnetic reconnection in the corona and the loop prominence phenomenon. *Solar Physics*, 50(1):85–98, October 1976.

[105] H. Künzel. Die Flare-Häufigkeit in Fleckengruppen unterschiedlicher Klasse und magnetischer Struktur. *Astronomische Nachrichten*, 285(5):271, August 1960.

[106] D. Kuridze, M. Mathioudakis, D. B. Jess, S. Shelyag, D. J. Christian, F. P. Keenan, and K. S. Balasubramaniam. Small-scale Hα jets in the solar chromosphere. *Astronomy & Astrophysics*, 533:A76, September 2011.

[107] K. D. Leka and G. Barnes. Photospheric Magnetic Field Properties of Flaring versus Flare-quiet Active Regions. IV. A Statistically Significant Sample. *The Astrophysical Journal*, 656(2):1173–1186, February 2007.

[108] K. D. Leka, G. Barnes, and A. Crouch. An Automated Ambiguity-Resolution Code for Hinode/SP Vector Magnetic Field Data. *Astronomical Society of the Pacific Conference Series*, 415:365, December 2009.

[109] K. D. Leka, G. Barnes, A. D. Crouch, T. R. Metcalf, G. A Gary, J. Jing, and Y. Liu. Resolving the 180° Ambiguity in Solar Vector Magnetic Field Data: Evaluating the Effects of Noise, Spatial Resolution, and Method Assumptions. *Solar Physics*, 260(1):83–108, November 2009.

[110] K. D. Leka and O. Steiner. Understanding Small Solar Magnetic Structures: Comparing Numerical Simulations to Observations. *The Astrophysical Journal*, 552(1):354–371, May 2001.

[111] J. R. Lemen, A. M. Title, D. J. Akin, P. F. Boerner, C. Chou, J. F. Drake, D. W. Duncan, C. G. Edwards, F. M. Friedlaender, G. F. Heyman, N. E. Hurlburt, N. L. Katz, G. D. Kushner, M. Levay, R. W. Lindgren, D. P. Mathur, E. L. McFeaters, S. Mitchell, R. A. Rehse, C. J. Schrijver, L. A. Springer, R. A. Stern, T. D. Tarbell, J.-P. Wuelser, C. J. Wolfson, C. Yanari, J. A. Bookbinder, P. N. Cheimets, D. Caldwell, E. E. Deluca, R. Gates, L. Golub, S. Park, W. A. Podgorski, R. I. Bush, P. H. Scherrer, M. A. Gummin, P. Smith, G. Auker, P. Jerram, P. Pool, R. Soufli, D. L. Windt, S. Beardsley, M. Clapp, J. Lang, and N. Waltham. The Atmospheric Imaging Assembly (AIA) on the Solar Dynamics Observatory (SDO). *Solar Physics*, 275:17–40, January 2012.

[112] Y. Li, J. Jing, Y. Fan, and H. Wang. Comparison Between Observation and Simulation of Magnetic Field Changes Associated with Flares. *The Astrophysical Journal Letters*, 727(1):L19, January 2011.

[113] Y. Li, J. Jing, C. Tan, and H. Wang. The Change of Magnetic Inclination Angles Associated with the X3.4 Flare on December 13, 2006. *Science in China: Physics, Mechanics and Astronomy*, 52:1702–1706, November 2009.

[114] E.-K. Lim, V. Yurchyshyn, V. Abramenko, K. Ahn, W. Cao, and P. Goode. Photospheric Signatures of Granular-scale Flux Emergence and Cancellation at the Penumbral Boundary. *The Astrophysical Journal*, 740:82, October 2011.

[115] B. W. Lites, K. D. Leka, A. Skumanich, V. Martinez Pillet, and T. Shimizu. Small-Scale Horizontal Magnetic Fields in the Solar Photosphere. *The Astrophysical Journal*, 460:1019, April 1996.

[116] B. W. Lites, A. Skumanich, and V. Martinez Pillet. Vector magnetic fields of emerging solar flux. I. Properties at the site of emergence. *Astronomy & Astrophysics*, 333:1053–1068, May 1998.

[117] C. Liu, N. Deng, J. Lee, T. Wiegelmann, C. Jiang, B. R. Dennis, Y. Su, A. Donea, and H. Wang. Three-dimensional Magnetic Restructuring in Two Homologous Solar Flares in the Seismically Active NOAA AR 11283. *The Astrophysical Journal*, 795:128, November 2014.

[118] C. Liu, N. Deng, R. Liu, J. Lee, T. Wiegelmann, J. Jing, Y. Xu, S. Wang, and H. Wang. Rapid Changes of Photospheric Magnetic Field after Tether-cutting Reconnection and Magnetic Implosion. *The Astrophysical Journal Letters*, 745:L4, January 2012.

[119] C. Liu, N. Deng, R. Liu, I. Ugarte-Urra, S. Wang, and H. Wang. A Standard-to-blowout Jet. *The Astrophysical Journal Letters*, 735(1):L18, July 2011.

[120] C. Liu, N. Deng, Y. Liu, D. Falconer, P. R. Goode, C. Denker, and H. Wang. Rapid Change of δ Spot Structure Associated with Seven Major Flares. *The Astrophysical Journal*, 622:722–736, March 2005.

[121] C. Liu, N. Deng, and H. Wang. Rapid Sunspot Displacement Associated with Solar Eruptions. *American Astronomical Society Meeting Abstracts*, 216:404.13, May 2010.

[122] C. Liu, Y. Xu, W. Cao, N. Deng, J. Lee, H. S. Hudson, D. E. Gary, J. Wang, J. Jing, and H. Wang. Flare Differentially Rotates Sunspot on Sun's Surface. *Nature Communications*, 7:13104, October 2016.

[123] C. Liu, Y. Xu, W. Cao, N. Deng, J. Lee, H. S. Hudson, D. E. Gary, J. Wang, J. Jing, and H. Wang. Flare differentially rotates sunspot on Sun's surface. *Nature Communications*, 7:13104, October 2016.

[124] R. Liu, B. Kliem, V. S. Titov, J. Chen, Y. Wang, H. Wang, C. Liu, Y. Xu, and T. Wiegelmann. Structure, Stability, and Evolution of Magnetic Flux Ropes from the Perspective of Magnetic Twist. *The Astrophysical Journal*, 818(2):148, February 2016.

[125] R. Liu, C. Liu, T. Török, Y. Wang, and H. Wang. Contracting and Erupting Components of Sigmoidal Active Regions. *The Astrophysical Journal*, 757(2):150, October 2012.

[126] R. Liu and H. Wang. Coronal Implosion and Particle Acceleration in the Wake of a Filament Eruption. *The Astrophysical Journal Letters*, 703(1):L23–L28, September 2009.

[127] R. Liu and H. Wang. Fast Contraction of Coronal Loops at the Flare Peak. *The Astrophysical Journal Letters*, 714(1):L41–L46, May 2010.

[128] R. Liu, H. Wang, and D. Alexander. Implosion in a Coronal Eruption. *The Astrophysical Journal*, 696(1):121–135, May 2009.

[129] W. Livingston and F. Watson. A new solar signal: Average maximum sunspot magnetic fields independent of activity cycle. *Geophysical Research Letters*, 42(21):9185–9189, November 2015.

[130] M. J. Martínez González and L. R. Bellot Rubio. Emergence of Small-scale Magnetic Loops Through the Quiet Solar Atmosphere. *The Astrophysical Journal*, 700(2):1391–1403, August 2009.

[131] V. Martinez Pillet and M. Vazquez. The continuum intensity-magnetic field relation in sunspot umbrae. *Astronomy & Astrophysics*, 270(1-2):494–508, March 1993.

[132] R. A. Maurya, P. Vemareddy, and A. Ambastha. Velocity and Magnetic Transients Driven by the X2.2 White-light Flare of 2011 February 15 in NOAA 11158. *The Astrophysical Journal*, 747(2):134, March 2012.

[133] E. B. Mayfield and J. K. Lawrence. The Correlation of Solar Flare Production with Magnetic Energy in Active Regions. *Solar Physics*, 96(2):293–305, April 1985.

[134] D. J. McComas, N. Alexander, N. Angold, S. Bale, C. Beebe, B. Birdwell, M. Boyle, J. M. Burgum, J. A. Burnham, E. R. Christian, W. R. Cook, S. A. Cooper, A. C. Cummings, A. J. Davis, M. I. Desai, J. Dickinson, G. Dirks, D. H. Do, N. Fox, J. Giacalone, R. E. Gold, R. S. Gurnee, J. R. Hayes, M. E. Hill, J. C. Kasper, B. Kecman, J. Klemic, S. M. Krimigis, A. W. Labrador, R. S. Layman, R. A. Leske, S. Livi, W. H. Matthaeus, R. L. McNutt, R. A. Mewaldt, D. G. Mitchell, K. S. Nelson, C. Parker, J. S. Rankin, E. C. Roelof, N. A. Schwadron, H. Seifert, S. Shuman, M. R. Stokes, E. C. Stone, J. D. Vandegriff, M. Velli, T. T. von Rosenvinge, S. E. Weidner, M. E. Wiedenbeck, and P. Wilson. Integrated Science Investigation of the Sun (ISIS): Design of the Energetic Particle Investigation. *Space Science Reviews*, 204(1-4):187–256, December 2016.

[135] C. Meegan, G. Lichti, P. N. Bhat, E. Bissaldi, M. S. Briggs, V. Connaughton, R. Diehl, G. Fishman, J. Greiner, A. S. Hoover, A. J. van der Horst, A. von Kienlin, R. M. Kippen, C. Kouveliotou, S. McBreen, W. S. Paciesas, R. Preece, H. Steinle, M. S. Wallace, R. B. Wilson, and C. Wilson-Hodge. The Fermi Gamma-ray Burst Monitor. *The Astrophysical Journal*, 702:791–804, September 2009.

[136] T. R. Metcalf. Resolving the 180-degree ambiguity in vector magnetic field measurements: The 'minimum' energy solution. *Solar Physics*, 155(2):235–242, December 1994.

[137] T. R. Metcalf, K. D. Leka, G. Barnes, B. W. Lites, M. K. Georgoulis, A. A. Pevtsov, K. S. Balasubramaniam, G. A Gary, J. Jing, J. Li, Y. Liu, H. Wang, V. Abramenko, V. Yurchyshyn, and Y. J. Moon. An Overview of Existing Algorithms for Resolving the 180 Ambiguity in Vector Magnetic Fields: Quantitative Tests with Synthetic Data. *Solar Physics*, 237(2):267–296, September 2006.

[138] J. G. Mitchell, G. A. de Nolfo, M. E. Hill, E. R. Christian, D. J. McComas, N. A. Schwadron, M. E. Wiedenbeck, S. D. Bale, A. W. Case, C. M. S. Cohen, C. J. Joyce, J. C. Kasper, A. W. Labrador, R. A. Leske, R. J. MacDowall, R. A. Mewaldt, D. G. Mitchell, M. Pulupa, I. G. Richardson, M. L. Stevens, and J. R. Szalay. Small Electron Events Observed by Parker Solar Probe/ISOIS during Encounter 2. *The Astrophysical Journal*, 902(1):20, October 2020.

[139] R. L. Moore, J. W. Cirtain, A. C. Sterling, and D. A. Falconer. Dichotomy of Solar Coronal Jets: Standard Jets and Blowout Jets. *The Astrophysical Journal*, 720(1):757–770, September 2010.

[140] R. L. Moore, A. C. Sterling, H. S. Hudson, and J. R. Lemen. Onset of the Magnetic Explosion in Solar Flares and Coronal Mass Ejections. *The Astrophysical Journal*, 552(2):833–848, May 2001.

[141] F. Moreno-Insertis and T. Emonet. The Rise of Twisted Magnetic Tubes in a Stratified Medium. *The Astrophysical Journal Letters*, 472:L53, November 1996.

[142] F. Moreno-Insertis and K. Galsgaard. Plasma Jets and Eruptions in Solar Coronal Holes: A Three-dimensional Flux Emergence Experiment. *The Astrophysical Journal*, 771(1):20, July 2013.

[143] F. Moreno-Insertis, K. Galsgaard, and I. Ugarte-Urra. Jets in Coronal Holes: Hinode Observations and Three-dimensional Computer Modeling. *The Astrophysical Journal Letters*, 673(2):L211, February 2008.

[144] F. Moreno-Insertis, J. Martinez-Sykora, V. H. Hansteen, and D. Muñoz. Small-scale Magnetic Flux Emergence in the Quiet Sun. *The Astrophysical Journal Letters*, 859(2):L26, June 2018.

[145] F. S. Mozer, J. W. Bonnell, T. A. Bowen, G. Schumm, and I. Y. Vasko. Large-amplitude, Wideband, Doppler-shifted, Ion Acoustic Waves Observed on the Parker Solar Probe. *The Astrophysical Journal*, 901(2):107, October 2020.

[146] L. J. November and G. W. Simon. Precise Proper-motion Measurement of Solar Granulation. *The Astrophysical Journal*, 333:427–442, October 1988.

[147] T. Oba, T. L. Riethmüller, S. K. Solanki, Y. Iida, C. Quintero Noda, and T. Shimizu. The Small-scale Structure of Photospheric Convection Retrieved by a Deconvolution Technique Applied to Hinode/SP Data. *The Astrophysical Journal*, 849:7, November 2017.

[148] A. Ortiz, L. R. Bellot Rubio, V. H. Hansteen, J. de la Cruz Rodríguez, and L. Rouppe van der Voort. Emergence of Granular-sized Magnetic Bubbles through the Solar Atmosphere. I. Spectropolarimetric Observations and Simulations. *The Astrophysical Journal*, 781(2):126, February 2014.

[149] K. Otsuji, R. Kitai, K. Ichimoto, and K. Shibata. Statistical Study on the Nature of Solar-Flux Emergence. *Publications of the Astronomical Society of Japan*, 63:1047–1057, October 2011.

[150] N. K. Panesar, A. C. Sterling, and R. L. Moore. Magnetic flux cancelation as the trigger of solar coronal jets in coronal holes. *The Astrophysical Journal*, 853(2):189, February 2018.

[151] N. K. Panesar, A. C. Sterling, R. L. Moore, S. K. Tiwari, B. De Pontieu, and A. A. Norton. IRIS and SDO Observations of Solar Jetlets Resulting from Network-edge Flux Cancelation. *The Astrophysical Journal Letters*, 868(2):L27, December 2018.

[152] E. Pariat, G. Aulanier, B. Schmieder, M. K. Georgoulis, D. M. Rust, and P. N. Bernasconi. Resistive Emergence of Undulatory Flux Tubes. *The Astrophysical Journal*, 614:1099–1112, October 2004.

[153] S. Park. An Observational Test of Solar Plasma Heating by Magnetic Flux Cancellation. *The Astrophysical Journal*, 897(1):49, July 2020.

[154] E. N. Parker. The Formation of Sunspots from the Solar Toroidal Field. *The Astrophysical Journal*, 121:491, March 1955.

[155] E. N. Parker. The Origin of Solar Activity. *Annual Review of Astronomy and Astrophysics*, 15:45–68, 1977.

[156] A. Patterson and H. Zirin. Transient magnetic field changes in flares. *The Astrophysical Journal Letters*, 243:L99–L101, January 1981.

[157] G. J. D. Petrie. The Abrupt Changes in the Photospheric Magnetic and Lorentz Force Vectors during Six Major Neutral-line Flares. *The Astrophysical Journal*, 759:50, November 2012.

[158] G. J. D. Petrie. Estimating Flare-Related Photospheric Lorentz Force Vector Changes Within Active Regions. *Solar Physics*, 289(10):3663–3680, October 2014.

[159] Y. B. Ponomarenko. Mechanism for the Formation of Sunspots. *Astronomical Journal*, 16:116, August 1972.

[160] C. Debi Prasad. Near infrared observations of the solar atmosphere. *Bulletin of the Astronomical Society of India*, 26:253, January 1998.

[161] E. R. Priest and T. G. Forbes. The magnetic nature of solar flares. *Astronomy & Astrophysics Review*, 10(4):313–377, January 2002.

[162] J. Qiu and D. E. Gary. Flare-related Magnetic Anomaly with a Sign Reversal. *The Astrophysical Journal*, 599(1):615–625, December 2003.

[163] M. A. Raadu. Suppression of the Kink Instability for Magnetic Flux Ropes in the Chromosphere. *Solar Physics*, 22(2):425–433, February 1972.

[164] A. Reid, M. Mathioudakis, E. Scullion, J. G. Doyle, S. Shelyag, and P. Gallagher. Ellerman Bombs with Jets: Cause and Effect. *The Astrophysical Journal*, 805(1):64, May 2015.

[165] M. Rempel, M. Schüssler, and M. Knölker. Radiative Magnetohydrodynamic Simulation of Sunspot Structure. *The Astrophysical Journal*, 691:640–649, January 2009.

[166] M. Rieutord and F. Rincon. The Sun's Supergranulation. *Living Reviews in Solar Physics*, 7(1):2, December 2010.

[167] M. Rieutord, T. Roudier, F. Rincon, J. M. Malherbe, N. Meunier, T. Berger, and Z. Frank. On the power spectrum of solar surface flows. *Astronomy & Astrophysics*, 512:A4, March 2010.

[168] M. A. Roberts, V. M. Uritsky, C. R. DeVore, and J. T. Karpen. Simulated Encounters of the Parker Solar Probe with a Coronal-hole Jet. *The Astrophysical Journal*, 866(1):14, October 2018.

[169] T. Samanta, H. Tian, V. Yurchyshyn, H. Peter, W. Cao, A. Sterling, R. Erdélyi, K. Ahn, S. Feng, D. Utz, D. Banerjee, and Y. Chen. Generation of solar spicules and subsequent atmospheric heating. *Science*, 366(6467):890–894, November 2019.

[170] H. U. Schmidt. Magnetohydrodynamics of an Active Region. *International Astronomical Union Symposium*, 35:95, 1968.

[171] H. U. Schmidt. Why the Chromosphere has its Discrete Fine Structure. *International Astronomical Union Symposium*, 56:35, 1974.

[172] J. Schou, P. H. Scherrer, R. I. Bush, R. Wachter, S. Couvidat, M. C. Rabello-Soares, R. S. Bogart, J. T. Hoeksema, Y. Liu, T. L. Duvall, D. J. Akin, B. A. Allard, J. W. Miles, R. Rairden, R. A. Shine, T. D. Tarbell, A. M. Title, C. J. Wolfson, D. F. Elmore, A. A. Norton, and S. Tomczyk. Design and Ground Calibration of the Helioseismic and Magnetic Imager (HMI) Instrument on the Solar Dynamics Observatory (SDO). *Solar Physics*, 275(1-2):229–259, January 2012.

[173] P. W. Schuck. Tracking Magnetic Footpoints with the Magnetic Induction Equation. *The Astrophysical Journal*, 646:1358–1391, August 2006.

[174] P. W. Schuck. Tracking Vector Magnetograms with the Magnetic Induction Equation. *The Astrophysical Journal*, 683(2):1134–1152, August 2008.

[175] D. H. Sekse, L. Rouppe van der Voort, B. De Pontieu, and E. Scullion. Interplay of Three Kinds of Motion in the Disk Counterpart of Type II Spicules: Upflow, Transversal, and Torsional Motions. *The Astrophysical Journal*, 769(1):44, May 2013.

[176] Jr. Sheeley, N. R. Observations of Small-Scale Solar Magnetic Fields. *Solar Physics*, 1(2):171–179, March 1967.

[177] K. Shibata and T. Magara. Solar Flares: Magnetohydrodynamic Processes. *Living Reviews in Solar Physics*, 8, December 2011.

[178] K. Shibata, S. Masuda, M. Shimojo, H. Hara, T. Yokoyama, S. Tsuneta, T. Kosugi, and Y. Ogawara. Hot-Plasma Ejections Associated with Compact-Loop Solar Flares. *The Astrophysical Journal Letters*, 451:L83, October 1995.

[179] K. Shibata, T. Nakamura, T. Matsumoto, K. Otsuji, T. J. Okamoto, N. Nishizuka, T. Kawate, H. Watanabe, S. Nagata, S. UeNo, R. Kitai, S. Nozawa, S. Tsuneta, Y. Suematsu, K. Ichimoto, T. Shimizu, Y. Katsukawa, T. D. Tarbell, T. E. Berger, B. W. Lites, R. A. Shine, and A. M. Title. Chromospheric Anemone Jets as Evidence of Ubiquitous Reconnection. *Science*, 318(5856):1591, December 2007.

[180] S. Shumko, N. Gorceix, S. Choi, A. Kellerer, W. Cao, P. R. Goode, V. Abramenko, K. Richards, T. R. Rimmele, and J. Marino. AO-308: the high-order adaptive optics system at Big Bear Solar Observatory. *Society of Photo-Optical Instrumentation Engineers (SPIE) Conference Series*, 9148:914835, August 2014.

[181] P. J. A. Simões, L. Fletcher, H. S. Hudson, and A. J. B. Russell. Implosion of Coronal Loops during the Impulsive Phase of a Solar Flare. *The Astrophysical Journal*, 777(2):152, November 2013.

[182] H. N. Smitha, L. S. Anusha, S. K. Solanki, and T. L. Riethmüller. Estimation of the Magnetic Flux Emergence Rate in the Quiet Sun from Sunrise Data. *The Astrophysical Journal Supplement Series*, 229(1):17, March 2017.

[183] D. G. Socker, G. E. Brueckner, C. M. Korendyke, and R. Schwenn. Spectrometric and spectropolarimetric observation of the solar corona with the LASCO/SOHO Lyot coronagraph. *Society of Photo-Optical Instrumentation Engineers (SPIE) Conference Series*, 2283:53–57, November 1994.

[184] S. K. Solanki. Smallscale Solar Magnetic Fields - an Overview. *Space Science Reviews*, 63(1-2):1–188, March 1993.

[185] S. K. Solanki. Sunspots: An Overview. *Astronomy & Astrophysics Review*, 11:153–286, 2003.

[186] S. K. Solanki, C. A. P. Montavon, and W. Livingston. Infrared lines as probes of solar magnetic features. 7: On the nature of the Evershed effect in sunspots. *Astronomy & Astrophysics*, 283:221–231, March 1994.

[187] S. K. Solanki, I. K. Rueedi, and W. Livingston. Infrared lines as probes of solar magnetic features. II - Diagnostic capabilities of Fe I 15648.5 A and 15652.9 A. *Astronomy & Astrophysics*, 263(1-2):312–322, September 1992.

[188] Y. L. Song and M. Zhang. On the Relationship Between Sunspot Structure and Magnetic Field Changes Associated with Solar Flares. *The Astrophysical Journal*, 826(2):173, August 2016.

[189] H. C. Spruit. A model of the solar convection zone. *Solar Physics*, 34(2):277–290, February 1974.

[190] A. C. Sterling and R. L. Moore. A Microfilament-eruption Mechanism for Solar Spicules. *The Astrophysical Journal Letters*, 828(1):L9, September 2016.

[191] A. C. Sterling, R. L. Moore, D. A. Falconer, and M. Adams. Small-scale filament eruptions as the driver of X-ray jets in solar coronal holes. *Nature*, 523(7561):437–440, July 2015.

[192] A. C. Sterling, R. L. Moore, N. K. Panesar, and T. Samanta. Possible Evolution of Minifilament-Eruption-Produced Solar Coronal Jets, Jetlets, and Spicules, into Magnetic-Twist-Wave "Switchbacks" Observed by the Parker Solar Probe (PSP). *arXiv e-prints*, page arXiv:2010.12991, October 2020.

[193] A. C. Sterling, R. L. Moore, T. Samanta, and V. Yurchyshyn. Possible production of solar spicules by microfilament eruptions. *The Astrophysical Journal*, 893(2):L45, April 2020.

[194] L. H. Strous, G. Scharmer, T. D. Tarbell, A. M. Title, and C. Zwaan. Phenomena in an emerging active region. I. Horizontal dynamics. *Astronomy & Astrophysics*, 306:947, February 1996.

[195] L. H. Strous and C. Zwaan. Phenomena in an emerging active region. II. properties of the dynamic small-scale structure. *The Astrophysical Journal*, 527(1):435–444, December 1999.

[196] P. A. Sturrock. Model of the High-Energy Phase of Solar Flares. *Nature*, 211(5050):695–697, August 1966.

[197] J. J. Sudol and J. W. Harvey. Longitudinal Magnetic Field Changes Accompanying Solar Flares. *The Astrophysical Journal*, 635:647–658, December 2005.

[198] Y. Suematsu, K. Ichimoto, Y. Katsukawa, T. Shimizu, T. Okamoto, S. Tsuneta, T. Tarbell, and R. A. Shine. High Resolution Observations of Spicules with Hinode/SOT. *Astronomical Society of the Pacific Conference Series*, 397:27, September 2008.

[199] X. Sun, J. T. Hoeksema, Y. Liu, M. Kazachenko, and R. Chen. Investigating the Magnetic Imprints of Major Solar Eruptions with SDO/HMI High-cadence Vector Magnetograms. *The Astrophysical Journal*, 839:67, April 2017.

[200] X. Sun, J. T. Hoeksema, Y. Liu, T. Wiegelmann, K. Hayashi, Q. Chen, and J. Thalmann. Evolution of Magnetic Field and Energy in a Major Eruptive Active Region Based on SDO/HMI Observation. *The Astrophysical Journal*, 748:77, April 2012.

[201] S. Takasao, H. Isobe, and K. Shibata. Numerical Simulations of Solar Chromospheric Jets Associated with Emerging Flux. *Publications of the Astronomical Society of Japan*, 65:62, June 2013.

[202] C. Tan, P. F. Chen, V. Abramenko, and H. Wang. Evolution of Optical Penumbral and Shear Flows Associated with the X3.4 Flare of 2006 December 13. *The Astrophysical Journal*, 690:1820–1828, January 2009.

[203] L. M. Thornton and C. E. Parnell. Small-Scale Flux Emergence Observed Using Hinode/SOT. *Solar Physics*, 269(1):13–40, March 2011.

[204] H. Tian, S. Yao, Q. Zong, J. He, and Y. Qi. Signatures of Magnetic Reconnection at Boundaries of Interplanetary Small-scale Magnetic Flux Ropes. *The Astrophysical Journal*, 720:454–464, September 2010.

[205] H. Tian, X. Zhu, H. Peter, J. Zhao, T. Samanta, and Y. Chen. Magnetic Reconnection at the Earliest Stage of Solar Flux Emergence. *The Astrophysical Journal*, 854(2):174, February 2018.

[206] L. Tian, D. Alexander, Y. Liu, and J. Yang. Magnetic Twist and Writhe of δ Active Regions. *Solar Physics*, 229(1):63–77, June 2005.

[207] V. S. Titov, G. Hornig, and P. Démoulin. Theory of magnetic connectivity in the solar corona. *Journal of Geophysical Research (Space Physics)*, 107(A8):1164, August 2002.

[208] V. S. Titov, Z. Mikić, J. A. Linker, R. Lionello, and S. K. Antiochos. Magnetic Topology of Coronal Hole Linkages. *The Astrophysical Journal*, 731(2):111, April 2011.

[209] S. Toriumi, Y. Katsukawa, and M. C. M. Cheung. Various Local Heating Events in the Earliest Phase of Flux Emergence. *The Astrophysical Journal*, 836:63, February 2017.

[210] S. Toriumi and S. Takasao. Numerical Simulations of Flare-productive Active Regions: δ-sunspots, Sheared Polarity Inversion Lines, Energy Storage, and Predictions. *The Astrophysical Journal*, 850(1):39, November 2017.

[211] S Toriumi and H Wang. Flare-productive active regions. *Living Reviews in Solar Physics*, 16(1):3, May 2019.

[212] G. Tsiropoula, K. Tziotziou, I. Kontogiannis, M. S. Madjarska, J. G. Doyle, and Y. Suematsu. Solar Fine-Scale Structures. I. Spicules and Other Small-Scale, Jet-Like Events at the Chromospheric Level: Observations and Physical Parameters. *Space Science Reviews*, 169(1-4):181–244, September 2012.

[213] S. Tsuneta and T. Naito. Fermi Acceleration at the Fast Shock in a Solar Flare and the Impulsive Loop-Top Hard X-Ray Source. *The Astrophysical Journal Letters*, 495(1):L67–L70, March 1998.

[214] O. van der Luehe, D. Soltau, T. Berkefeld, and T. Schelenz. KAOS: adaptive optics system for the Vacuum Tower Telescope at Teide Observatory. *International Society for Optics and Photonics*, 4853:187 – 193, 2003.

[215] L. van Driel-Gesztelyi and L. M. Green. Evolution of Active Regions. *Living Reviews in Solar Physics*, 12(1):1, September 2015.

[216] J. Varsik, C. Plymate, P. Goode, A. Kosovichev, W. Cao, R. Coulter, K. Ahn, N. Gorceix, and S. Shumko. Control and operation of the 1.6 m New Solar Telescope in Big Bear. *Society of Photo-Optical Instrumentation Engineers (SPIE) Conference Series*, 9147:91475D, August 2014.

[217] M. Verma and C. Denker. Horizontal flow fields observed in Hinode G-band images. III. The decay of a satellite sunspot and the role of magnetic flux removal in flaring. *Astronomy & Astrophysics*, 545:A92, September 2012.

[218] G. J. M. Vissers, L. H. M. Rouppe van der Voort, R. J. Rutten, M. Carlsson, and B. De Pontieu. Ellerman Bombs at High Resolution. III. Simultaneous Observations with IRIS and SST. *The Astrophysical Journal*, 812(1):11, October 2015.

[219] G. J. M. Vissers, L. H. M. Rouppe van der Voort, and R. J. Rutten. Ellerman Bombs at High Resolution. II. Triggering, Visibility, and Effect on Upper Atmosphere. *The Astrophysical Journal*, 774(1):32, August 2013.

[220] N. Vitas and E. Khomenko. Equation of state for solar near-surface convection. *Annales Geophysicae*, 33(6):703–709, June 2015.

[221] R. Volkmer, O. von der Lühe, F. Kneer, J. Staude, T. Berkefeld, P. Caligari, C. Halbgewachs, F. Heidecke, W. Schmidt, D. Soltau, H. Nicklas, A. Wittmann, H. Balthasar, A. Hofmann, K. Strassmeier, M. Sobotka, M. Klvana, and M. Collados. The new 1.5m solar telescope GREGOR: first light and start of commissioning. *Society of Photo-Optical Instrumentation Engineers (SPIE) Conference Series*, 6267:62670W, June 2006.

[222] A. Vourlidas, R. A. Howard, S. P. Plunkett, C. M. Korendyke, A. F. R. Thernisien, D. Wang, N. Rich, M. T. Carter, D. H. Chua, D. G. Socker, M. G. Linton, J. S. Morrill, S. Lynch, A. Thurn, P. Van Duyne, R. Hagood, G. Clifford, P. J. Grey, M. Velli, P. C. Liewer, J. R. Hall, E. M. DeJong, Z. Mikic, P. Rochus, E. Mazy, V. Bothmer, and J. Rodmann. The Wide-Field Imager for Solar Probe Plus (WISPR). *Space Science Reviews*, 204(1-4):83–130, December 2016.

[223] Z. Švestka. Optical Observations of Solar Flares. *Space Science Reviews*, 5(3):388–418, May 1966.

[224] H. Wang. Evolution of Vector Magnetic Fields and the August 27 1990 X-3 Flare. *Solar Physics*, 140:85–98, July 1992.

[225] H. Wang. Comparison of Hα and He II λ304 Macrospicules. *The Astrophysical Journal*, 509(1):461–470, December 1998.

[226] H. Wang. Rapid Changes of Photospheric Magnetic Fields around Flaring Magnetic Neutral Lines. *The Astrophysical Journal*, 649:490–497, September 2006.

[227] H. Wang, M. W. Ewell, Jr., H. Zirin, and G. Ai. Vector magnetic field changes associated with X-class flares. *The Astrophysical Journal*, 424:436–443, March 1994.

[228] H. Wang and C. Liu. Observational Evidence of Back Reaction on the Solar Surface Associated with Coronal Magnetic Restructuring in Solar Eruptions. *The Astrophysical Journal Letters*, 716:L195–L199, June 2010.

[229] H. Wang and C. Liu. Structure and Evolution of Magnetic Fields Associated with Solar Eruptions. *Research in Astronomy and Astrophysics*, 15:145–174, February 2015.

[230] H. Wang, C. Liu, K. Ahn, Y. Xu, J. Jing, N. Deng, N. Huang, R. Liu, K. Kusano, G. D. Fleishman, D. E. Gary, and W. Cao. High-resolution observations of flare precursors in the low solar atmosphere. *Nature Astronomy*, 1:0085, March 2017.

[231] H. Wang, C. Liu, J. Qiu, N. Deng, P. R. Goode, and C. Denker. Rapid Penumbral Decay following Three X-Class Solar Flares. *The Astrophysical Journal Letters*, 601(2):L195–L198, February 2004.

[232] H. Wang, C. Liu, S. Wang, N. Deng, Y. Xu, J. Jing, and W. Cao. Study of Rapid Formation of a δ Sunspot Associated with the 2012 July 2 C7.4 Flare Using High-resolution Observations of the New Solar Telescope. *The Astrophysical Journal Letters*, 774:L24, September 2013.

[233] H. Wang, H. Song, J. Jing, V. Yurchyshyn, Y. Deng, H. Zhang, D. Falconer, and J. Li. The Relationship between Magnetic Gradient and Magnetic Shear in Five Super Active Regions Producing Great Flares. *Chinese Journal of Astronomy and Astrophysics*, 6(4):477–488, August 2006.

[234] J. Wang, C. Liu, N. Deng, and H. Wang. Evolution of Photospheric Flow and Magnetic Fields Associated with the 2015 June 22 M6.5 Flare. *The Astrophysical Journal*, 853(2):143, February 2018.

[235] J. Wang, P. J. A. Simões, and L. Fletcher. Unambiguous Evidence of Coronal Implosions during Solar Eruptions and Flares. *The Astrophysical Journal*, 859(1):25, May 2018.

[236] J. Wang, M. Zhao, and G. Zhou. Magnetic Changes in the Course of the X7.1 Solar Flare on 2005 January 20. *The Astrophysical Journal*, 690:862–874, January 2009.

[237] S. Wang, C. Liu, N. Deng, and H. Wang. Sudden Photospheric Motion and Sunspot Rotation Associated with the X2.2 Flare on 2011 February 15. *The Astrophysical Journal Letters*, 782:L31, February 2014.

[238] S. Wang, C. Liu, R. Liu, N. Deng, Y. Liu, and H. Wang. Response of the Photospheric Magnetic Field to the X2.2 Flare on 2011 February 15. *The Astrophysical Journal Letters*, 745(2):L17, February 2012.

[239] Y. M. Wang. Coronal Holes and Open Magnetic Flux. *Space Science Reviews*, 144(1-4):383–399, April 2009.

[240] H. Watanabe, G. Vissers, R. Kitai, L. Rouppe van der Voort, and R. J. Rutten. Ellerman Bombs at High Resolution. I. Morphological Evidence for Photospheric Reconnection. *The Astrophysical Journal*, 736(1):71, July 2011.

[241] B. T. Welsch, Y. Li, P. W. Schuck, and G. H. Fisher. What is the Relationship Between Photospheric Flow Fields and Solar Flares? *The Astrophysical Journal*, 705:821–843, November 2009.

[242] M. S. Wheatland, D. B. Melrose, and A. Mastrano. Photospheric Response to a Flare. *The Astrophysical Journal*, 864(2):159, September 2018.

[243] M. S. Wheatland, P. A. Sturrock, and G. Roumeliotis. An Optimization Approach to Reconstructing Force-free Fields. *The Astrophysical Journal*, 540(2):1150–1155, September 2000.

[244] T. Wiegelmann. Optimization code with weighting function for the reconstruction of coronal magnetic fields. *Solar Physics*, 219(1):87–108, January 2004.

[245] T. Wiegelmann and B. Inhester. How to deal with measurement errors and lacking data in nonlinear force-free coronal magnetic field modelling? *Astronomy & Astrophysics*, 516:A107, June 2010.

[246] T. Wiegelmann, B. Inhester, and T. Sakurai. Preprocessing of Vector Magnetograph Data for a Nonlinear Force-Free Magnetic Field Reconstruction. *Solar Physics*, 233(2):215–232, February 2006.

[247] T. Wiegelmann and S. K. Solanki. Similarities and Differences between Coronal Holes and the Quiet Sun: Are Loop Statistics the Key? *Solar Physics*, 225(2):227–247, December 2004.

[248] T. Wiegelmann, J. K. Thalmann, B. Inhester, T. Tadesse, X. Sun, and J. T. Hoeksema. How Should One Optimize Nonlinear Force-Free Coronal Magnetic Field Extrapolations from SDO/HMI Vector Magnetograms? *Solar Physics*, 281(1):37–51, November 2012.

[249] K. Wilhelm, L. Abbo, F. Auchère, N. Barbey, L. Feng, A. H. Gabriel, S. Giordano, S. Imada, A. Llebaria, W. H. Matthaeus, G. Poletto, N. E. Raouafi, S. T. Suess, L. Teriaca, and Y. M. Wang. Morphology, dynamics and plasma parameters of plumes and inter-plume regions in solar coronal holes. *Astronomy & Astrophysics Review*, 19(1):35, June 2011.

[250] P. R. Wilson. The Structure of a Sunspot. I: The Birth and Development of a Sunspot. *Solar Physics*, 3(2):243–257, February 1968.

[251] F. Wöger, O. von der Lühe, and K. Reardon. Speckle interferometry with adaptive optics corrected solar data. *Astronomy & Astrophysics*, 488:375–381, September 2008.

[252] S. T. Wu, A. H. Wang, Yang Liu, and J. Todd Hoeksema. Data-driven Magnetohydrodynamic Model for Active Region Evolution. *The Astrophysical Journal*, 652(1):800–811, November 2006.

[253] P. F. Wyper and C. R. DeVore. Simulations of Solar Jets Confined by Coronal Loops. *The Astrophysical Journal*, 820(1):77, March 2016.

[254] Y. Xu, W. Cao, K. Ahn, J. Jing, C. Liu, J. Chae, N. Huang, N. Deng, D. E. Gary, and H. Wang. Transient rotation of photospheric vector magnetic fields associated with a solar flare. *Nature Communications*, 9:46, January 2018.

[255] Z. Xu, Y. Jiang, J. Yang, J. Hong, and H. Li. Sudden Penumbral Reappearance and Umbral Motion Induced by an M7.9 Solar Flare. *The Astrophysical Journal Letters*, 840(2):L21, May 2017.

[256] Z. Xu, Y. Jiang, J. Yang, B. Yang, and Y. Bi. Rapid Penumbra and Lorentz Force Changes in an X1.0 Solar Flare. *The Astrophysical Journal Letters*, 820:L21, March 2016.

[257] Y. Yamauchi, R. L. Moore, S. T. Suess, H. Wang, and T. Sakurai. The Magnetic Structure of Hα Macrospicules in Solar Coronal Holes. *The Astrophysical Journal*, 605(1):511–520, April 2004.

[258] Y. Yamauchi, H. Wang, Y. Jiang, N. Schwadron, and R. L. Moore. Study of Hα Macrospicules in Coronal Holes: Magnetic Structure and Evolution in Relation to Photospheric Magnetic Setting. *The Astrophysical Journal*, 629(1):572–581, August 2005.

[259] G. Yang, Y. Xu, W. Cao, H. Wang, C. Denker, and T. R. Rimmele. Photospheric Shear Flows along the Magnetic Neutral Line of Active Region 10486 prior to an X10 Flare. *The Astrophysical Journal Letters*, 617:L151–L154, December 2004.

[260] H. Yang, J. Chae, E. Lim, D. Song, K. Cho, H. Kwak, V. B. Yurchyshyn, and Y. Kim. Fine-scale Photospheric Connections of Ellerman Bombs. *The Astrophysical Journal*, 829(2):100, September 2016.

[261] P. R. Young and K. Muglach. Solar Dynamics Observatory and Hinode Observations of a Blowout Jet in a Coronal Hole. *Solar Physics*, 289(9):3313–3329, September 2014.

[262] L. Yu, S. Y. Huang, Z. G. Yuan, K. Jiang, Q. Y. Xiong, S. B. Xu, Y. Y. Wei, J. Zhang, and Z. H. Zhang. Characteristics of Magnetic Holes in the Solar Wind Revealed by Parker Solar Probe. *arXiv e-prints*, page arXiv:2010.14008, October 2020.

[263] V. Yurchyshyn, K. Ahn, V. Abramenko, P. Goode, and W. Cao. Small Scale Field Emergence and Its Impact on Photospheric Granulation. *arXiv e-prints*, page arXiv:1207.6418, July 2012.

[264] G. P. Zank, M. Nakanotani, L. L. Zhao, L. Adhikari, and J. Kasper. The Origin of Switchbacks in the Solar Corona: Linear Theory. *The Astrophysical Journal*, 903(1):1, November 2020.

[265] J. Zhang, J. Wang, C. Lee, and H. Wang. Macrospicules Observed with Hα Against the Quiet Solar Disk. *Solar Physics*, 194(1):59–72, May 2000.

[266] L. L. Zhao, G. P. Zank, Q. Hu, D. Telloni, Y. Chen, L. Adhikari, M. Nakanotani, J. C. Kasper, J. Huang, S. D. Bale, K. E. Korreck, A. W. Case, M. Stevens, J. W. Bonnell, T. Dudok de Wit, K. Goetz, P. R. Harvey, R. J. MacDowall, D. M. Malaspina, M. Pulupa, D. E. Larson, R. Livi, P. Whittlesey, K. G. Klein, and N. E. Raouafi. Detection of small magnetic flux ropes from the third and fourth Parker Solar Probe encounters. *arXiv e-prints*, page arXiv:2010.04664, October 2020.

[267] H. Zirin and M. A. Liggett. Delta spots and great flares. *Solar Physics*, 113(1-2):267–283, January 1987.

[268] H. Zirin and K. Tanaka. Magnetic transients in flares. *The Astrophysical Journal*, 250:791–795, November 1981.

[269] C. Zwaan. The Structure of Sunspots. *Annual Review of Astronomy and Astrophysics*, 6:135, January 1968.

[270] C. Zwaan. The Emergence of Magnetic Flux. *Solar Physics*, 100:397, October 1985.